# CHARACTERIZATION AND PERFORMANCE PREDICTION OF UNBOUND GRANULAR BASES WITH AND WITHOUT GEOGRIDS IN FLEXIBLE PAVEMENTS

A Dissertation

by

FAN GU

Submitted to the Office of Graduate and Professional Studies of
Texas A&M University
in partial fulfillment of the requirements for the degree of

DOCTOR OF PHILOSOPHY

| | |
|---|---|
| Chair of Committee, | Robert L. Lytton |
| Co-Chair of Committee, | Rong Luo |
| Committee Members, | Jon A. Epps |
| | Philip Park |
| | Vikram Kinra |
| Head of Department, | Robin Autenrieth |

December 2015

Major Subject: Civil Engineering

## ABSTRACT

Unbound granular materials (UGMs) constitute the supporting layer of flexible pavements. The performance of unbound granular base layer has been widely recognized to be influenced by its resilient modulus and permanent deformation, as well as whether it is reinforced by geogrids. The UGMs are found to exhibit moisture-sensitive and stress-dependent nonlinear cross-anisotropic behaviors, but are not adequately characterized by existing models in pavement engineering. The primary objective of this study is to develop a comprehensive methodology to accurately characterize the constitutive behavior of UGM, and predicting the performance of UGM in flexible pavements. Furthermore, this study aims at quantifying the influence of geogrid on pavement performance to facilitate the incorporation of geogrid into Pavement ME Design Software.

A new resilient modulus model is first developed to characterize the moisture-sensitive and stress-dependent nonlinear cross-anisotropic behavior for UGM. The moisture dependence of UGM is characterized by the degree of saturation and the matric suction. This model is validated by the laboratory resilient modulus tests on the selected UGMs at different moisture contents. The finite element approach is then employed to predict the performance of flexible pavements by incorporating this constitutive model for UGM. To accurately predict the rutting depth of base course, a new mechanistic-empirical rutting model is also developed to forecast the rutting behavior of UGM at different stress levels.

In this study, the repeated load triaxial tests are performed on a variety of granular materials to determine the resilient modulus and permanent deformation properties. The measured resilient modulus and permanent deformation properties are statistically related to a wide variety of performance-related base course properties. These regression models can accurately and efficiently predict the resilient modulus and permanent deformation properties of UGM.

A laboratory methodology is developed to evaluate the impact of geogrid on cross-anisotropy and permanent deformation properties of UGM. This impact is successfully predicted by an analytical model. Finite element models are developed to simulate the geogrid-reinforced structures by considering the geogrid-reinforcement mechanisms. These numerical models are validated by the large-scale tank tests. The validated finite element models provide a sound basis for predicting the performance of geogrid-reinforced pavements.

## DEDICATION

To my wife and my parents

## ACKNOWLEDGEMENTS

I would like to express my deepest gratitude to my advisor and committee chair, Dr. Robert L. Lytton, for his guidance, encouragement and support throughout my graduate studies at Texas A&M University. I have been fortunate to work with Dr. Lytton on so many research projects. He is such a knowledgeable professor, who is always willing to share his experience and ideas with his students. I shall always remember those days and nights discussing with Dr. Lytton on the academic problems I had.

I also would like to appreciate my committee members, Dr. Rong Luo, Dr. Jon Epps, Dr. Philip Park and Dr. Vikram Kinra, for their guidance, support and valuable comments on my research work. Thank Dr. Rong Luo and Dr. Jon Epps for providing me the opportunities to work on their research projects. These research experiences provide me a sound basis to explore my dissertation research. I am sincerely grateful to Dr. Xue Luo and Dr. Yuqing Zhang, for their encouragement and help on my studies.

Many thanks go to all of my friends and colleagues at Texas A&M University. Their friendship is one of the most valuable gifts I have received in my study. Last but not least, I would like to thank my wife and my parents for their dedication and support.

## TABLE OF CONTENTS

Page

## LIST OF FIGURES

Page

## LIST OF TABLES

Page

# 1. INTRODUCTION

## 1.1 Background

A conventional flexible pavement consists of asphalt concrete layer, granular base course and subgrade. A granular base course of good quality can provide functional support to pavement structures, and effectively dissipate the stresses induced by the traffic load to the underlying subgrade (Huang 2004). Accurate characterization and prediction of performance of unbound granular material (UGM) is crucial for flexible pavement design and analysis. In a conventional pavement design, the granular base is assumed to be linear elastic. Based on this assumption, the linear isotropic pavement model predicts an unexpected tensile stress in base layer, which conflicts with the fact that the granular material cannot transfer tensile stress among aggregate particles (Tutumluer 1995). A number of recent studies have revealed that UGM exhibits the cross-anisotropic behavior, which means the horizontal modulus of UGM is smaller than its vertical modulus (Adu-Osei et al. 2001; Tutumluer and Seyhan 1999; Oh et al. 2006). Using this anisotropic pavement model, the unexpected tensile stress in the base layer is diminished or eliminated (Tutumluer and Thompson 1997; Al-Qadi et al. 2010). In addition to cross-anisotropy, nonlinear stress-dependence and moisture-sensitivity are other important characteristics influencing the performance of UGM. In general, coarse granular base exhibits both the effects of increasing modulus with increasing confinement and decreasing modulus with increasing shear stress. Uzan (1985) developed a widely-used power model combining the bulk stress and the octahedral shear stress terms to represent the stress-dependence of UGM. Lekarp et al. (2000a)

reported that the resilient modulus of UGMs is also moisture-sensitive, i.e. the modulus decreases with the growing saturation level. Tseng and Lytton (1989) proposed a mechanistic-empirical model to predict the plastic deformation behavior of UGM subjected to repeated load. They pointed out the plastic deformation behavior of granular material is affected by both the stress level and the moisture condition. Therefore, accurate characterization and prediction of performance of UGMs needs to take into account their cross-anisotropic, nonlinear stress-dependent and moisture sensitive characteristics.

Geogrids are often used by highway agencies in unbound base layers (i.e., within the base layer or as a base/subgrade interface) as a means for enhancing the performance of flexible pavements (Berg et al. 2000; Kwon 2007; Zornberg et al. 2008). Beneficial effects of the geogrid layer have been identified on the responses of pavements under the traffic load through two major mechanisms (Giroud and Noiray 1981; Perkins and Ismeik 1997a; Giroud and Han 2004; Kwon and Tutumluer 2009): (a) later confinement, which is produced by the interface frictional interaction and interlocking between base course aggregates and the geogrid layer; and (b) vertical membrane effect, which is caused by membrane deformation to reduce vertical stress inside of base course. Although a great deal of research has been performed to evaluate the influence of geogrids on granular bases, limited research has dealt with the methodologies of quantifying their influence on pavement performance in a manner that would allow incorporation into the mechanistic-empirical pavement design and analysis procedures.

## 1.2 Problem Statement

### *1.2.1 Problems of Characterization and Performance Prediction of Granular Base*

The resilient modulus and permanent deformation behaviors of UGMs have been widely recognized as the two major factors that influence the performance of unbound granular base layer in pavement structures. In the laboratory, the resilient modulus and permanent deformation behavior are characterized by the repeated load triaxial (RLT) test. The response of unbound aggregates specimen under the repeated load is divided into a resilient (recoverable) strain and a permanent (unrecoverable) strain. The recoverable behavior is characterized by the resilient modulus of unbound aggregates. The permanent strain accumulated by the repeated load applications is used to describe the permanent deformation behavior.

In order to determine the resilient modulus of UGMs, various models have been developed to predict the resilient modulus by the bulk stress or deviatoric stress, or the combination of them (Uzan 1985; Andrei et al. 2004; NCHRP 2003). All of these models indicate that the resilient modulus of UGM is stress dependent. However, a number of studies have reported that the resilient modulus of UGM is not only stress-dependent but also moisture-dependent. AASHTO (2008) employed an environmental factor to represent the moisture dependence of resilient modulus, which irrationally assumes that the moisture condition and stress state are two independent factors. Lytton (1995) developed a constitutive model to predict the resilient modulus of UGM at any moisture content by incorporating a matric suction term into the Uzan model (Uzan

1985). This model considers the mutual effect between the moisture condition and the stress state. However the prediction accuracy of the model needs to be further validated.

Another important characteristic of resilient behavior is cross-anisotropy, which refers to a material constitutive behavior that the properties in the vertical direction are different from the properties in the horizontal plane while the properties in the horizontal plane are the same in all directions. For example, the resilient modulus of UGM is greater in the vertical direction than that in the horizontal direction. This behavior has been well documented for UGMs (Tutumluer and Thompson 1997; Adu-Osei et al. 2001; Salehi Ashtiani 2009).

However, in the current AASHTOWare Pavement ME Design, the cross-anisotropic properties are not considered in its structural response. Instead, the Pavement ME Design incorporates the isotropic material constitutive models to calculate critical pavement responses (stresses and strains). The isotropic and cross-anisotropic material constitutive models produce different pavement responses in terms of stress-strain distributions, which yield various predictions of pavement performance in the long term. Therefore, it is crucial to incorporate cross-anisotropic unbound base layer in the Pavement ME Design, which significantly affects the accuracy of critical pavement responses and distress calculations.

It is also known that the accumulated permanent strain is mainly affected by the stress level and the number of load repetitions (Tutumluer 2013). Moreover, the stress induced by the traffic load is non-uniformly distributed inside of unbound granular base in flexible pavements. Therefore, quantifying the effect of stress level on the PD

behavior of UGM is a key to accurately predict the rutting of unbound base layer. However, little effort has been dedicated to develop a mechanistic-empirical model for predicting the stress-dependent permanent deformation behavior of UGM.

### *1.2.2 Problems of Characterization and Performance Prediction of Granular Base with Geogrids*

Geogrid is defined by ASTM (2008) as "a planar product manufactured from polymeric material used with soil, rock, earth, or other geotechnical engineering related material as an integral part of a man-made project, structure, or system". Geogrids are often used by highway agencies in unbound base layers (i.e., within the layer or as a subgrade/base interface layer) as a means for enhancing the performance of flexible and rigid pavements. Although a great deal of research has been performed on the properties of these materials and their use in pavement structures, limited research has dealt with the methodologies of quantifying their influence on pavement performance in a manner that would allow incorporation into the mechanistic-empirical pavement design and analysis procedures. The *AASHTO Interim Mechanistic-Empirical Pavement Design Guide Manual of Practice* developed under NCHRP Project 01-37A provides a methodology for the analysis and performance prediction of pavements. However, use of geogrids in pavement layers and their influence on distress models have not been addressed in the current Pavement ME Design.

Procedures that quantify the influence of geogrids on pavement performance will help in determining the payoff obtained by using these materials and selecting the

appropriate material for a specific application. Such information is not readily available. Therefore, research is needed to develop a methodology for quantifying the influence of geogrids on pavement performance for use in pavement design and analysis. To achieve this goal, two steps are involved: I) develop a laboratory methodology to quantify the influence of geogrids on the performance of base material; II) propose a method to evaluate the effect of geogrid-reinforced base on pavement performance. Specifically, this study aims to develop a laboratory methodology to quantify the influence of geogrids on the resilient and plastic behavior of base material, and then to evaluate the performance of geogrid-reinforced pavement using the finite element techniques.

As stated in the previous section, the resilient behavior of unbound base is nonlinear cross-anisotropic, which has been demonstrated as the principal reason for the differences in the way pavements perform. The effects of geogrids on the anisotropy of the unbound base are expected to have a major influence on pavement performance. This is the fundamental mechanism by which geogrids affect pavement structures. However, evaluations of the effects of geogrids on the anisotropic properties of the unbound base have not been identified in any of the literature that was reviewed in this study.

The influence of geogrids on pavement structures has been evaluated using finite element models. Specifically, the finite element models are constructed to compute pavement responses (stresses, strains and deformations) of pavements (with/without a geogrid layer) under different loading configurations. These pavement responses are used to evaluate the benefits of using the geogrid layer as base reinforcement (Perkins and Ismeik 1997b; Perkins and Edens 2003; Perkins 2001; Saad et al. 2006; Prozzi and

Luo 2007). The elements addressed in the finite element models include geogrid geometric characteristics, traffic loading, constitutive models of materials and interface condition. Table 1.1 summarizes the features of the finite element models constructed for geogrid-reinforced pavements and the corresponding modeling techniques. It can be seen that aggregates base is often simplified as an isotropic linear elastic material, which ignores the nonlinear cross-anisotropic characteristics of base material. Therefore, this study aims at developing a geogrid-reinforced pavement model, which takes into account the nonlinear cross-anisotropic behavior of base material.

**Table 1.1 Summary of FE model studies on geogrid-reinforced pavements**

| Developer | Geometry | Surface Model | Base Model | Geogrid Model | Interface Model | Subgrade Model |
|---|---|---|---|---|---|---|
| Barksdale and Brown (1988) | Axial symmetric | Isotropic nonlinear elastic | Anisotropic linear elastic | Isotropic linear elastic membrane | Linear elastic-plastic | Isotropic |
| Wathugala et al. (1996) | Two dimension | Isotropic elastoplastic D-P | Isotropic elastoplastic D-P | Isotropic, elastoplastic membrane | None | Isotropic elastoplastic HiSS |
| Perkins (2001) | Three dimension | Anisotropic elastic-perfectly plastic | Isotropic plastic | Anisotropic elastic-plastic membrane | Mohr-C | Isotropic plastic |
| Saad et al. (2006) | Three dimension | Isotropic linear elastic | Isotropic elastic-plastic D-P | Isotropic linear elastic membrane | Perfect bonding | Isotropic elastoplastic Cam-Clay |
| Luo (2007) | Two dimension | Isotropic linear elastic | Isotropic linear elastic | Isotropic linear elastic truss element | Perfect bonding | Isotropic linear elastic |

## 1.3 Research Objectives

The goal of this research is to address the problems mentioned above pertaining to testing and modeling in the characterization of unbound aggregates with and without geogrids. The research will focus on achieving the following objectives:

- Develop a moisture-sensitive and stress-dependent resilient modulus model for UGM;
- Develop a finite element model to characterize the moisture-sensitive and stress-dependent nonlinear cross-anisotropic behavior of UGM;
- Develop a new mechanistic-empirical rutting model for unbound aggregates by taking into account the influence of stress level;
- Develop a laboratory methodology to quantify the influence of geogrids on pavement performance; and
- Develop a finite element model for the geogrid-reinforced pavement structure using nonlinear cross-anisotropic approach.

## 1.4 Dissertation Outline

This dissertation is organized as follows:

Section 1 is an introduction which contains background, problem statement, research objectives and dissertation outline.

Section 2 presents a methodology of modelling the moisture-sensitive and stress-dependent nonlinear cross-anisotropic behaviors of UGMs, which includes the development of a constitutive model to characterize the moisture-sensitive and stress-

dependent cross-anisotropic behaviors, and a finite element model to simulate these behaviors of UGMs based on the proposed constitutive model.

Section 3 presents a new mechanistic-empirical rutting model to evaluate the permanent deformation behavior of UGM, a repeated load triaxial test protocol to calibrate the model coefficients and to validate the accuracy of the model predictions, as well as an implementation of the developed rutting model to predict the rut depth of a flexible pavement. The new rutting model is capable of predicting the permanent deformation of the UGMs at any stress levels and numbers of load repetitions.

Section 4 presents an investigation of performance-related base course properties, and a statistical method of predicting the performance of UGM based on these performance-related base course properties. The proposed performance-related base course properties include methylene blue value, percent fines content, gradation of particle sizes, and shape, angularity and texture of coarse aggregates.

Section 5 presents a comprehensive laboratory evaluation of the impact of geogrid on cross-anisotropy and permanent deformation of UGM. One type of crushed granite material and four types of geogrids are selected for the RLT tests. The influence of the geogrid type, the sheet stiffness and the location of the geogrid is quantified in terms of the increase of resilient modulus and the reduction of permanent deformation of the UGMs.

Section 6 presents a methodology of developing finite element models for the geogrid-reinforced pavement structures by considering the lateral confinement and membrane effect reinforcement mechanisms. The measurements of the laboratory Soil

Tank test are used to validate the developed geogrid-reinforced pavement models. The effect of material and geometric factors on the performance of geogrid-reinforced pavement structures is also evaluated in this section.

Section 7 presents overall summaries and conclusions of the dissertation. Recommendations for future studies are also suggested in this section.

# 2. MODELLING OF MOISTURE-SENSITIVE AND STRESS-DEPENDENT NONLINEAR CROSS-ANISOTROPIC BEHAVIOR OF GRANULAR BASE*

## 2.1 Introduction

Unbound granular materials (UGMs) are often used as base layers for flexible pavements. An unbound granular base provides the foundational support to the pavement structure, and dissipates the stresses induced by traffic loading to the underlying subgrade. Understanding the constitutive behavior of UGM is crucial to the accurate performance prediction of the pavement structures. A number of recent studies have revealed that the UGM exhibits the nonlinear cross-anisotropic behavior, which means the resilient modulus of the granular base is stress-dependent, and its horizontal modulus is smaller than the vertical modulus. For example, Adu-Osei et al. (2001) and Tutumluer and Seyhan (1999) successfully determined the cross-anisotropic properties of UGMs by using the rapid triaxial cell device and UI-FastCell device respectively. Tutumluer and Thompson (1997) proposed an anisotropic model for granular bases in flexible pavements. They found that using a cross-anisotropic model in the base can significantly reduce or eliminate the tensile stresses predicted by the isotropic linear elastic model. Oh et al. (2006) and Al-Qadi et al. (2010) also reported that modeling the pavement structures using nonlinear cross-anisotropic approach resulted in greater predicted pavement responses. Tutumluer et al. (2003) and Wang and Al-Qadi (2013)

---

concluded that the nonlinear cross-anisotropic model provided better agreement with the field measurements. Hence, modeling the UGM as a nonlinear cross-anisotropic material should be taken into account for the pavement design and analysis. However, a review of these existing studies showed that the moisture condition of the unbound granular base was often assumed at optimum, or the same as the condition that the UGMs were tested in the laboratory. This assumption may not be true because the moisture condition of the unbound aggregate base is affected by the weather, the groundwater table depth, and the drainage condition and surface properties in the field.

The moisture content affects the constitutive behavior of UGMs, which influences the performance of pavement structures in the field. Lekarp et al. (2000a) reported that the resilient modulus of UGMs is moisture-sensitive, i.e. the modulus decreased with the growing saturation level. Saevarsdottir and Erlingsson (2013) found that increasing the moisture content of the UGMs reduced the frictional strength and the resistance to the permanent deformation. Salour and Erlingsson (2013) investigated the pavement response to variations of moisture content of base layers using falling weight deflectometer tests. They concluded that the increase of water content of UGMs significantly reduced the back-calculated modulus of base layer. These studies therefore suggested that the moisture-sensitive behavior of UGM should also be taken into account for modeling the pavement structures.

In order to characterize the moisture-sensitive behavior of UGM, AASHTO (2008) employed an environmental factor to quantify the influence of moisture content

on the resilient modulus of unbound aggregates. This model is adopted by the current Pavement ME Design, which is shown in Equation 2.1.

$$\log\frac{M_R}{M_{Ropt}} = a + \frac{b-a}{1+\exp\left[\ln\frac{-b}{a} + k_m \cdot \left(S - S_{opt}\right)\right]} \tag{2.1}$$

where $M_R$ is the resilient modulus at a given degree of saturation; $M_{Ropt}$ is the resilient modulus at reference condition; $\frac{M_R}{M_{Ropt}}$ is an environmental factor; $a$ is the minimum of $\log\left(\frac{M_R}{M_{Ropt}}\right)$; $b$ is the maximum of $\log\left(\frac{M_R}{M_{Ropt}}\right)$; $k_m$ is the regression parameter; and $\left(S - S_{opt}\right)$ is the variation of degree of saturation expressed in decimal. Heath et al. (2004) developed a framework to predict the resilient modulus of unbound aggregates at any moisture content by incorporating a normalizing matric suction term into the Uzan model (Uzan 1985). Liang et al. (2008) and Cary and Zapata (2011) also proposed similar models to characterize the moisture dependence of resilient modulus for both subgrade soils and unbound aggregates in terms of matric suction.

According to these existing studies, the constitutive model of unbound aggregates should take into account both the nonlinear cross-anisotropic behavior and the moisture-sensitive characteristic. In addition, the moisture sensitivity of the anisotropic modulus should depend on both the degree of saturation and the matric suction.

To address the aforementioned problems, this chapter aims at proposing a new constitutive model for unbound aggregates considering both nonlinear cross-anisotropic behavior and moisture-sensitive characteristics, and incorporating the proposed constitutive model into a finite element model of pavement structure to quantify the influence of moisture content on the pavement responses. More specifically, the saturation factor and the matric suction of the unsaturated unbound aggregates will be applied to the proposed constitutive model to reflect the moisture dependence. A new user-defined material (UMAT) subroutine will be developed to characterize the moisture-sensitive and stress-dependent nonlinear cross-anisotropic behavior of base material using the finite element software ABAQUS. The developed UMAT subroutine will then be implemented in the finite element model of flexible pavement structures to evaluate the effect of moisture content on the pavement responses.

## 2.2 Constitutive Model for Moisture-Sensitive and Stress-Dependent Nonlinear Cross-Anisotropic Granular Bases

The UGM is considered to be cross-anisotropic, i.e. it is isotropic in the horizontal direction and anisotropic in the vertical direction. The generalized Hooke's Law is used to define the cross-anisotropic behavior of unbound aggregates for an axisymmetric problem, which is shown in Equation 2.2.

$$\begin{bmatrix} \frac{1}{E_x} & -\frac{\nu_{xy}}{E_x} & -\frac{\nu_{xx}}{E_x} & 0 \\ -\frac{\nu_{xy}}{E_x} & \frac{1}{E_y} & -\frac{\nu_{xy}}{E_x} & 0 \\ -\frac{\nu_{xx}}{E_x} & -\frac{\nu_{xy}}{E_x} & \frac{1}{E_x} & 0 \\ 0 & 0 & 0 & \frac{1}{G_{xy}} \end{bmatrix} \begin{bmatrix} \sigma_x \\ \sigma_y \\ \sigma_x \\ \tau_{xy} \end{bmatrix} = \begin{bmatrix} \varepsilon_x \\ \varepsilon_y \\ \varepsilon_x \\ \gamma_{xy} \end{bmatrix} \tag{2.2}$$

where $E_x$ is the horizontal modulus; $E_y$ is the vertical modulus; $G_{xy}$ is the shear modulus; $\nu_{xy}$ is the Poisson's ratio to characterize the effect of vertical strain on horizontal strain; $\nu_{xx}$ is the Poisson's ratio to characterize the effect of horizontal strain on horizontal strain.

In ABAQUS, this constitutive model needs to be rewritten as a strain-stress relationship (ABAQUS 2010). Converted from Equation 2.2, the strain-stress relationship for the cross-anisotropic material can be expressed as,

$$\begin{bmatrix} \sigma_x \\ \sigma_y \\ \sigma_x \\ \tau_{xy} \end{bmatrix} = \frac{E_y}{\alpha\beta} \begin{bmatrix} n\left(1-n\nu_{yx}^2\right) & n\nu_{yx}\alpha & n\left(\nu_{xx}+n\nu_{yx}^2\right) & 0 \\ n\nu_{yx}\alpha & 1-\nu_{xx}^2 & n\nu_{yx}\alpha & 0 \\ n\left(\nu_{xx}+n\nu_{yx}^2\right) & n\nu_{yx}\alpha & n\left(1-n\nu_{yx}^2\right) & 0 \\ 0 & 0 & 0 & m\alpha\beta \end{bmatrix} \begin{bmatrix} \varepsilon_x \\ \varepsilon_y \\ \varepsilon_x \\ \frac{1}{2}\gamma_{xy} \end{bmatrix} \tag{2.3}$$

where $n=\frac{E_x}{E_y}$; $m=\frac{G_{xy}}{E_y}$; $\alpha=1+\nu_{xx}$; $\beta=1-\nu_{xx}-2n\nu_{yx}^2$. This strain-stress relationship is used to compute the incremental stress for a given incremental strain in ABAQUS. In Equation 2.3, the vertical modulus $E_y$ is dependent on both the stress state and the moisture content. In order to characterize this behavior, a new constitutive model is

proposed as shown in Equation 2.4, which incorporates a matric suction term into the generalized resilient modulus model (Lytton 1995, Gu et al. 2015).

$$E_y = k_1 P_a \left(\frac{I_1 - 3\theta f h_m}{P_a}\right)^{k_2} \left(\frac{\tau_{oct}}{P_a}\right)^{k_3} \tag{2.4}$$

where $I_1$ = the first invariant of the stress tensor; $P_a$ = the atmospheric pressure; $\theta$= the volumetric water content; $h_m$ = the matric suction in the aggregate matrix; $f$ = the saturation factor, $1 \le f \le \frac{1}{\theta}$; $\tau_{oct}$ = the octahedral shear stress; and $k_1$ , $k_2$ and $k_3$ are regression coefficients. . In this model, $I_1$ and $\tau_{oct}$ vary with the stress state, and $h_m$ is related to the moisture content of unbound aggregates.

## 2.3 Validation of Moisture-Sensitive and Stress-Dependent Resilient Modulus Model

To validate the proposed model, the repeated load triaxial tests are conducted on the three selected materials at three different moisture contents. Two critical steps are involved in using Equation 2.4 to estimate the moisture sensitive and stress-dependent resilient modulus of UGMs:

- Determine the value of the matric suction $h_m$ and examine the validity of $h_m$ in discriminating different moisture contents;
- Determine the values of $k_1$ , $k_2$ and $k_3$ by regression analysis based on the repeated load triaxial test results.

In this section, the matric suction of the UGMs is obtained from the Soil Water Characteristic Curve (SWCC), defined as the relationship between the suction and the moisture content. The SWCC has been widely used in unsaturated soils and pavement base courses. The SWCC of a specific soil can be determined based on the following two equations (Fredlund and Xing 1994):

$$\theta_w = C(h_m) \times \left[ \frac{\theta_{sat}}{\left[ \ln\left[ \exp(1) + \left( \frac{h_m}{a_f} \right)^{b_f} \right] \right]^{c_f}} \right] \tag{2.5}$$

$$C(h_m) = \left[ 1 - \frac{\ln\left( 1 + \frac{h_m}{h_r} \right)}{\ln\left( 1 + \frac{10^6}{h_r} \right)} \right] \tag{2.6}$$

where $\theta_w$ is volumetric water content, $\theta_{sat}$ is the saturated volumetric water content, $h_m$ is the matric suction, and $a_f$, $b_f$, $c_f$ and $h_r$ are regression coefficients. In the mechanistic-empirical pavement design guide, $a_f$, $b_f$, $c_f$ and $h_r$ are calculated based on $P_{200}$, the effective grain size with the 60 percent passing weight ($D_{60}$), and plasticity index (PI) (AASHTO 2008). However, the measurements of $P_{200}$ and PI show high variability, and the predicted SWCC using Equations 2.5 and 2.6 have a noticeable difference to that measured from the filter paper test (ASTM 2010). Therefore, two new properties, MBV and percent fines content, are determined to calculate $a_f$, $b_f$, $c_f$ and

$h_r$ as two repeatable and reliable indicators of material characteristics. In order to determine the SWCC, the filter paper method specified in ASTM D5298 (ASTM 2010) is used to measure the matric suction for base course materials at specific moisture contents. Sahin et al. (2015) presented the methodology to determine the SWCC for base course materials in detail. Figure 2.1 shows the generated SWCCs for the three selected base materials. The matric suction values at the optimum moisture content are determined from the SWCCs, and then substituted into Equation 2.4 to solve for the three unknown coefficients: $k_1$, $k_2$, and $k_3$, using the repeated load triaxial test data. Table 2.1 lists their values as well as associated matric suction values and the corresponding R-squared values for each specimen.

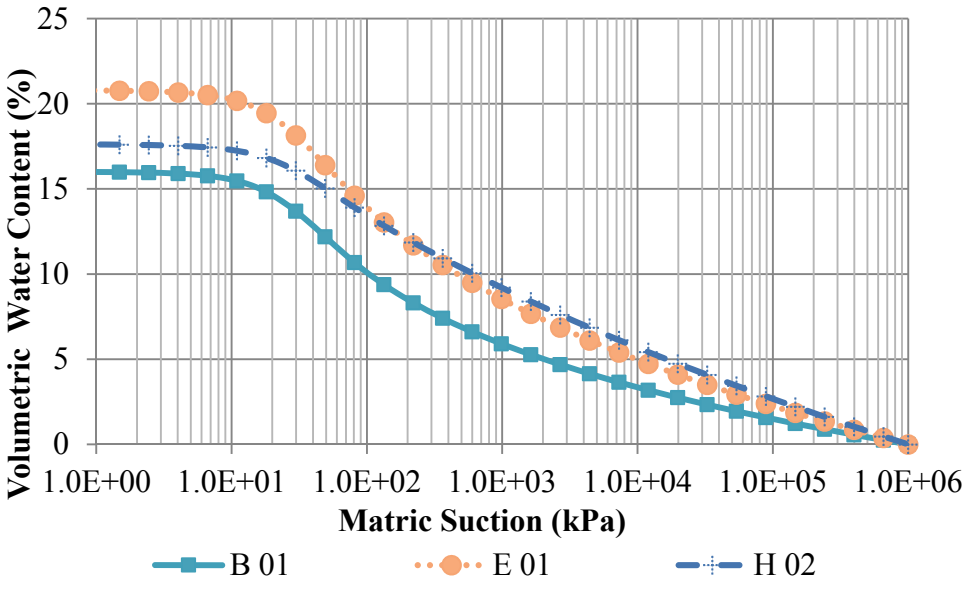


**Figure 2.1 Soil Water Characteristic Curves for Selected Materials**

**Table 2.1 Test Results for Aggregate Specimens at Optimum Moisture Content**

| Source Type | $k_1$ | $k_2$ | $k_3$ | Matric Suction (kPa) | $R^2$ |
|---|---|---|---|---|---|
| B01 | 689.1 | 1.31 | -0.16 | -20.0 | 0.99 |
| E01 | 1206.0 | 0.87 | -0.03 | -63.1 | 0.99 |
| H02 | 1928.2 | 0.71 | -0.03 | -63.1 | 0.96 |

It is seen that the matric suction value of each specimen at the given moisture content can also be determined from the SWCCs in Figure 2.1. These matric suction values are used to predict the resilient modulus at the corresponding moisture content using Equation 2.4. On the other hand, the resilient modulus of each specimen is measured using the improved repeated load triaxial test. Figure 2.2 shows the plot of the predicted resilient moduli by Equation 2.4 versus those measured from the test. A fairly good agreement is observed between the predicted resilient moduli and the measured ones. This indicates that the resilient modulus model proposed in Equation 2.4 properly reflects the change of the resilient modulus due to the moisture variations of unbound aggregates.

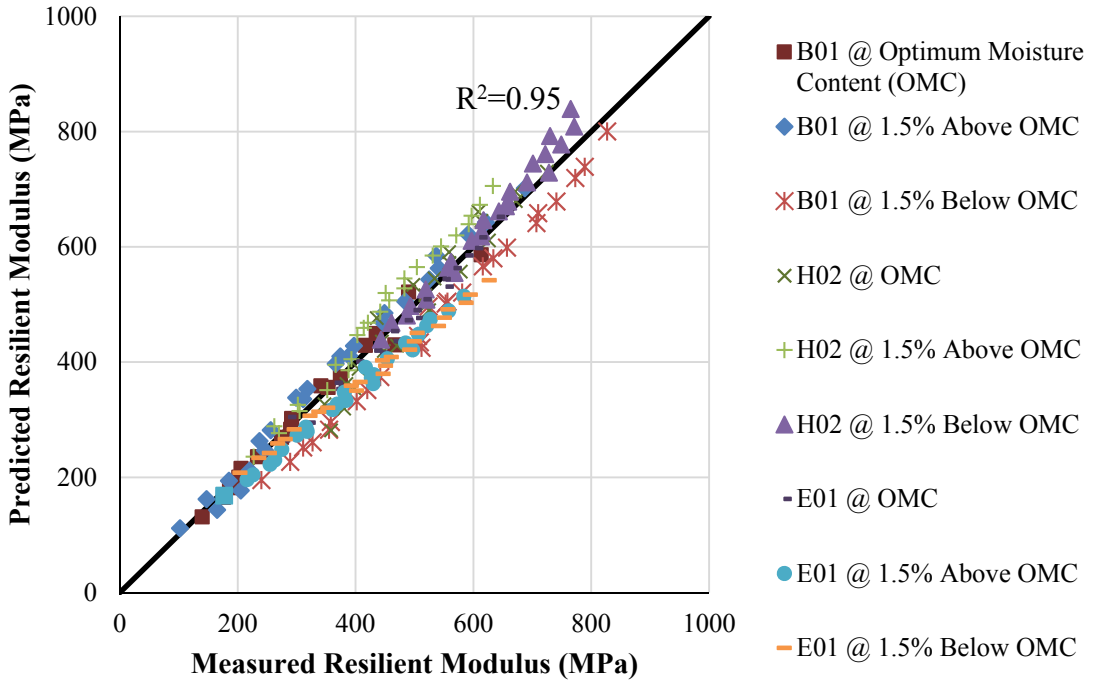


**Figure 2.2 Comparison of Predicted and Measured Resilient Moduli for Selected Base Materials**

To further examine the accuracy of the proposed resilient modulus model, the predictions by Equation 2.4 are compared to that predicted by the Pavement ME Design model (i.e., Equation 2.1). Figure 2.3 shows an example of the comparison between the proposed model and the Pavement ME Design model. It is obvious that the proposed model provides a more accurate prediction of the changes in resilient modulus due to changes in moisture. This is because the Pavement ME Design model assumes the moisture condition and stress state are independent, while the proposed model considers the influence of the moisture variation on the stress state in terms of matric suction.

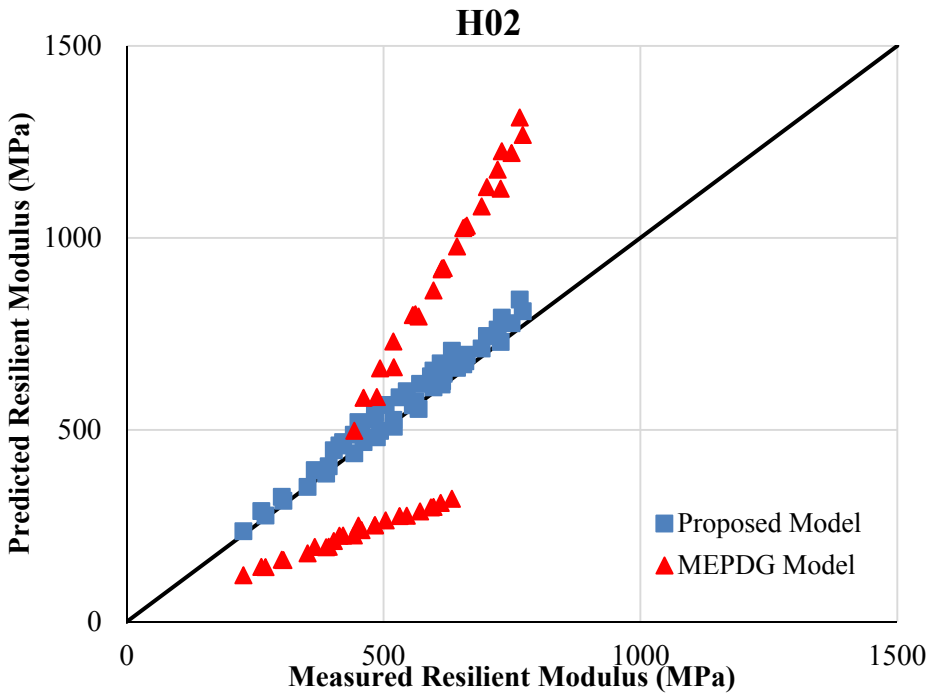


**Figure 2.3 Comparison between Predictions by Proposed Model and Pavement ME Design Model**

## 2.4 Development of a User-Defined Material Subroutine for Granular Bases

Several studies have been carried out to program different UMATs to define the elastic behavior of unbound aggregates. Hjelmstad and Taciroglu (2000) developed a UMAT subroutine for the granular material based on the tangent stiffness method. They formulated the nonlinear stress-dependent resilient modulus model as a function of the strain state. Kim et al. (2009) adopted a direct secant stiffness approach to determine the nonlinear resilient modulus solution in each iteration. This nonlinear solution technique is less complicated than the tangent stiffness approach and Newton-Raphson approach,

but it is good enough to provide good convergence of the iterations. Based on the secant stiffness approach, Wang and Al-Qadi (2013) programmed a cross-anisotropic UMAT subroutine for the unbound granular material by incorporating an anisotropic constitutive model. Using this nonlinear cross-anisotropic UMAT subroutine, he successfully analyzed the response of a 3-Dimensional pavement model under the moving vehicular loading. In this study, a similar UMAT subroutine is also programmed by using the secant stiffness technique with damping factor λ. The trial vertical modulus is computed by Equation 2.7 in each iteration.

$$E_y^i = (1-\lambda) E_y^{i-1} + \lambda E_{ycomputed}^i \tag{2.7}$$

where $E_y^i$ is the vertical modulus output from the ith iteration; $E_y^{i-1}$ is the vertical modulus output from the (i-1)$^{th}$ iteration; $\lambda$ is the damping factor; $E_{ycomputed}^i$ is the vertical modulus computed from Equation 2.4 at the i$^{th}$ iteration. The convergence criteria used in this study are shown in Equations 2.8 and 2.9.

$$Error_i = \frac{\left|E_y^i - E_y^{i-1}\right|}{\left|E_y^i\right|} \le 5\% \tag{2.8}$$

$$Error_c = \frac{\sum_{i=1}^{n}\left(E_y^i - E_y^{i-1}\right)^2}{\sum_{i=1}^{n}\left(E_y^i\right)^2} \le 0.5\% \tag{2.9}$$

where $Error_i$ is the individual error for each node; $Error_c$ is the cumulative error for the entire model; $n$ is the number of nodes in the model. The moisture-sensitive and stress-dependent cross-anisotropic constitutive models, which are shown in Equations 2.3 and

2.4, are coded into the UMAT subroutine. The Mohr-Coulomb failure theory is also applied to adjust the initially computed horizontal stresses so that the yield stress of the material will not be exceeded. This method originally proposed by ILLI-PAVE and KENLAYER is incorporated in the development of the UMAT subroutine for the nonlinear cross-anisotropic unbound aggregates in this study. Figure 2.4 is the flowchart of the developed UMAT program.

For further confirmation, the triaxial load test is simulated by using ABAQUS to verify the moduli and responses of unbound aggregates specimen under various stress states. Figure 2.5a is the schematic plot of the simulated triaxial load test in the axisymmetric condition. The inputted nonlinear cross-anisotropic properties of UGMs are shown in Table 2.2. Figures 2.5b, 2.5c and 2.5d show the distribution of vertical moduli, horizontal strains and vertical strains of a water-saturated specimen under a stress state with 70 kPa vertical stress and 40 kPa confining pressure, respectively. The computed vertical moduli, horizontal strains at point A and vertical strains at point B under various stress states are also compared to the analytical solutions calculated by Equations 2.3 and 2.4, which are shown in Table 2.3. As can be seen from Table 2.3, the simulation results based on the finite element model provide good agreement with the analytical results calculated from the constitutive models. This indicates that the developed UMAT can accurately characterize the moisture-sensitive and stress-dependent nonlinear cross-anisotropic behavior of the UGMs.

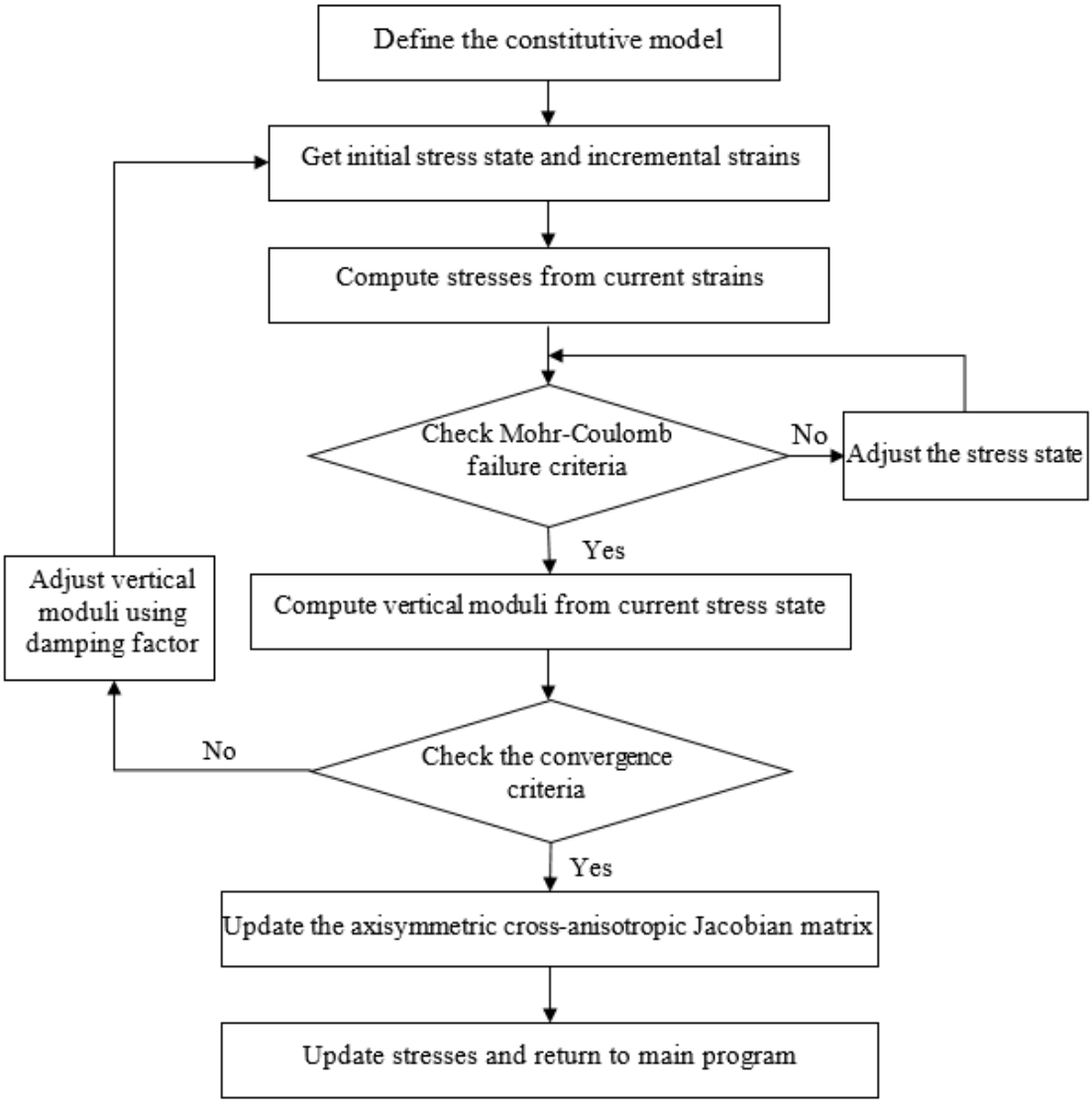


**Figure 2.4 Flowchart of the Developed UMAT Program**

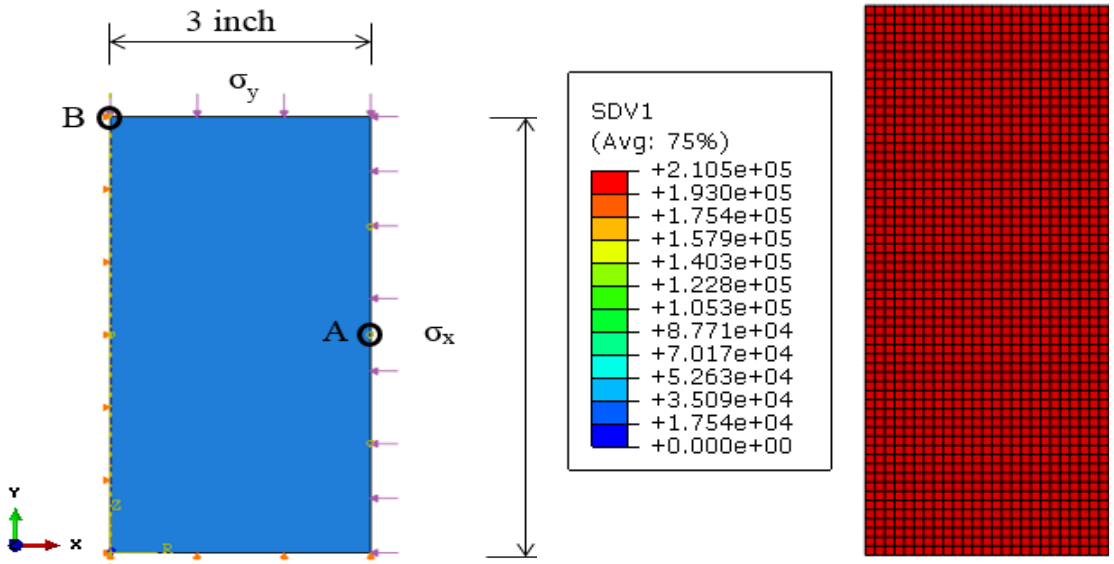


**a. Axisymmetric plot of triaxial test** **b. Vertical moduli distribution**

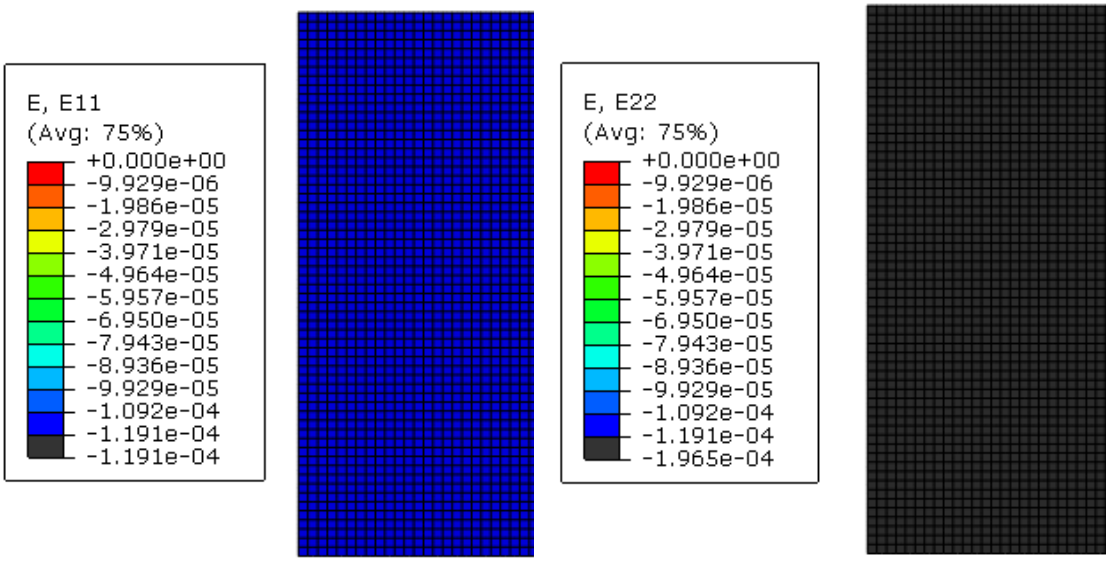


**c. Horizontal strains distribution** **d. Vertical strains distribution**

**Figure 2.5 Simulation Results of Triaxial Load Test in ABAQUS**

**Table 2.2 Inputted Nonlinear Cross-Anisotropic Properties for UGMs**

| Constitutive Model | $k_1$ | $k_2$ | $k_3$ | n | m | $\nu_{xy}$ | $\nu_{xx}$ | $\theta fh_m$ (kPa) |
|---|---|---|---|---|---|---|---|---|
| Nonlinear Cross-anisotropic | 1281 | 0.81 | -0.08 | 0.45 | 0.35 | 0.17 | 0.43 | 0 (saturated) |
| | | | | | | | | -30.0 (optimum) |
| | | | | | | | | -60.0 (dry) |

**Table 2.3 Comparison between Computational Results and Analytical Solutions**

| Stress State (kPa) | | Moisture Condition | Analytical Calculation | | | FEM Computation | | |
|---|---|---|---|---|---|---|---|---|
| σy | σx | | Ey (MPa) | εy (με) | εx (με) | Ey (MPa) | εy (με) | εx (με) |
| 70 | 40 | Saturated | 209 | 191 | 116 | 205 | 190 | 114 |
| | | Optimum | 305 | 130 | 79 | 299 | 127 | 73 |
| | | Dry | 395 | 101 | 61 | 387 | 97 | 55 |

## 2.5 Finite Element Modelling of Flexible Pavement Structures

As shown in Figure 2.6a, the axisymmetric pavement structures analyzed in this section consist of a 15-cm hot mix asphalt (HMA) layer, a 25-cm unbound aggregate base and 1.4-meter subgrade. The pavement structures are subjected to a half-sine impact load with a loading amplitude of 40.03 kN and a pulse duration of 0.1 second. The load is assumed as a uniform pressure over a 0.15m radius of circular area at the left edge of the axisymmetric pavement structures. Figure 2.6b shows the meshed finite element model that is constructed according to the pavement structures in Figure 2.6a.

Fine mesh is used in the loading area. 8-node biquadratic axisymmetric elements with reduced integration are used in the whole finite domain. The interfaces between the HMA layer, unbound aggregate base and subgrade are assumed to be fully bonded.

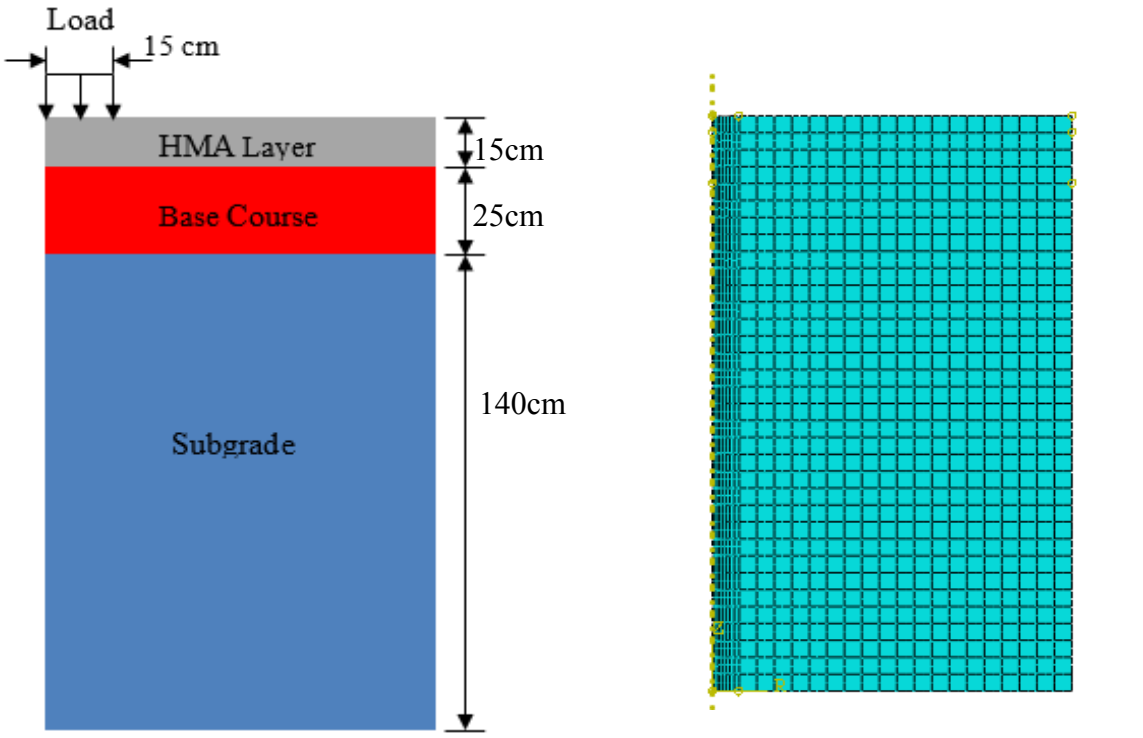


**(a) Schematic Plot of Pavement Structures** **(b) Meshed Finite Element Model**

**Figure 2.6 Finite Element Modeling of Flexible Pavement Structures**

HMA is considered as a viscoelastic material in the numerical analysis. In ABAQUS, the Prony-Series models are used to characterize the time-dependent behavior of HMA, which are shown in Equations 2.10 and 2.11.

$$G(t) = G_0\left(1 - \sum_{i=1}^{n} G_i\left(1 - e^{-t/\tau}\right)\right) \tag{2.10}$$

$$K(t) = K_0\left(1 - \sum_{i=1}^{n} K_i\left(1 - e^{-t/\tau}\right)\right) \tag{2.11}$$

where $G(t)$ and $K(t)$ are relaxation shear modulus and bulk modulus; $G_0$ and $K_0$ are instantaneous shear modulus and bulk modulus; $G_i$, $K_i$ and $\tau_i$ are the input coefficients. Table 2.4a lists the coefficients of the Prony-Series model for the HMA. A constant Poisson's ratio is assumed during the analysis. As mentioned previously, one of the objectives of this study is to model the nonlinear cross-anisotropic behavior of UGM. The nonlinear cross-anisotropic parameters, including $k_1$, $k_2$, $k_3$, $n$, $m$, $\nu_{xx}$ and $\nu_{yx}$, are presented in Table 2.4b. Figure 2.7 is the SWCC of the base material to characterize the moisture-dependence of UGM. As shown in Table 2.4c, subgrade is simplified as a linear-elastic material with constant Poisson's ratio.

**Table 2.4 Determined Model Coefficients for Paving Materials**

**a. Determined Prony-series Model Coefficients for HMA**

| Series Number | Prony-Series Coefficients | | |
|---|---|---|---|
| i | $G_i$ | $K_i$ | $\tau_i$ |
| 1 | 0.362 | 0.362 | 4.09E-06 |
| 2 | 0.363 | 0.363 | 2.56E-04 |
| 3 | 0.1765 | 0.1765 | 7.71E-03 |
| 4 | 0.074 | 0.074 | 2.10E-01 |
| 5 | 0.0165 | 0.0165 | 3.88E+00 |
| 6 | 0.0057 | 0.0057 | 6.53E+01 |
| Elastic parameters: instantaneous modulus = 18,130 MPa; Poisson's ratio = 0.35 | | | |
| Note: $\sum_{i=1}^{n} G_i \le 1$ and $\sum_{i=1}^{n} K_i \le 1$ | | | |

**b. Nonlinear Cross-anisotropic Properties for Unbound Aggregates Base**

| Material Properties | $k_1$ | $k_2$ | $k_3$ | n | m | $\nu_{xy}$ | $\nu_{xx}$ |
|---|---|---|---|---|---|---|---|
| **Values** | 1281 | 0.81 | -0.08 | 0.45 | 0.35 | 0.17 | 0.43 |

**c. Linear-Elastic Material Properties of Subgrade**

| Material Properties | E (MPa) | v |
|---|---|---|
| **Values** | 56 | 0.4 |

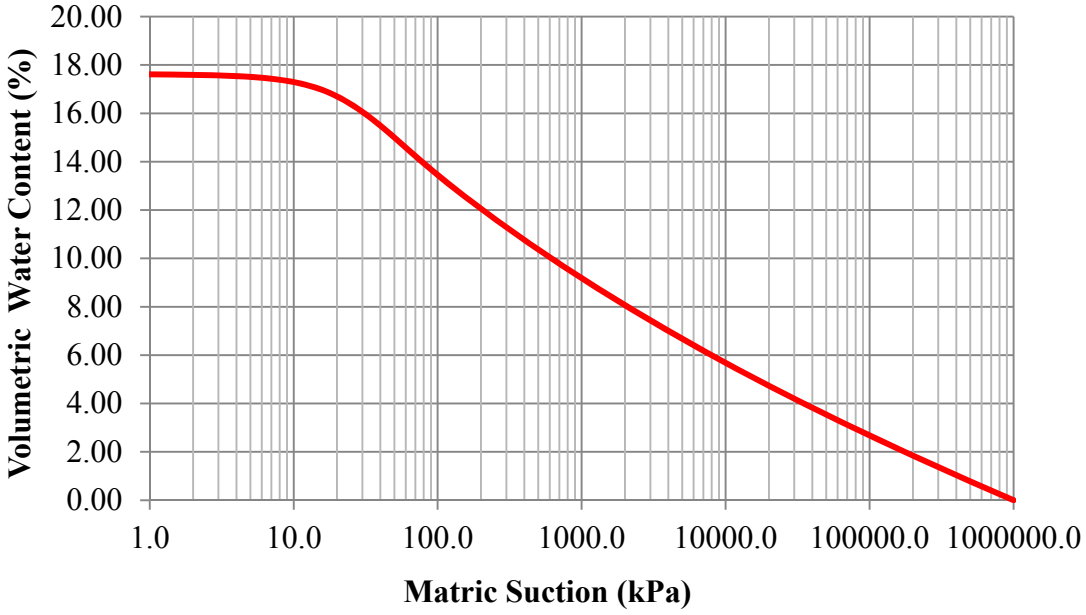


**Figure 2.7 Soil Water Characteristic Curve for the Modeled Base Material**

## 2.6 Influence of Moisture Content of Base Material on Pavement Response

To investigate the influence of moisture content of base material on pavement response, three moisture conditions are simulated in the numerical model, which include the dry condition (i.e., 1.5% below the optimum moisture content), the optimum condition (i.e., the optimum moisture content), and the moist condition (i.e., 1.5% above the optimum moisture content). Figure 2.8 compares the vertical moduli distribution in base course at different moisture conditions. It is shown that the modulus of base material decreases from the top to the bottom of base layer. The modulus of base material is sensitive to the moisture condition. It is seen that the moduli of base material at the dry condition are nearly twice as large as those of base material at the moist

condition. This variation further results in the change of pavement responses, such as the surface deflection, the tensile strain at the bottom of asphalt concrete, and the compressive strain in base course and subgrade. Figures 2.9-2.12 show the influence of the moisture condition on these pavement responses. It is seen that the model-predicted surface deflections, tensile strain at the bottom of asphalt concrete and compressive strains in base course are significantly sensitive to the moisture condition in base course, while the model-predicted compressive strain at the top of subgrade is slightly affected by the moisture variation in base course. It is obvious that increasing the moisture content of base course results in larger surface deflections, higher tensile strains at the bottom of asphalt concrete, and higher compressive strains in base and subgrade. This indicates that the current finite element model can properly reflect the influence of moisture content of base material on pavement responses.

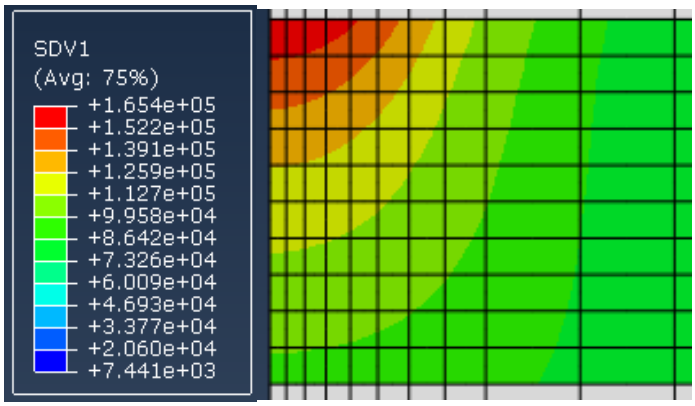


**a. Base Course at Moist Condition**

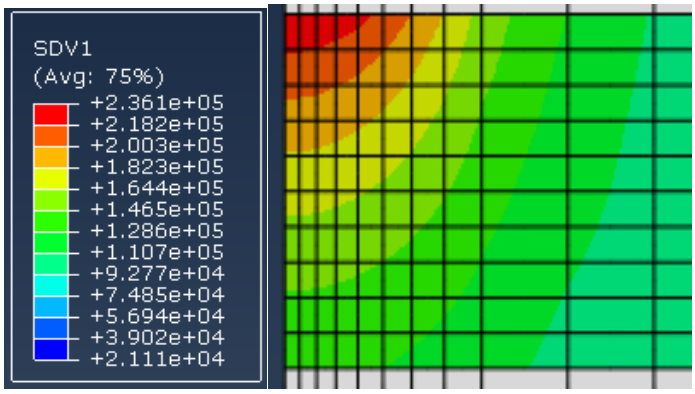


**b. Base Course at Optimum Condition**

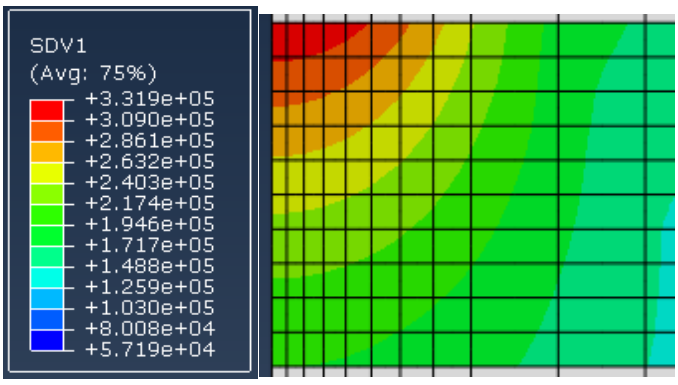


**c. Base Course at Dry Condition**

**Figure 2.8 Vertical Moduli Distribution of Base Course for Different Moisture Conditions of Base Material**

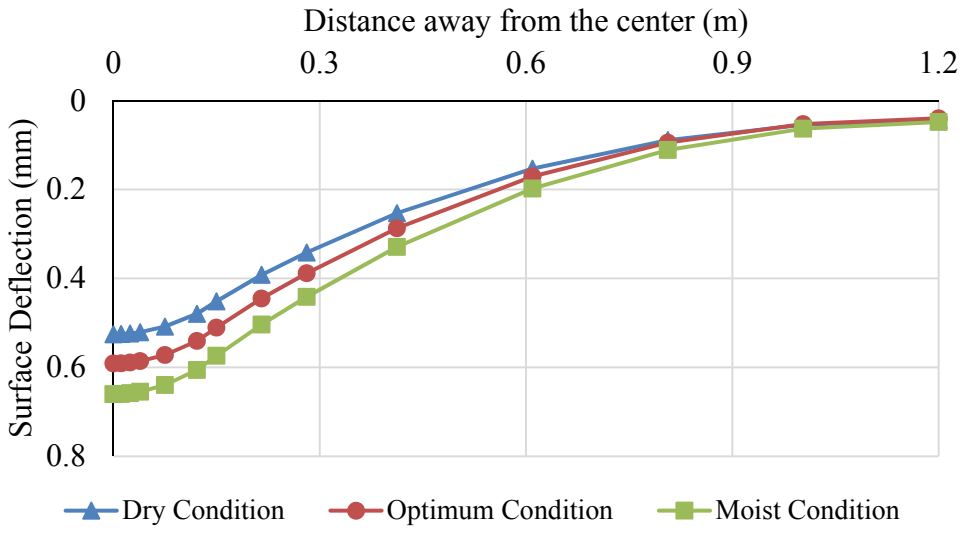


**Figure 2.9 Surface Deflections of Flexible Pavement for Different Moisture Conditions of Base Material**

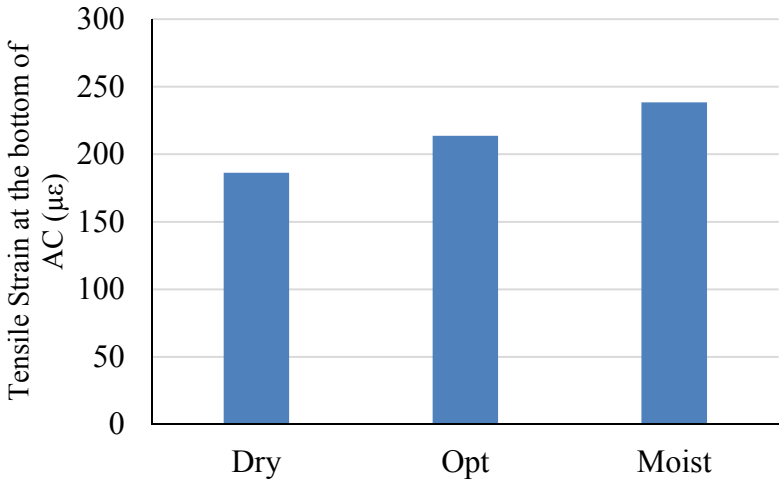


**Figure 2.10 Tensile Strain at the Bottom of Asphalt Concrete for Different Moisture Conditions of Base Material**

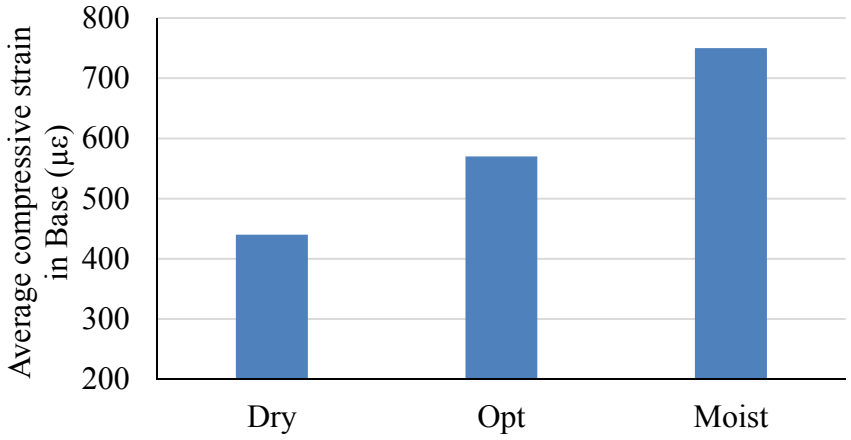


**Figure 2.11 Average Compressive Strain in Base Layer for Different Moisture Conditions of Base Material**

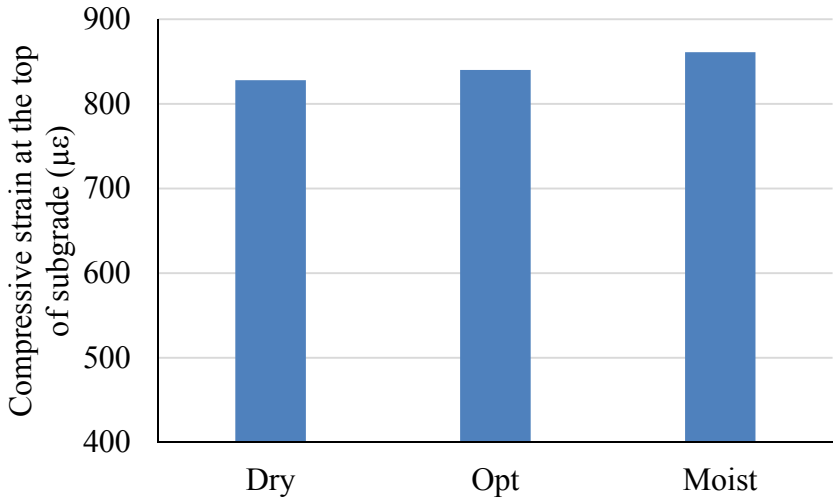


**Figure 2.12 Compressive Strain at the Top of Subgrade for Different Moisture Conditions of Base Material**

# 3. DEVELOPMENT OF A NEW MECHANISTIC-EMPIRICAL RUTTING MODEL FOR UNBOUND GRANULAR MATERIAL

## 3.1 Introduction

Rutting or accumulated permanent deformation (PD) is the primary distress for unbound aggregate bases in flexible pavements. Accordingly, understanding the PD behavior of an unbound granular material (UGM) plays a significant role in the accurate evaluation and prediction of the performance of an unbound base layer (Epps et al. 2014). In the laboratory, the PD behavior of the UGM is characterized by repeated load triaxial (RLT) tests. The responses of an unbound aggregate specimen under the repeated load include the resilient (recoverable) strain and the permanent (unrecoverable) strain. The recoverable behavior is characterized by the resilient modulus of the unbound aggregates. The permanent strain accumulated by the repeated load applications is used to describe the PD behavior (Lekarp et al. 2000b). It is known that the accumulated permanent strain is mainly affected by the stress level and the number of load repetitions (Tutumluer 2013, Xiao et al. 2015). Moreover, the stress induced by the traffic load is non-uniformly distributed in the base course of flexible pavements. Therefore, quantifying the effect of stress level on PD behavior of the UGM is critical to accurately predict the rutting of the unbound base layer.

In order to characterize the PD behavior of UGM, various rutting models have been developed to predict the accumulated PD with the number of load cycles. The existing rutting models for UGM are generally divided into two categories: the rutting models of the first category are purely mechanics-based, which were developed based on

elastoplastic theory (Desai 1980; Desai and Faruque 1984; Vermeer 1982; Uzan 1999; Chazallon et al. 2006; Chen et al. 2010). The advantages of these elastoplastic models are that they consider the effects of stress level and stress path on the PD of the UGM. However, they are typically complicated in analysis, and time-consuming in rutting prediction, which make them hard to implement in pavement design. The rutting models of the second category are mechanistic-empirical models, which were focused on developing the relationship between the accumulated PD and the load repetitions (Lytton et al. 1993). These mechanistic-empirical models are widely used in the current pavement ME designs. They are simple in analysis, fast in computation, and provide acceptable accuracy in rutting predictions.

Based on the RLT test protocols, the mechanistic-empirical models are also categorized as two groups, single-stage models and multi-stage models. Single-stage implies that the RLT test is performed at one stress level in one test. Multi-stage means that the RLT tests are performed at multiple stress levels in one test on one specimen (Erlingsson and Rahman 2013; Gabr and Cameron 2013). The multi-stage models need to consider the effects of the stress level and the stress history on PD of the UGM, which are beyond the scope of this study. In the single stage RLT tests, multiple specimens are commonly tested at different stress levels. The most popular single-stage model is the Tseng-Lytton model (Tseng and Lytton 1989) as shown in Equation 3.1.

$$\varepsilon^p = \varepsilon_0^p e^{-(\frac{\rho}{N})^\beta} \tag{3.1}$$

where $\varepsilon^p$ is the permanent strain of the granular material; $\varepsilon_0^p$ is the maximum permanent strain; $N$ is number of load cycles; $\rho$ is a scale factor; and $\beta$ is a shape factor. $\varepsilon_0^p$, $\rho$ and $\beta$ are three unknown parameters. The Tseng-Lytton model is efficient for predicting the accumulated PD at one stress level. However, in this form, it does not consider the stress effect. Therefore, the test data from different stress levels result in different combinations of the three parameters ($\varepsilon_0^p$, $\rho$ and $\beta$). In order to quantify the effect of stress level, the relationships between stress levels and the three-parameters are established based on a statistical analysis. The regression models normally have relatively low R-squared values (Tseng and Lytton 1989), which means this method cannot accurately represent the stress dependent PD behavior.

To improve the prediction accuracy, several single-stage models were developed to take into account the stress effect, including the MEPDG model (NCHRP 2004), Korkiala-Tanttu (K-T) model (Korkiala-Tanttu 2009), and UIUC model (Chow et al. 2014). Equation 3.2 is the MEPDG model, which converts the plastic strain measured from the laboratory to the field condition.

$$\varepsilon_p = \beta_s \left( \frac{\varepsilon_0}{\varepsilon_r} \right) e^{-\left(\frac{\rho}{N}\right)^{\beta}} \varepsilon_v \tag{3.2}$$

where $\beta_s$ is a global calibration coefficient, 1.673 for granular materials; $\varepsilon_r$ is the resilient strain imposed in the laboratory test; and $\varepsilon_v$ is the average vertical resilient strain in the base layer of the flexible pavements. It can be seen from Equation 3.2 that the MEPDG model considers the effect of stress on PD by linearly projecting the plastic

deformation obtained from the laboratory tests to the plastic deformation of the pavement base layer in the field through vertical strains (rather than stresses). The projection is an assumption without any mechanical or experimental justifications, which turns out to be inaccurate due to the nonlinear effect of the stress on the PD of the UGM according to this study.

Equation 3.3 shows the K-T model developed in Finland, which is widely used by researchers from Europe.

$$\varepsilon_p = C \cdot N^b \frac{R}{1-R} \tag{3.3}$$

$$b = d\left(\frac{q}{q_f}\right) + c' \tag{3.4}$$

where $C$ is the permanent strain in the first loading cycle, $b$ is a shear ratio parameter shown in Equation 3.4, $R$ is the shear failure ratio $= \frac{q}{q_f} = \frac{\sigma_1 - \sigma_3}{q_0 + Mp}$, $M = \frac{6\sin\phi}{3-\sin\phi}$, $q_0 = \frac{c \cdot 6\cos\phi}{3-\sin\phi}$, where $c$and $\phi$ are cohesion and friction angle, and $d$ and $c'$ are material parameters. The K-T model used a deviatoric stress ratio to capture the nonlinear effect of stress state, which is an improvement to the MEPDG model. However, limitations exist in the K-T model which include a) plastic deformation becomes infinity when the load cycles go to infinity, and this is unreasonable for an UGM without considering stress level; b) the K-T model cannot clearly demonstrate the hardening and softening behavior of the UGM; and c) regression analyses indicate that the K-T model cannot

accurately predict the plastic deformation of the UGM at different stress levels, which will be illustrated in this study.

The UIUC model (Chow et al. 2014) was developed in a recent study by incorporating the power functions of deviatoric shear stress and shear strength ratio into the VESYS model (Kenis 1977), which is shown in Equation 3.5.

$$\varepsilon_p = AN^B \sigma_d^C \left( \frac{\tau_f}{\tau_{\max}} \right)^D \tag{3.5}$$

where $\sigma_d$ is the deviatoric shear stress, $\tau_f$ is the shear stress, and $\tau_{\max}$ is the shear strength, $A$, $B$, $C$ and $D$ are regression coefficients. Chow (2014) conducted the RLT tests for 16 types of materials at one confining pressure (i.e. 34.5 kPa) and three deviatoric stress states to validate the UIUC model. According to the test results, the UIUC model predicted the plastic deformation of the UGM with very high R-squared values. However, the four regression coefficients varied significantly from one UGM to another (e.g., the coefficient A can differ by more than $10^{17}$ between different UGM specimens). In addition, the study was performed at one confining pressure, thus the UIUC model still needs to be validated for the stress states at different confining pressures. More drawbacks still exist in the UIUC model, including: a) when the number of load cycles $N$ is close to infinity, the corresponding plastic strain also goes to infinity, which is unreasonable for the UGM at one confining pressure; b) the model uses the shear strength ratio, which empirically assumes the contribution of shear stress to plastic strain is proportional to that of shear strength to plastic strain; c) the deviatoric shear stress term interferes with the shear strength ratio in the model, both of which

represent the softening behavior of the material without addressing the hardening aspect of bulk stress on the UGM.

The objective of this chapter is to develop a mechanistic-empirical rutting (MER) model for UGM, which is capable of predicting the rutting behavior of the UGM at different stress states using the single-stage test protocol. The proposed MER model will be calibrated and validated at various confining pressures and deviatoric pressures. The developed rutting model will also be compared with the existing single-stage models, including the MEPDG model, K-T model, and UIUC model in terms of the rutting prediction in the RLT tests and pavement structures.

## 3.2 Development of Rutting Model for Unbound Granular Material

In order to characterize the stress-dependent PD behavior of unbound aggregates, a new MER model is proposed, i.e., the MER model shown in Equation 3.6. The MER model is able to determine the accumulated PD at any specific stress state and number of load repetitions.

$$\varepsilon_p = \varepsilon_0 e^{-\left(\frac{\rho}{N}\right)^{\beta}} \left(\sqrt{J_2}\right)^m \left(\alpha I_1 + K\right)^n \tag{3.6}$$

$$\alpha = \frac{2\sin\phi}{\sqrt{3}\left(3-\sin\phi\right)} \tag{3.7}$$

$$K = \frac{c \cdot 6\cos\phi}{\sqrt{3}\left(3-\sin\phi\right)} \tag{3.8}$$

where $J_2$ is the second invariant of the deviatoric stress tensor; $I_1$ is the first invariant of the stress tensor; $\varepsilon_0$, $\rho$, $\beta$, $m$ and $n$ are model coefficients; $c$ and $\phi$ are cohesive strength and friction angle, respectively. In this model, the two terms, $\sqrt{J_2}$ and $\alpha I_1 + K$, are incorporated into the Tseng-Lytton model, which are used to reflect the influence of a stress state on the PD of the UGM.

Figure 3.1 illustrates the concept of the MER model. The Drucker-Prager plastic yield criterion (Drucker and Prager 1952), which is widely applied to rock, concrete and other pressure-dependent materials, is used in this study. As shown in Figure 3.1, the black dot represents the current stress state in the $I_1 - \sqrt{J_2}$ plane. The term of $\sqrt{J_2}$ represents the softening effects of the deviatoric shear stress on the UGM, and a higher $\sqrt{J_2}$ yields a larger PD. Thus the power coefficient m is always a positive number. In addition, the term $\alpha I_1 + K$ indicates the hardening/strengthening effect of the hydrostatic stress on the UGM, which is highly affected by the material cohesion and internal friction angle. A higher $\alpha I_1 + K$ value results in a smaller plastic deformation, thus the power coefficient n is always a negative number. Note that, using the same concept but different plastic yield criterion, the MER model can be extended to address more mechanical properties of the granular materials such as the anisotropy, convexity of the yield surface, extensive yielding, etc. (Zhang et al. 2014; Matsuoka and Nakai 1985).

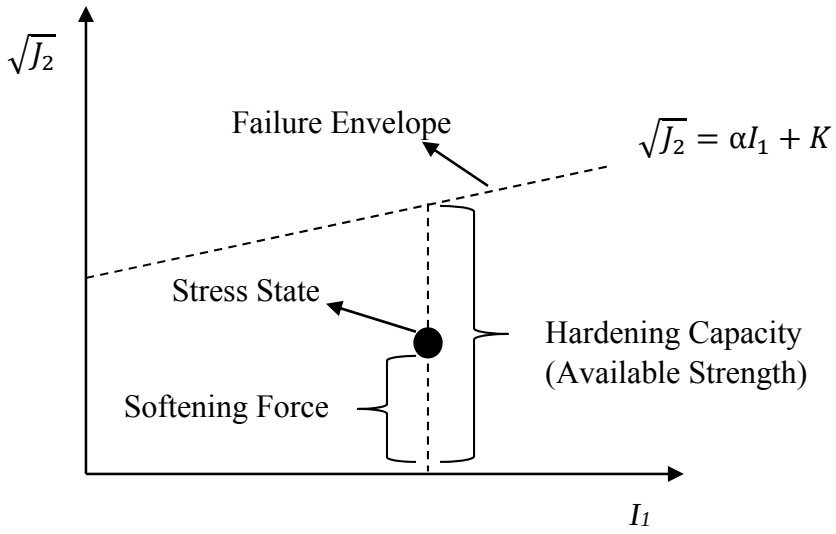


**Figure 3.1 Illustration of the Stress-Related Terms in the Proposed Model**

Two critical steps are involved in using Equation 3.6 to determine the coefficients of the proposed rutting model:

- Determine the cohesion $c$ and friction angle $\phi$ from the triaxial compressive strength tests;
- Determine the coefficients $\varepsilon_0$, $\rho$, $\beta$, $m$ and $n$ from the RLT tests at multiple stress levels.

## 3.3 Materials and Experiment

### *3.3.1 Compressive Strength Test*

The triaxial compressive strength test is a standard test used to determine the shearing resistance of base materials, which is documented in Tex-117-E (TxDOT

2010). The axial load with a constant strain rate of 2% per minute is applied on the aggregate matrix specimen under different confining stress levels (i.e. 0 kPa, 20.7 kPa, and 103.4 kPa) until it is broken. The maximum axial load value is recorded as compressive strength for a specific confining stress. Finally, the cohesion $C$ and the friction angle $\phi$ are determined based on the Mohr's failure envelope. Note that α and K can also be determined directly from the compressive strength tests at different confining stresses by plotting the $\sqrt{J_2}\sim I_1$ diagram.

### *3.3.2 Repeated Load Triaxial Test*

The RLT test is performed on cylindrical aggregate specimens using the Universal Testing Machine (UTM) with a Rapid Triaxial Test (RaTT) cell. Figure 3.2 shows the configuration of the RLT test. Prior to testing, the RaTT cell is moved downward to encompass the specimen. A static confining pressure is applied directly to the specimen by the RaTT cell via a pneumatic bladder. The dynamic axial load is applied to the specimen through the loading frame of the UTM. The axial load follows a haversine shape with 0.1 second load period and 0.9 second rest period. In pre-conditioning, the confining pressure is controlled constantly at 103.4 kPa, and a 103.4 kPa deviatoric axial load is applied for 500 repetitions (AASHTO 2003). The specimens are then subjected to 10,000 cycles of repeated load at the specified stress levels shown in Tables 3.1a and 3.1b, respectively. During each test, two linear variable differential transformers (LVDTs) mounted on the top of the specimen are used to measure the

vertical deformation of the specimen. The test data are used to determine the PD behavior of the UGM.

As seen in Table 3.1a, a total of 7 stress levels are designed to determine the coefficients of the proposed rutting model. Stress states 1, 2, 3 and 4 employ the same $I_1$ but different $J_2$, whereas stress states 1, 5, 6 and 7 apply the same $J_2$ with various $I_1$. This test protocol allows for quantifying the influence of $I_1$ and $J_2$ on the PD behavior of UGM, individually. Note that stress state 4 represents a hydrostatic state, which can also be used to verify that the plastic behavior of UGM is marginal under the hydrostatic condition. Table 3.1b presents the other 2 stress states used to validate the determined coefficients in the proposed MER model.


**Figure 3.2 Configuration of Repeated Load Permanent Deformation Test**

**Table 3.1 Proposed Permanent Deformation Test Protocol**

**a. Proposed Stress Levels for Calibration of Model Coefficients**

| Stress State | Confining Pressure, $\sigma_3$ (kPa) | Deviatoric Stress, $\sigma_d$ (kPa) | Bulk Stress, $I_1$ (kPa) | Second Invariant of Shear Stress Tensor, $J_2$ ($kPa^2$) |
|---|---|---|---|---|
| 1 | 27.6 | 192.9 | 275.6 | 12406.0 |
| 2 | 48.2 | 130.9 | 275.6 | 5712.5 |
| 3 | 68.9 | 68.9 | 275.6 | 1582.4 |
| 4 | 91.9 | 0 | 275.6 | 0 |
| 5 | 48.2 | 192.9 | 337.6 | 12406.0 |
| 6 | 68.9 | 192.9 | 399.6 | 12406.0 |
| 7 | 89.6 | 192.9 | 461.6 | 12406.0 |

**b. Proposed Stress Levels for Validation of Model Coefficients**

| Stress State | Confining Pressure, $\sigma_3$ (kPa) | Deviatoric Stress, $\sigma_d$ (kPa) | Bulk Stress, $I_1$ (kPa) | Second Invariant of Shear Stress Tensor, $J_2$ ($kPa^2$) |
|---|---|---|---|---|
| 8 | 34.5 | 172.3 | 275.6 | 9890.0 |
| 9 | 103.4 | 192.9 | 503.0 | 12406.0 |

### *3.3.3 Materials*

Two crushed aggregate materials, including a granite aggregate and a limestone conglomerate aggregate, are used in this study. Figure 3.3 shows the aggregate gradation for the two selected materials. The aggregate specimens are fabricated as 15-cm diameter and 15-cm height cylinders using a modified compactive effort (ASTM 2012). The compressive strength tests are first performed on the fabricated specimens to

determine the cohesion and the internal friction angle. The permanent deformation behavior of the base materials are then characterized by the RLT tests. Table 3.2 lists the physical properties of the unbound aggregates, including maximum dry density γd, optimum moisture content ω, liquid limit (LL), plasticity index (PI), cohesive strength c, and friction angle Φ. The measured cohesion and friction angle values will be used to determine the coefficients of the proposed rutting model.

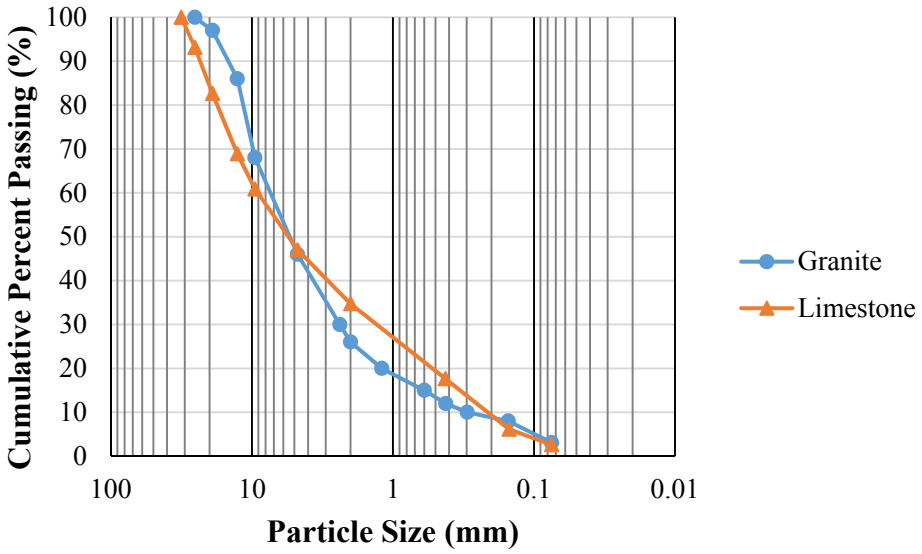


**Figure 3.3 Particle Size Distribution for Base Materials Used in This Study**

**Table 3.2 Physical Properties of Base Materials Used in This Study**

| Aggregate Type | $\gamma_d$ (kg/m$^3$) | ω (%) | LL | PI | c (kPa) | Φ (degree) |
|---|---|---|---|---|---|---|
| Granite | 2162 | 6.7 | 25 | 4 | 20.2 | 51.3 |
| Limestone | 1934 | 13.5 | NA* | NP** | 66.2 | 54.9 |

Note: *: NA= Not applicable; **: NP= Non-plastic

## 3.4 Determination of Coefficients of the Rutting Model

Based on the results of the RLT tests, the correlations of $I_1$ and $J_2$ with the accumulated permanent strain at 10,000 load cycles are presented in Figures 3.4a and 3.4b, respectively. At the same $I_1$, increasing $J_2$ results in an increasing accumulated permanent strain, which indicates that $J_2$ is a softening factor for the PD of UGM. While at a consistent $J_2$, increasing $I_1$ yields a reduction of the accumulated permanent strain, which demonstrates that $I_1$ is a strengthening indicator for the PD of UGM. As can be seen in Figures 3.4a and 3.4b, the correlations are fitted by the power functions with 0.97~0.99 R-Squared values. The high goodness of fit explains why the power models of $I_1$ and $J_2$ are incorporated in Equation 3.6.

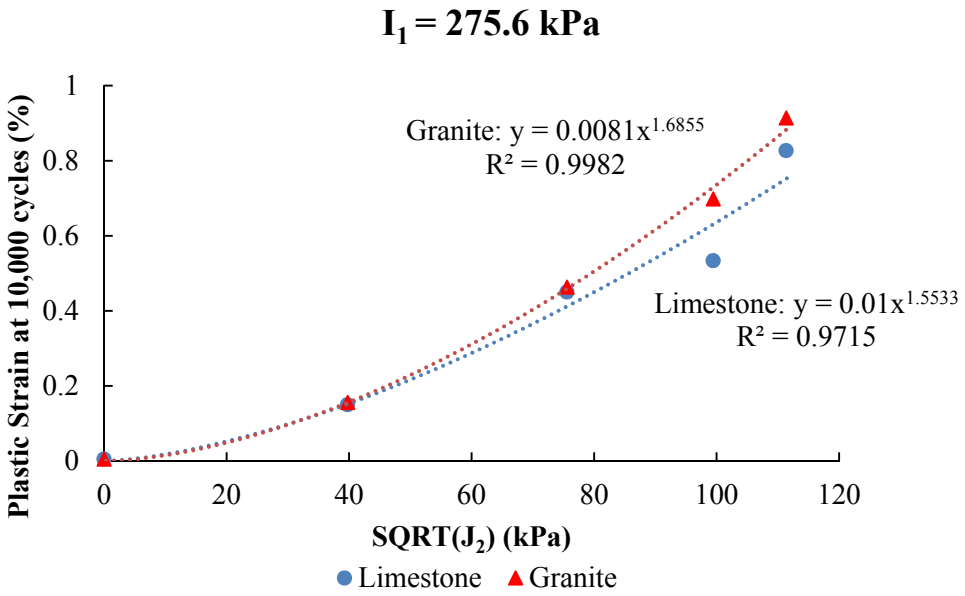


**a. Correlations of $J_2$ with Accumulated Plastic Strain at 10,000 Load Cycles**

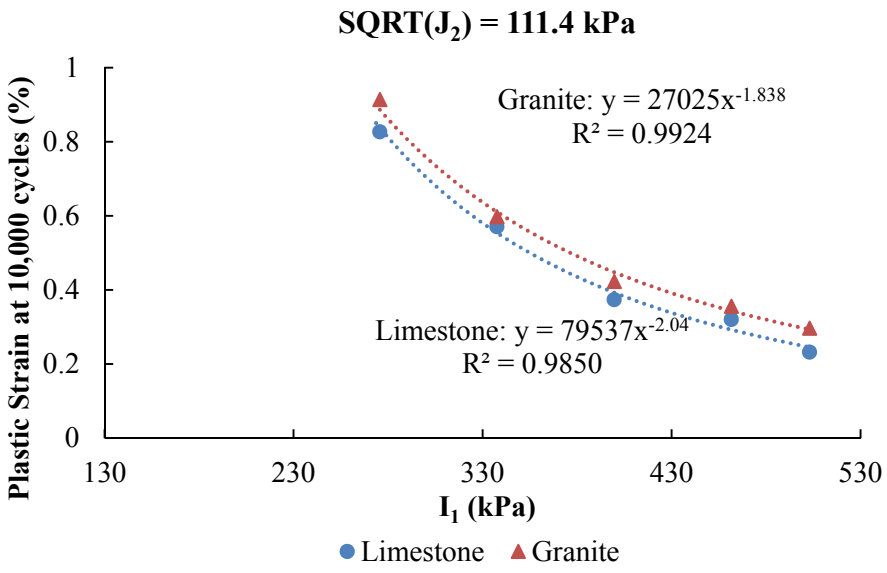


**b. Correlations of $I_1$ with Accumulated Plastic Strain at 10,000 Load Cycles**

**Figure 3.4 Correlations of $J_2$ and $I_1$ with Accumulated Plastic Strain at 10,000 Load Cycles**

The coefficients of the MER model are determined by using the solver function in Microsoft Excel to fit the measured PD curves. Figures 3.5a and 3.5b present comparisons of laboratory-measured and model-predicted accumulated permanent strains at different stress levels for both granite aggregates and limestone aggregates. Stress state is abbreviated as "S" shown in the legend. The recorded permanent strain starts from the 15th load cycle. The root-mean-square errors (RMSEs) are calculated to evaluate the goodness of model fitting at various stress states. In general, a smaller RMSE indicates a better goodness of fitting (Gauch et al. 2003). It is seen that the determined RMSE at each stress level is relatively small, which indicates that the MER model accurately captures the trend of the measured PD curves for both of the tested UGMs. No PD is observed in the hydrostatic stress state 4 for both of the tested materials. Figures 3.5a and 3.5b also show the determined coefficients of the MER model, which can be used to predict the rutting behavior of the tested UGMs at any stress levels and number of load repetitions.

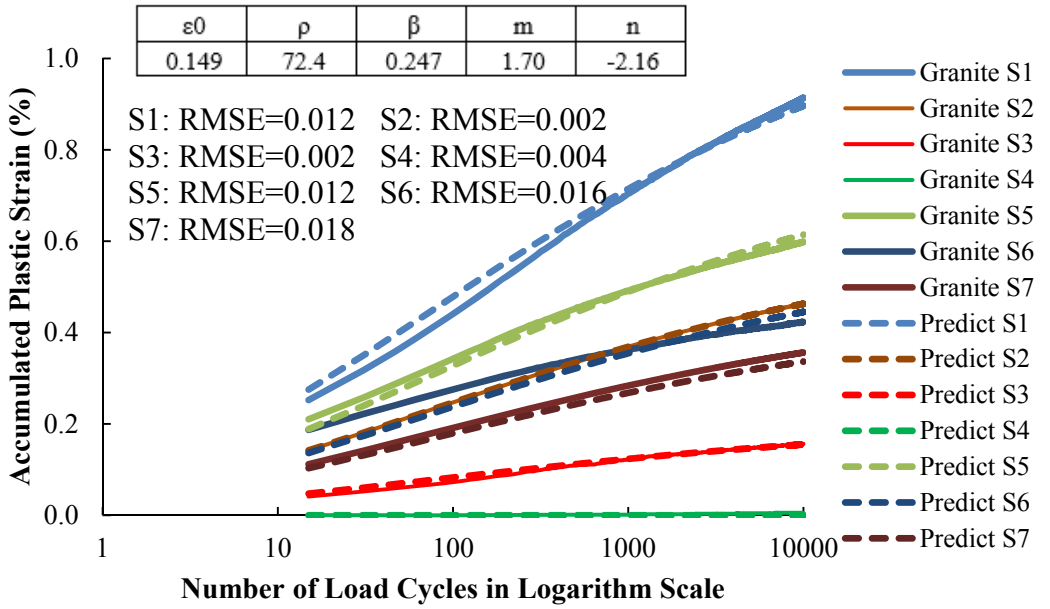


**a. Comparison of Lab-Measured and Proposed Model-Predicted PD curves for Granite Aggregates**

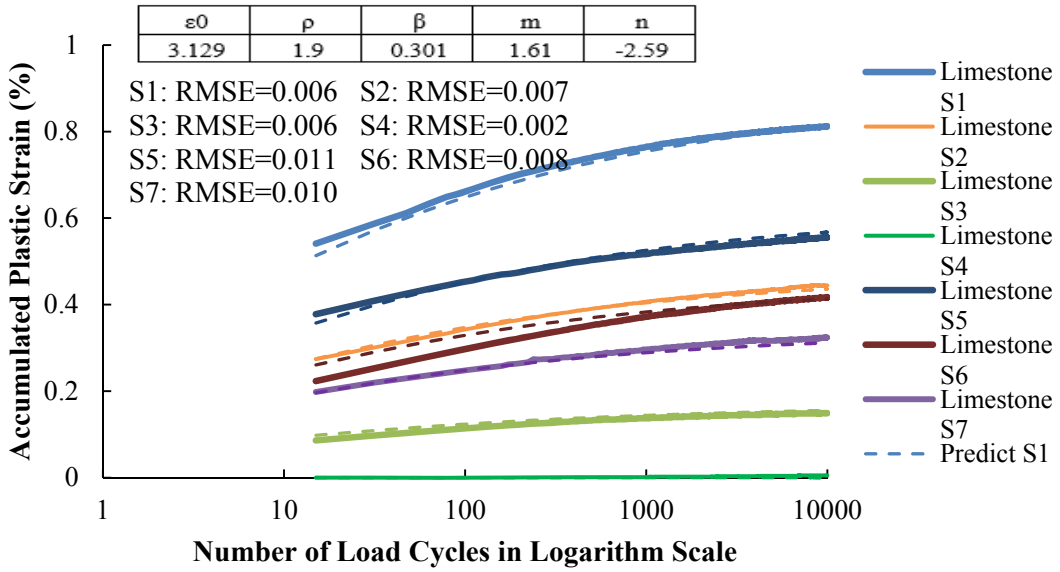


**b. Comparison of Lab-Measured and Proposed Model-Predicted PD curves for Limestone Aggregates**

**Figure 3.5 Comparison of Lab-Measured and Model-Predicted PD Curves**

Using the same regression method and solver function, the coefficients of the K-T model, MEPDG model and UIUC model are also determined based on the RLT test data. Figures 3.6 and 3.7 compare the model predictions with the measured PD at various stress states for both the granite aggregates and limestone aggregates. It is shown that K-T model poorly captures the trend of PD curves for all of the stress states, and the MEPDG model significantly underestimates the PD for most of the stress states. The UIUC model cannot accurately capture the trend of PD curves in the first 1,000 load cycles, but fits well with the PD curves in the rest of the load cycles. Another problem existing in the UIUC model is that the coefficient C is determined as a negative value shown in Figures 3.6c and 3.7c, which conflicts with the fact that a higher deviatoric stress yields a higher PD. The reason for this problem is that both the deviatoric stress and the shear strength ratio (SSR) are softening terms, and the two terms interfere with each other during the model coefficient regression, which further indicates that the softening and hardening behavior of the UGM are not well characterized in the UIUC model. Due to the determined negative values for the coefficient C, the UIUC model cannot be used to predict the PD in the hydrostatic stress state, which has a zero deviatoric shear stress. Compared to the UIUC model, the MER model has smaller RMSEs for both the granite aggregates and limestone aggregates, which indicates the proposed model matches much better with the measured PD curves for all of the load cycles, as shown in Figures 3.5a and 3.5b. Furthermore, the positive m value indicates the softening effect of $J_2$ and the negative n value indicates the hardening effect of $I_1$ on the PD behavior of the UGM.

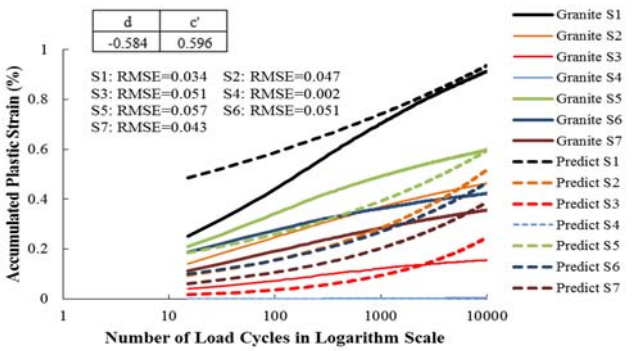


**a. Lab-Measured vs. K-T Model-Predicted PD Curves**

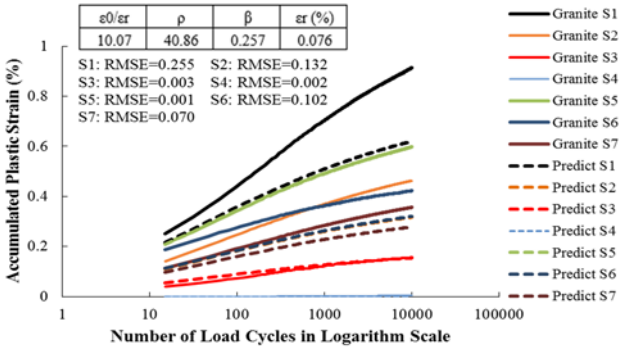


**b. Lab-Measured vs. MEPDG Model-Predicted PD Curves**

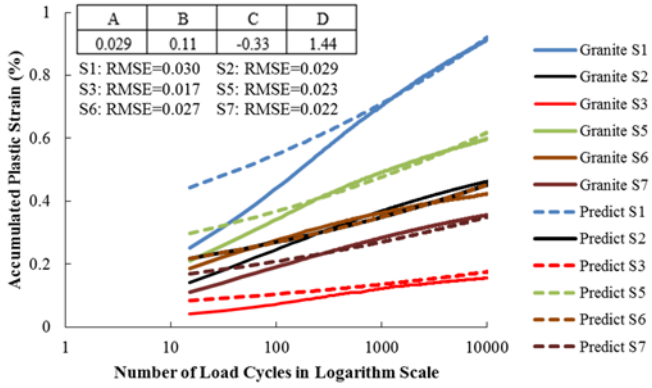


**c. Lab-Measured vs. UIUC Model-Predicted PD Curves**

**Figure 3.6 Comparison of Lab-Measured and Existing Models-Predicted PD Curves for Granite Aggregates**

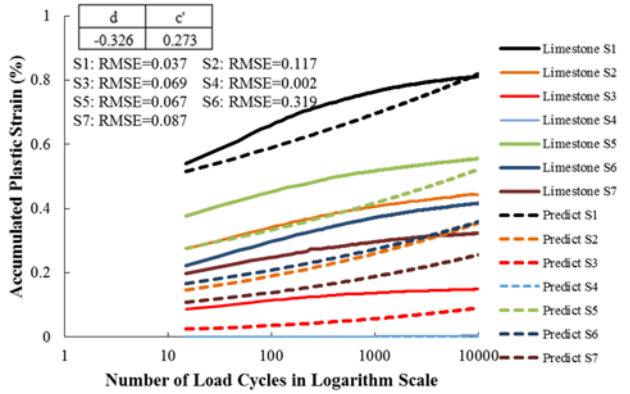


**a. Lab-Measured vs. K-T Model-Predicted PD Curves**

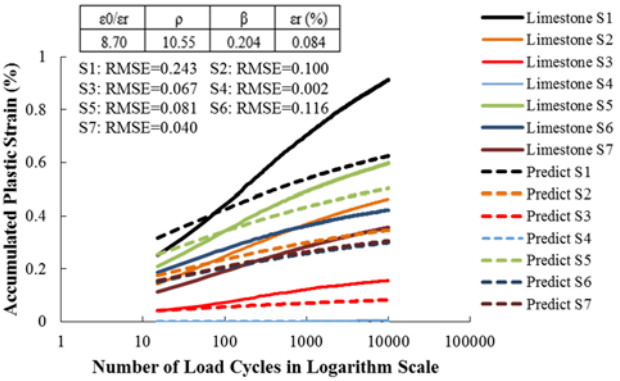


**b. Lab-Measured vs. MEPDG Model-Predicted PD Curves**

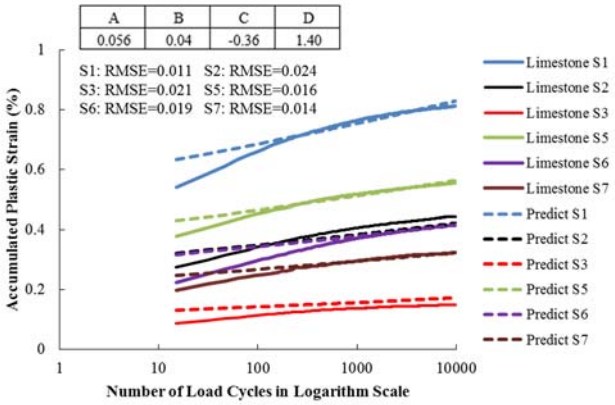


**c. Lab-Measured vs. UIUC Model-Predicted PD Curves**

**Figure 3.7 Comparison of Lab-Measured and Existing Models-Predicted PD Curves for Limestone Aggregates**

## 3.5 Validation of Prediction Accuracy of Rutting Model

Test data from stress states 8 and 9 shown in Table 3.1b are used to validate the prediction accuracy of the rutting models. Figures 3.8a and 3.8b compare the measured PD curves to the MER model-predicted PD curves for both granite aggregates and limestone aggregates by using the determined coefficients shown in Figures 3.5a and 3.5b, respectively. It is seen that the MER model predictions have small RMSE values for the UGMs at the two stress states. Figures 3.8a and 3.8b also compare the measured PD curves with the predictions from the K-T model, UIUC model and MEPDG model. The determined RMSE values of these two models are much higher than those of the MER model for both stress states 8 and 9. This indicates that the proposed model is the best one to predict the rutting behavior of UGMs among these models.

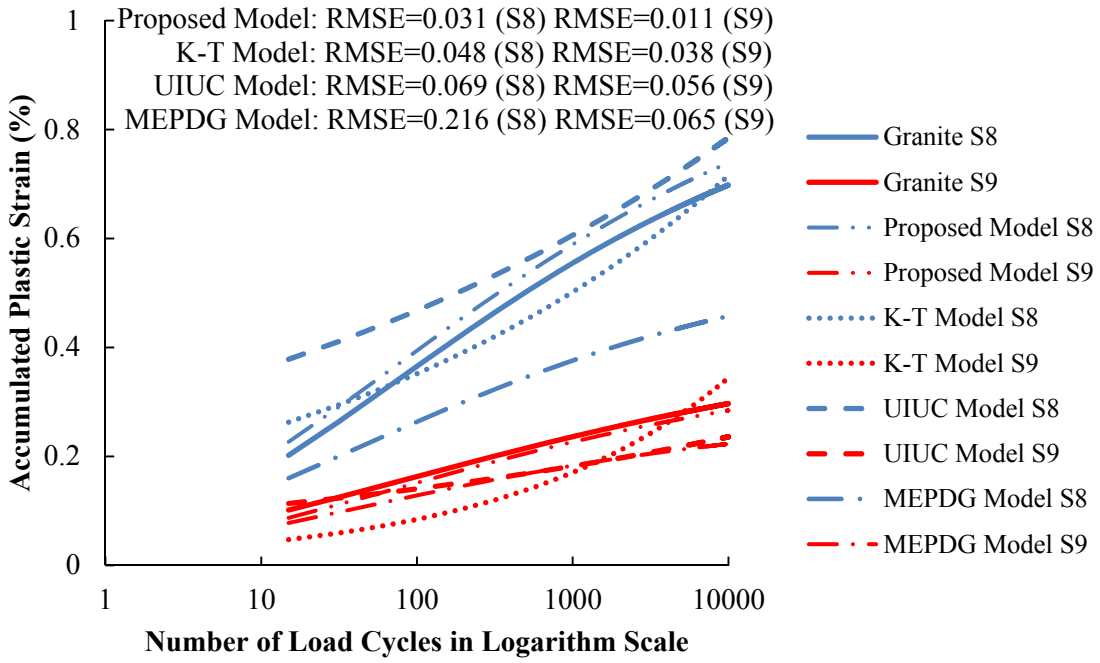


**a. Validation of Prediction Accuracy of Rutting Model for Granite Aggregates**

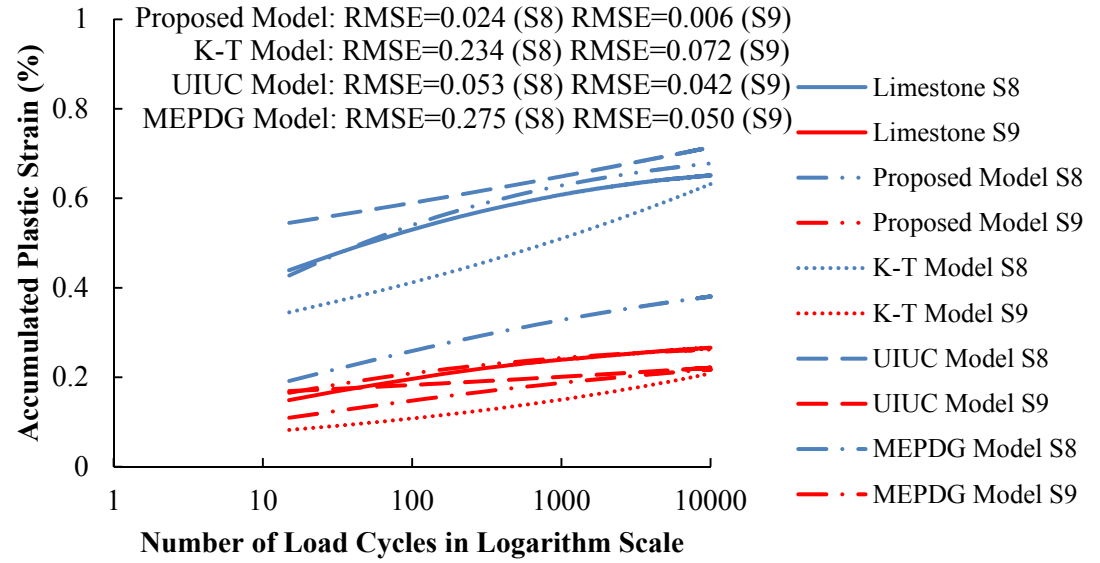


**b. Validation of Prediction Accuracy of Rutting Model for Limestone Aggregates**

**Figure 3.8 Validation of Prediction Accuracy of Rutting Model**

A sensitivity analysis of cohesion $C$ and friction angle $\phi$ on the PD behavior has been conducted in this study, which is shown in Figures 3.9a and 3.9b. It is shown that a higher cohesion $C$ yields a smaller accumulated permanent strain when the friction angle remains constant, and increasing the friction angle $\phi$ also reduces the accumulated permanent strain at a given constant cohesion. It is clear to see that the proposed model is able to discriminate the effects of $C$ or $\phi$ on the PD of the UGM. Theyse (2002) reported that an increasing moisture content does not affect the friction angle of the UGM, but reduces its cohesion. Thus, through the sensitivity analysis, one can deduce that the increasing of moisture content results in a larger accumulated PD, which is consistent with the fact observed in the laboratory and the field. Therefore, the proposed model has a potential ability to evaluate the moisture-sensitivity of the PD behavior of the UGM.

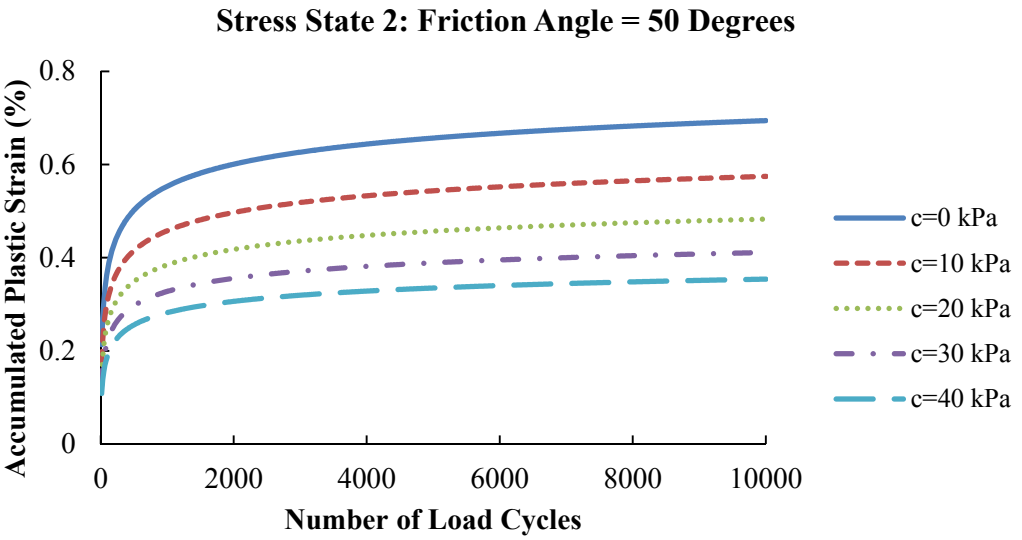


**a. Effect of Cohesion on PD Behavior of UGM**

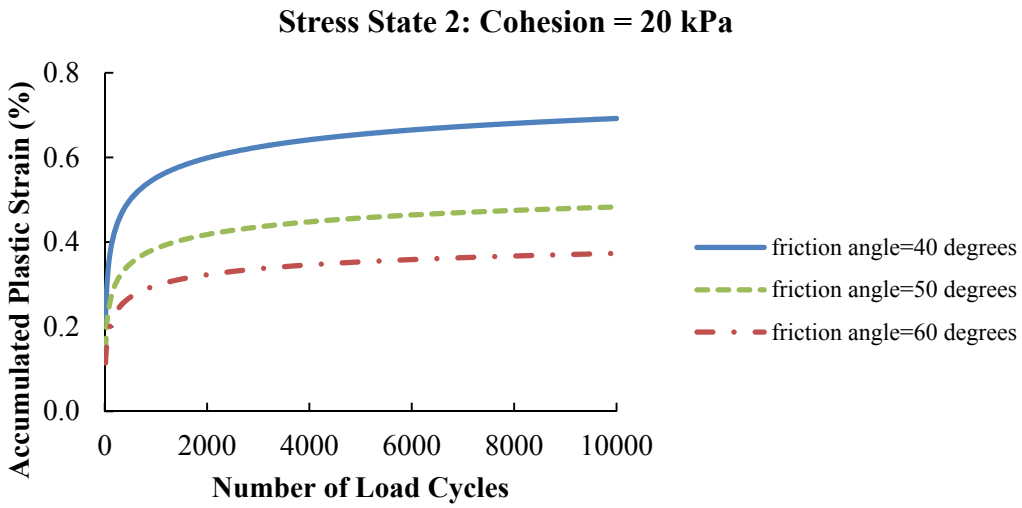


**b. Effect of Friction Angle on PD Behavior of UGM**

**Figure 3.9 Effect of Cohesion and Friction Angle on PD Behavior of UGM**

## 3.6 Model Implementation for Predicting Rut Depth of Flexible Pavement

The validated MER model and the MEPDG model are applied to predict the accumulated rut depth of the base layer in one typical flexible pavement structure, which is illustrated in Figure 3.10. The investigated flexible pavement consists of a 15-cm HMA layer, a 25-cm base course, and subgrade. Figure 3.11 presents the flowchart of the rutting prediction procedure by using the MER model and the MEPDG model. According to the flowchart, one finite element model is created to compute the stress and strain distributions in the base layer when it is subjected to the specified loads, as shown in Figure 3.10. The base layer is characterized as a nonlinear cross-anisotropic material. The nonlinearity indicates that the modulus of the base materials is stress dependent. The cross-anisotropy means that the material properties in the vertical direction are different from those in the horizontal plane, while the properties in the horizontal plane are the same in all directions (Adu-Osei et al. 2001). The reason for this consideration is that a conventional isotropic model always predicts unrealistic horizontal tensile stresses at the bottom of the base layer, while the nonlinear cross-anisotropic model can eliminate the unexpected horizontal tensile stresses from the base layer (Tutumluer and Thompson 1997; Al-Qadi et al. 2010). The cross-anisotropic constitutive model is shown in Equation 3.9 (Zienkiewicz and Taylor 2000).

$$\begin{bmatrix}\sigma_x\\ \sigma_y\\ \sigma_x\\ \tau_{xy}\end{bmatrix}=\frac{E_y}{\alpha\beta}\begin{bmatrix} s\left(1-s\nu_{yx}^2\right) & s\nu_{yx}\alpha & s\left(\nu_{xx}+s\nu_{yx}^2\right) & 0\\ s\nu_{yx}\alpha & 1-\nu_{xx}^2 & s\nu_{yx}\alpha & 0\\ s\left(\nu_{xx}+s\nu_{yx}^2\right) & s\nu_{yx}\alpha & s\left(1-s\nu_{yx}^2\right) & 0\\ 0 & 0 & 0 & r\alpha\beta\end{bmatrix}\begin{bmatrix}\varepsilon_x\\ \varepsilon_y\\ \varepsilon_x\\ \frac{1}{2}\gamma_{xy}\end{bmatrix} \tag{3.9}$$

where $s = \frac{E_x}{E_y}$; $r = \frac{G_{xy}}{E_y}$; $\alpha = 1 + \nu_{xx}$; $\beta = 1 - \nu_{xx} - 2s\nu_{yx}^2$; $E_x$ is the horizontal modulus; $E_y$ is the vertical modulus; $G_{xy}$ is the shear modulus; $\nu_{yx}$ is the Poisson's ratio to characterize the effect of vertical strain on horizontal strain; $\nu_{xx}$ is the Poisson's ratio to characterize the effect of horizontal strain on orthogonal horizontal strain. Equation 3.10 is used to characterize the nonlinear stress dependent behavior of vertical modulus (NCHRP 2003).

$$E_y = k_1 P_a \left(\frac{I_1}{P_a}\right)^{k_2} \left(\frac{\tau_{oct}}{P_a}\right)^{k_3} \tag{3.10}$$

where $I_1$ = the first invariant of the stress tensor; $P_a$ = the atmospheric pressure; $\tau_{oct}$ = the octahedral shear stress; and $k_1$ , $k_2$ and $k_3$ are regression coefficients. In order to simplify the model, the asphalt layer and subgrade are herein assumed as linear elastic materials. The model inputs of the material properties are presented in Figure 3.10. The input nonlinear cross-anisotropic properties are determined on the basis of experimental measurements. Note that three representative values of $k_1$, i.e., 1081, 1281 and 1481 are used in the analysis, which correspond to the low, medium and high resilient moduli of the base material. Figures 3.12a, 3.12b and 3.12c show the computed distributions of the vertical strain, vertical stress, and horizontal stress in the base layer at the centerline of the load.

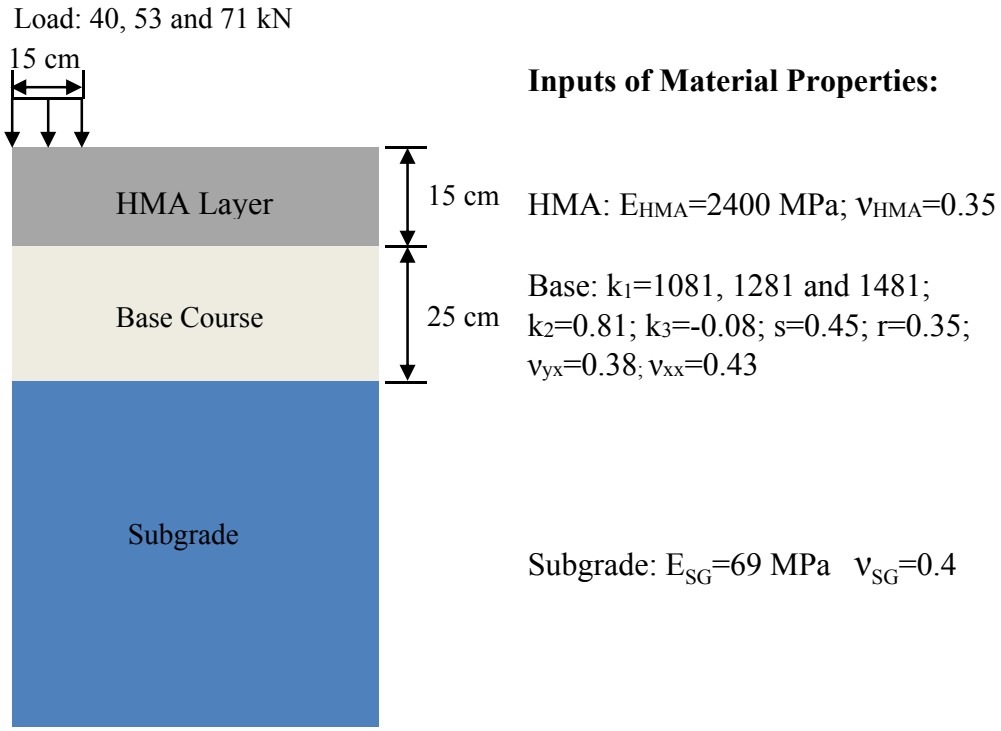


**Figure 3.10 Illustration of Investigated Pavement Structure and Corresponding Material Properties**

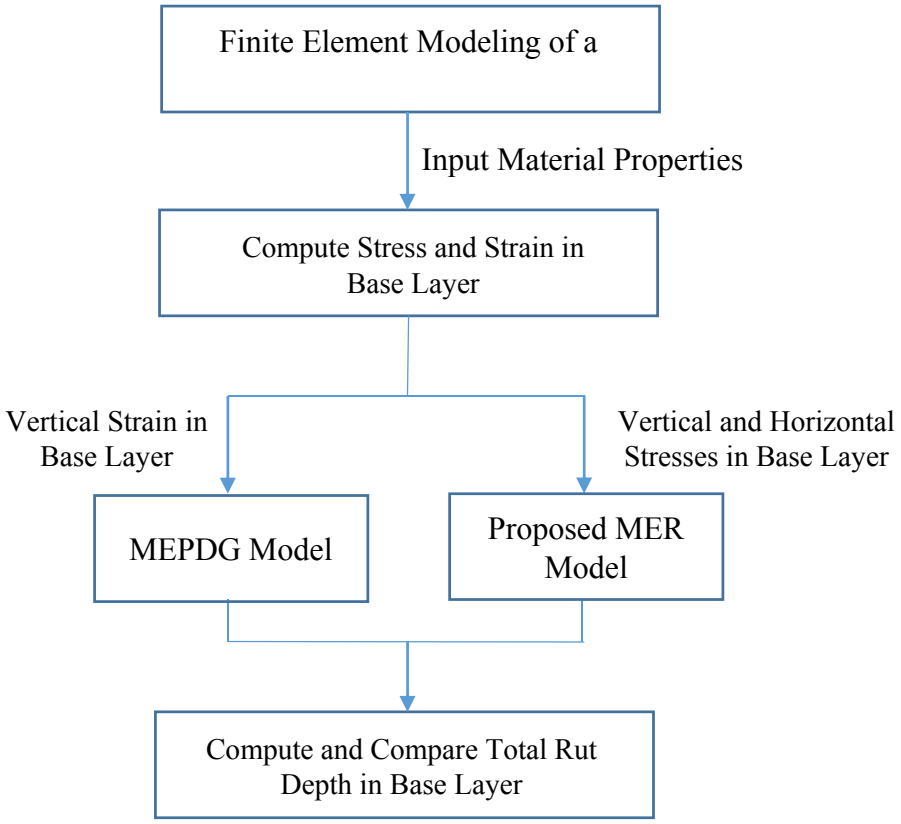


**Figure 3.11 Flowchart of Rutting Prediction Procedure**

After obtaining the stress and strain distributions in the base layer, the multi-layered incremental approach is employed to compute the total rut depth. The following equations explain how the total rut depth of the base layer is computed using the MER model and the MEPDG model, respectively.

MER Model:

$$\delta_{base}(N) = \int_0^h \varepsilon_0 e^{-\left(\frac{\rho}{N}\right)^{\beta}} \left(\sqrt{J_2(z)}\right)^m \left(\alpha I_1(z) + K\right)^n dz \qquad (3.11)$$

MEPDG Model:

$$\delta_{base}(N) = \int_0^h \frac{\varepsilon_0}{\varepsilon_r} e^{-\left(\frac{\rho}{N}\right)^{\beta}} \varepsilon_v(z)\,dz \tag{3.12}$$

where $\delta_{base}$ is the total rut depth in base, $h$ is the thickness of the base layer, and $z$ is the depth within the base layer. The coefficients of these two models are shown above in Figures 3.5a and 3.6b, respectively. Figure 3.12d presents the results of the computed rut depths by the MEPDG model and the proposed model using the computed stress and strain distributions shown in Figures 3.12a, 3.12b and 3.12c. It is indicated that the predicted rut depth by the proposed model is higher than that by the MEPDG model. This is consistent with the result shown in Figure 3.6b that the MEPDG model underestimates the PD behavior of the tested UGM. Figures 3.13a and 3.13b present the sensitivity analysis of the computed rut depth using the MEPDG model and the MER model by varying the load magnitude and resilient modulus of the base material, respectively. As can be seen from Figure 3.13a, the MEPDG model and the MER model both exhibit the same trend that enhancing load magnitude increases the accumulated rut depth of the base layer at 100,000 load cycles. At a 560 kPa load level, the computed rut depth by the MER model is 0.07 cm greater than that predicted by the MEPDG model; while at a 1000 kPa load level, the difference in predicted rut depth increases to 0.13 cm. This indicates that the proposed model is much more sensitive than the MEPDG model to the variation of load magnitude. As shown in Figure 3.13b, both models predict higher rut depths when using the lower base modulus (i.e. $k_1$=1081). It is also seen that the

proposed MER model is somewhat more sensitive than the MEPDG model to the change of base modulus.

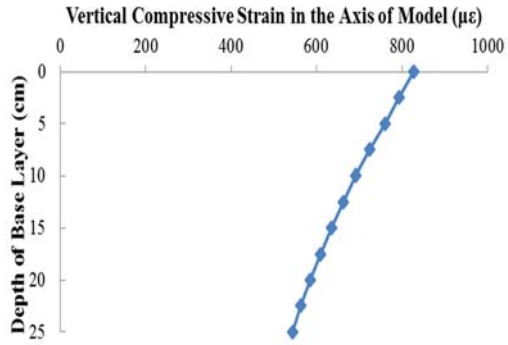


**a. Vertical Compressive Strain Distribution in Base Layer**

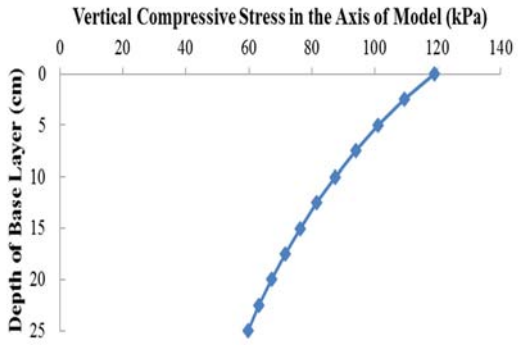


**b. Vertical Compressive Stress Distribution in Base Layer**

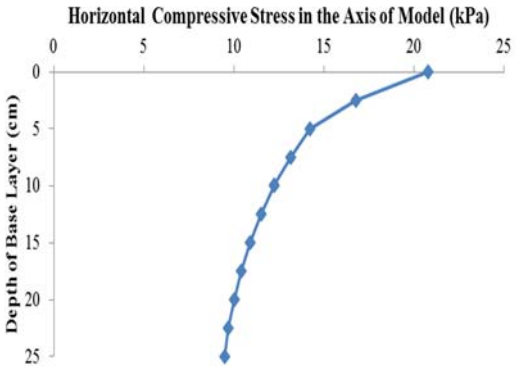


**c. Horizontal Compressive Stress Distribution in Base Layer**

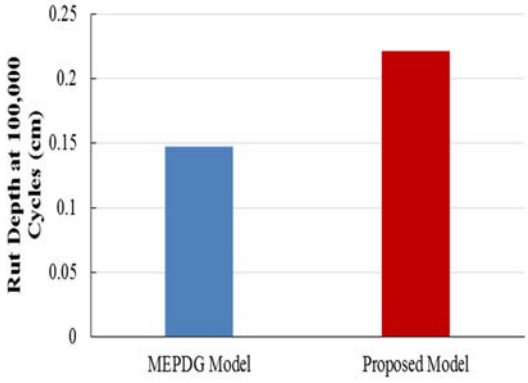


**d. Computed Rut Depth Using MEPDG Model and Proposed Model**

**Figure 3.12 Computation of Rut Depth Using MEPDG Model and Proposed Model**

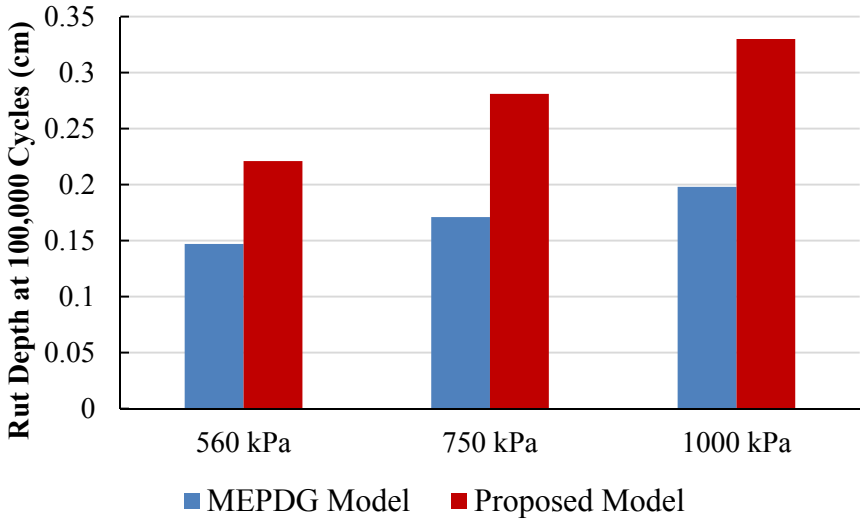


**a. Effect of Load Magnitude on Computed Rut Depth**

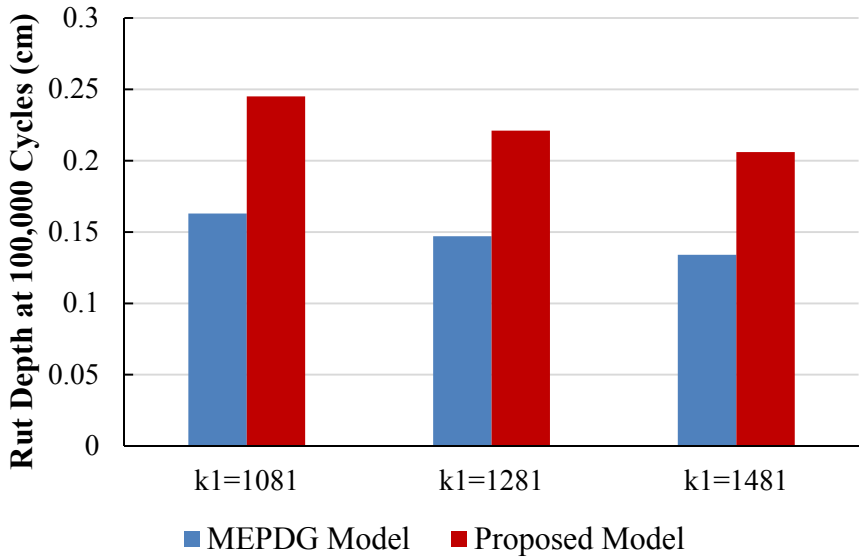


**b. Effect of Base Modulus on Computed Rut Depth**

**Figure 3.13 Sensitivity Analysis of Computed Rut Depth Using MEPDG Model and Proposed Model**

# 4. INVESTIGATION OF PERFORMANCE-RELATED BASE COURSE PROPERTIES

## 4.1 Introduction

Current engineering design and the expected service life of pavements are based upon the modulus values of the individual pavement layers. In the design process, the layer modulus may either be assumed based upon experience or taken from laboratory tests of the materials that are expected to be used in the construction of the pavement or upon modulus values that have been inferred from nondestructive testing of in-service pavements. In the construction of each pavement layer, the objective should be to assure that layer is built so that its modulus matches as closely as possible the modulus that was used in its design.

However, the properties of the base course layer that are measured during the construction are rarely, if ever, the modulus which was the basis of design. Most commonly it is the dry unit weight and water content which are compared with laboratory compaction curves to assure that an adequate level of compaction has been achieved. For decades, it has been recognized that there is a need to assure that the properties of base courses that were used in design are what have actually been placed.

A major obstacle to achieving this desired result is the difficulty of measuring the modulus and even more difficult, the permanent deformation properties of the base course properties. What is needed is a quick, accurate and simple process for determining reliable values of the in-place as compacted base course modulus and permanent deformation properties.

It is with this objective in view that the measurements presented in this chapter were undertaken. Samples of base course materials were taken from several quarries around Texas and tested to determine their stress-dependent resilient moduli and permanent deformation properties. In addition to these properties, other, simpler and quicker tests of the characteristics of the same base course aggregates were made to determine if there were any that were sound, repeatable and reliable predictors of the performance-related properties of base course aggregates. These tests include the methylene blue test developed by the Grace corporation, the Horiba particle size analyzer to determine the percent fines content of the base course, the filter paper test to determine the suction of the base course, the sieve analysis to determine the gradation of the particle sizes, and the aggregate imaging system (AIMS) test to determine the shape, angularity and texture of the aggregates.

## 4.2 Selection of Performance Testing for Base Course Properties

Selection of performance-related base course indicators is a key to accurately estimate the performance of unbound aggregates. There are many property indicators used to characterize the flexible base materials. Typical properties used in Texas include particle size gradation, plasticity index (PI), liquid limit, wet ball mill value, maximum dry density and optimum moisture content (Epps et al. 2014). Other properties used by other specifying agencies include LA abrasion value and sand equivalent. Among these properties, particle size gradation, maximum dry density and optimum moisture content are considered as basic property indicators. Wet ball mill value and LA abrasion are used

specially to evaluate the durability of coarse aggregates, while Atterberg limits and sand equivalent are applied to fine aggregates. However, these properties are empirical indicators, which are not directly related to the performance of flexible base materials.

In recent years, many performance-related tests are investigated to evaluate flexible base materials, including AIMS test, methylene blue test, and percent fines content (PFC) test. The AIMS test is used to characterize the shape, angularity and texture properties of coarse aggregates (Masad et al. 2005; Ashtiani et al. 2008). These aggregate morphological indices are successfully linked to the resilient behavior and the permanent deformation trend of aggregate materials. The aggregates with higher composite angularity index and surface texture index were found to have a higher resilient modulus. The cubic-shaped aggregates were found to be more susceptible to permanent deformation than the crushed aggregates. The aggregate matrix specimens with lower angularity index and surface texture index correspond to a higher permanent strain in the base course (Barksdale and Itani 1994; Tutumluer and Pan 2008). The methylene blue test is used to measure the amount of moisture active clay particles in the aggregate matrix (Ashtiani 2009; AASHTO 2007). It is proven that the test has less variability compared to the PI test (Sahin et al. 2015). The higher methylene blue value (MBV) indicates that the fines in the base material have higher plasticity, which has negative effect on the performance of the base course. For example, the expected performance of the base course is considered by AASHTO T330 to be a failure when the MBV is higher than 20 (AASHTO 2007). The PFC test is used to evaluate the total clay content in fine aggregates. Clay is defined as the particles smaller than 2 microns

according to the identification and classification of soils. The clay content is a critical factor that controls moisture susceptibility, swelling, shrinkage, and plasticity of soils, which affects the performance of flexible bases (Mishara and Tutumluer 2012; Sahin 2011).

Based on the aforementioned research findings, the following performance-related base course properties are selected in this section: dry density, optimum moisture content, MBV, PFC, gradation of particles, and shape, angularity and texture of aggregates in terms of Weibull distribution parameters. These performance-related properties are applied to characterize the flexible base materials and to develop the prediction models for the resilient modulus and permanent deformation properties of the base course.

## 4.3 Candidate Tests for Aggregates Characteristics

### *4.3.1 Methylene Blue Test*

Because of its high repeatability and reproducibility (Epps, et al. 2014), the W.R Grace methylene blue test method is applied to determine the MBVs of each kind of base material instead of the AASHTO T 330 standard test (AASHTO 2007). The 20 grams of fine materials passing through the No.4 sieve is first added to a 30 ml methylene blue solution. The sample is then mixed for 5 minutes by the shaking machine. Subsequently, the solution is injected into a 2 um filter and the filtered solution is mixed with 45ml distilled water. Finally, the variation of the solution color measured

by a colorimeter is used to determine the MBV. Figure 4.1 shows the devices used for the Methylene Blue test.

**Figure 4.1 Test Devices for Methylene Blue Test**

### *4.3.2 Aggregate Imaging System Test*

The AIMS test device is a system comprised of a computer, image acquisition hardware, a high-resolution camera, microscope, aggregate tray and lighting system. It is used to characterize the morphology of coarse aggregates, including shape, angularity and surface texture. Aggregate shape characterizes the flatness and elongation of aggregate particles. Angularity evaluates the degree of roundness of aggregate corners. Surface texture defines the roughness of aggregate surfaces. In this section, the washed

coarse aggregates are separated by the No.1/2, No. 3/8, and No.4 size sieves. The materials retained on each sieve are placed in the aggregate tray and scanned by high-resolution camera. The distributions of angularity, shape, and surface texture indices are measured from this test. Figure 4.2 shows the configuration of AIMS test.

**Figure 4.2 Configuration of Aggregate Imaging System Test**

### *4.3.3 Percent Fines Content Test*

Horiba laser scattering particle size distribution analyzer is used to determine percent fines content of aggregates (Sahin 2011). A viscous solution made of the particles passing through the No.200 sieve and water flows through a beam of light. The

light scattering device analyzes the dimensions of various particles in the solution and generates a particle size distribution from the smallest to the largest particle dimension. The configuration of particle size distribution analyzer is shown in Figure 4.3.

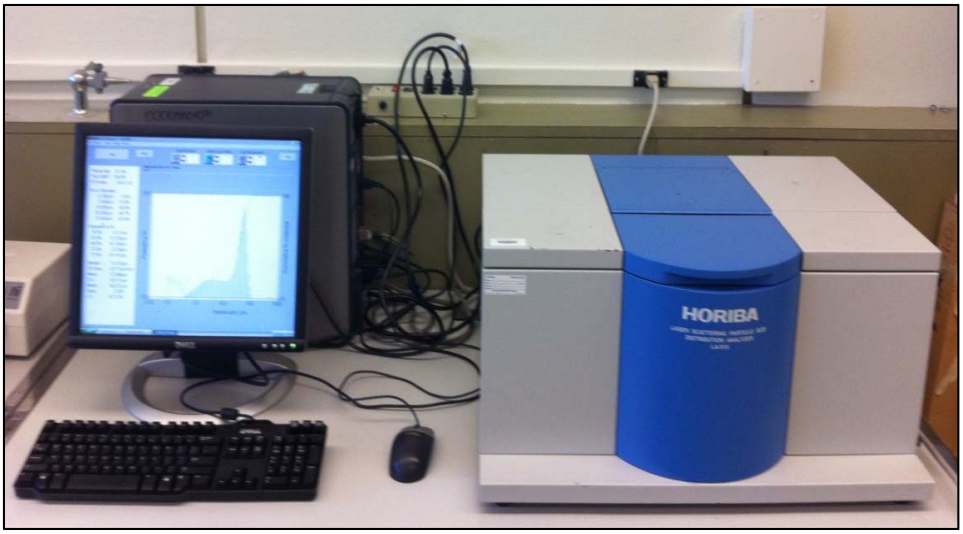


**Figure 4.3 Configuration of Laser Scattering Particle Size Distribution Analyzer**

## 4.4 Characterization of Performance-Related Base Course Properties

Base course materials used in this study are selected from 9 quarries around Texas. These quarries are selected in attempts to capture the geographic, mineralogical, and production volume diversity of typical sources used for Texas Department of Transportation (TxDOT) projects. In order to investigate the variability of material production, some kinds of base materials are picked up twice from the same quarry at

different times, denoted with “01” for the first time, “02” for the second time and “03” for the third time. Table 4.1 summarizes the source of material used for laboratory testing.

**Table 4.1 Sources of Material for Laboratory Testing**

| Source Type | Rock Type | Production Size |
|---|---|---|
| A01 | Limestone | Large |
| A02 | Limestone | Large |
| A03 | Limestone | Large |
| B01 | Limestone | Large |
| B02 | Limestone | Large |
| C01 | Sandstone | Large |
| C02 | Sandstone | Large |
| C03 | Sandstone | Large |
| D01 | Limestone | Small |
| D02 | Limestone | Small |
| E01 | Limestone | Medium |
| F01 | Limestone | Large |
| F02 | Limestone | Large |
| F03 | Limestone | Large |
| G01 | Limestone | Large |
| G02 | Limestone | Large |
| H01 | Limestone | Medium |
| H02 | Limestone | Medium |
| I01 | Caliche | Small |
| I02 | Caliche | Small |

Figure 4.4 shows the distributions of angularity index, shape and surface texture for the I01 aggregate retained on No.1/2, No 3/8 and No, 4 sieves. Since the aggregate matrix is composed of these different sizes of aggregates, the composite angularity,

shape and surface texture indices are used to characterize the morphologies of the blended coarse aggregates. The calculation of composite angularity, shape and surface texture indices are shown in Equation 4.1:

$$\text{Composite Index} = \frac{\sum_{i=1}^{n}\left[(a_i)(\text{index}_i)\right]}{\sum_{i=1}^{n}(a_i)} \tag{4.1}$$

where $Composite\ Index$ is composite angularity, shape, or surface texture index for a certain aggregate blend, respectively; $a_i$ is the volume percentage of the i$^{th}$ size aggregate blended in the aggregate matrix; and $index_i$ is the angularity, shape, or surface texture indices for a given size aggregate (Tutumluer and Pan 2008). The distributions of the composite angularity, shape and surface texture indices are also presented in Figure 4.4.

In order to quantify the AIMS test results, a known statistical distribution is fitted to the distributions measured from the AIMS test. The cumulative Weibull distribution is adopted in this study, which is shown in Equation 4.2:

$$F\left(x;a,\lambda\right)=1-e^{-\left(x/\lambda\right)^{a}} \tag{4.2}$$

where $F\left(x;a,\lambda\right)$ is the cumulative probability; $x$ is the composite angularity, shape, or surface texture indices; $\lambda$ is the scale parameter; and $a$ is the shape parameter (Montgomery and Runger 2007). The determined shape parameter $a$ and scale parameter $\lambda$ are used to quantify the AIMS test results. Figure 4.5 shows the plot of the measured cumulative distributions and the fitted cumulative Weibull distributions. A good agreement is observed between the fitted cumulative Weibull distributions and the

measured ones. This indicates that the Weibull distribution is suitable to analyze the AIMS test results. The AIMS test results are presented from the 3th to 10th column in Table 4.2. The subscripts in these columns denote the following: G is for gradation; A is for angularity; S is for shape; and T is for texture.

Percent fines content test and methylene blue test are used to characterize the amount and quality of moisture active clay in fine aggregates. Figure 4.6 shows the fine particle size distribution for I01. The solid line is the cumulative distribution curve. The percent fines content is calculated according to Equation 4.3.

$$\text{Percent Fines Content } (pfc) = \frac{m_{2\mu m}}{m_{75\mu m}} \tag{4.3}$$

where $m_{2\mu m}$ is the mass of aggregate smaller than 2 microns; $m_{75\mu m}$ is the mass of aggregate smaller than 75 microns. In Table 4.2, the 2nd column lists the results of the percent fines content test. Methylene blue test results can be used directly as variables in the k-values prediction analysis, which are listed in the 1st column of Table 4.2.

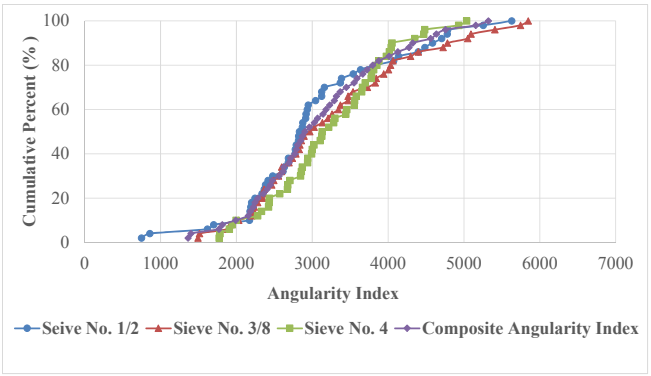


**a. Distribution of Angularity Index**

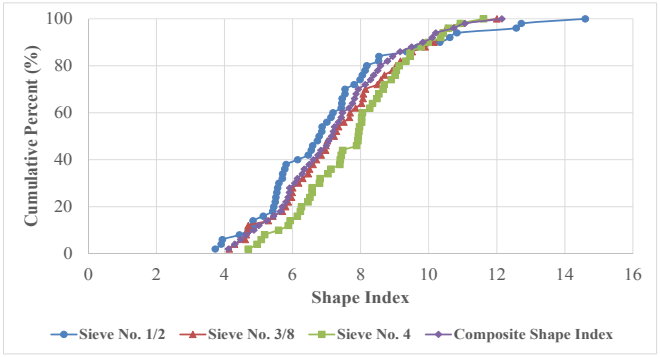


**b. Distribution of Shape Index**

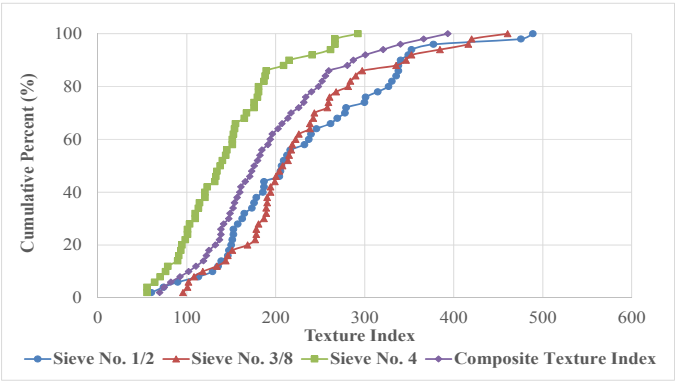


**c. Distribution of Texture Index**

**Figure 4.4 Example of Distributions of Angularity Shape and Surface Texture Index**

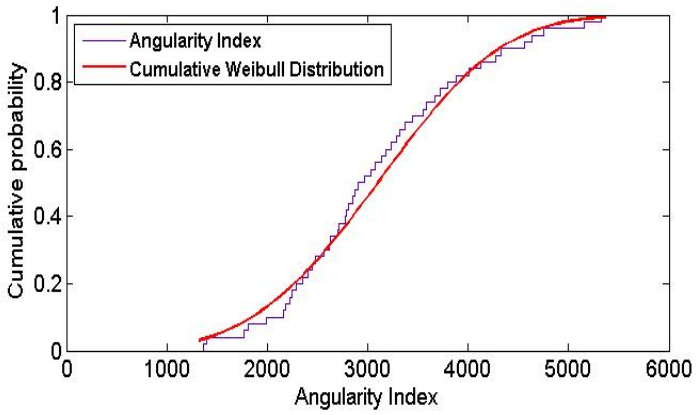


**a. Cumulative Weibull Distribution of Angularity Index**

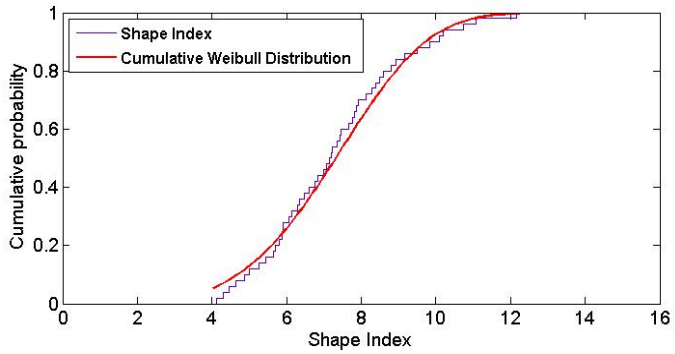


**b. Cumulative Weibull Distribution of Shape Index**

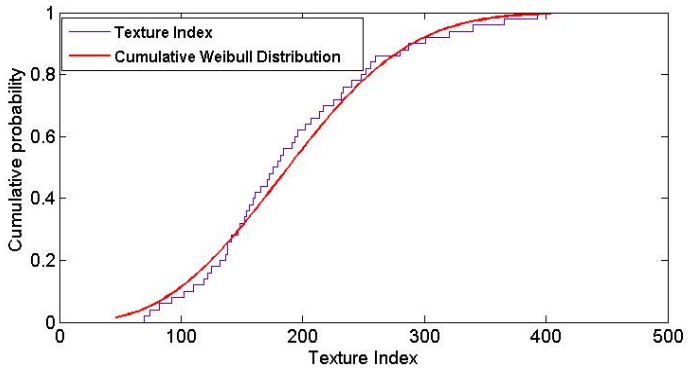


**c. Cumulative Weibull Distribution of Texture Index**

**Figure 4.5 Comparison of Fitted Weibull Distributions and Measured Composite Index Distributions**

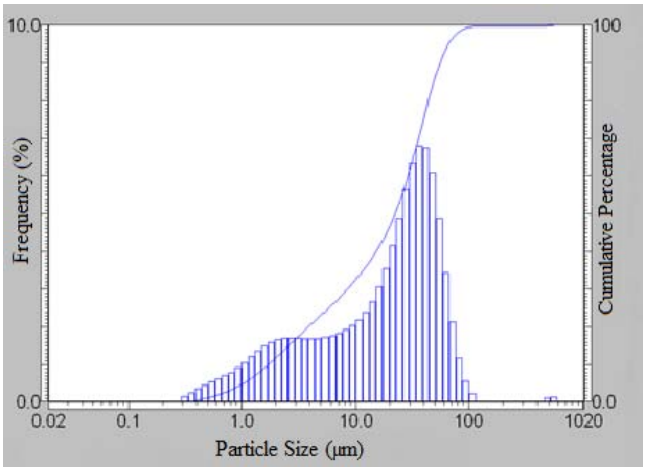


**Figure 4.6 Example of Fine Particle Size Distribution**

**Table 4.2 Databases of Measured Base Course Properties**

| Material Type | MBV | PFC | Gradation | | Angularity | | Shape | | Texture | |
|---|---|---|---|---|---|---|---|---|---|---|
| | | | $a_G$ | $\lambda_G$ | $a_A$ | $\lambda_A$ | $a_S$ | $\lambda_S$ | $a_T$ | $\lambda_T$ |
| A01 | 7.1 | 13.2 | 0.73 | 10.6 | 4.76 | 3328.0 | 4.44 | 8.9 | 2.93 | 174.6 |
| A02 | 6.4 | 12.3 | 0.67 | 9.6 | 4.76 | 3328.0 | 4.44 | 8.9 | 2.93 | 174.6 |
| A03 | 4.3 | 13.2 | 0.70 | 9.1 | 4.76 | 3328.0 | 4.44 | 8.9 | 2.93 | 174.6 |
| B01 | 2.7 | 21.5 | 0.72 | 10.4 | 3.79 | 3291.5 | 3.96 | 7.8 | 2.12 | 165.8 |
| B02 | 2.5 | 20.3 | 0.70 | 10.0 | 3.79 | 3291.5 | 3.96 | 7.8 | 2.12 | 165.8 |
| C01 | 5.3 | 11.4 | 0.87 | 14.6 | 5.09 | 3113.1 | 4.11 | 8.6 | 2.51 | 194.1 |
| C02 | 3.7 | 13.0 | 0.86 | 15.7 | 5.09 | 3113.1 | 4.11 | 8.6 | 2.51 | 194.1 |
| C03 | 3.3 | 12.0 | 0.80 | 16.0 | 5.09 | 3113.1 | 4.11 | 8.6 | 2.51 | 194.1 |
| D01 | 16.4 | 12.7 | 0.93 | 10.3 | 5.10 | 3072.9 | 3.65 | 8.0 | 1.96 | 171.5 |
| D02 | 13.7 | 13.2 | 0.98 | 12.2 | 5.10 | 3072.9 | 3.65 | 8.0 | 1.96 | 171.5 |
| E01 | 3.1 | 13.3 | 0.90 | 11.3 | 3.75 | 3228.1 | 4.48 | 7.6 | 1.75 | 205.5 |
| F01 | 7.0 | 15.5 | 0.85 | 12.7 | 4.50 | 3210.5 | 4.63 | 8.0 | 1.86 | 138.8 |
| F02 | 7.6 | 15.8 | 0.85 | 13.1 | 4.53 | 3210.5 | 4.63 | 8.0 | 1.86 | 138.8 |
| F03 | 6.4 | 14.7 | 0.79 | 12.2 | 4.53 | 3210.5 | 4.63 | 8.0 | 1.86 | 138.8 |
| G01 | 6.8 | 13.6 | 0.88 | 10.8 | 4.99 | 3342.8 | 3.63 | 8.7 | 1.48 | 205.6 |
| G02 | 2.8 | 15.0 | 1.02 | 13.1 | 4.99 | 3342.8 | 3.63 | 8.7 | 1.48 | 205.6 |
| H01 | 5.0 | 16.1 | 0.89 | 8.3 | 4.38 | 3336.9 | 4.66 | 8.2 | 3.16 | 287.6 |
| H02 | 10.1 | 19.7 | 1.02 | 11.0 | 4.38 | 3336.9 | 4.66 | 8.2 | 3.16 | 287.6 |
| I01 | 18.5 | 22.8 | 0.75 | 9.9 | 3.25 | 3633.4 | 4.27 | 8.2 | 2.87 | 253.9 |
| I02 | 18.5 | 22.8 | 0.46 | 6.7 | 3.25 | 3633.4 | 4.27 | 8.2 | 2.87 | 253.9 |

## 4.5 Performance Prediction for Base Materials Using Performance-Related Base Course Properties

### *4.5.1 Prediction of Resilient Modulus for Base Materials*

The constitutive model shown in Equation 4.4 is used to determine the resilient modulus of base material at any specific stress state and moisture content.

$$E_y = k_1 P_a \left(\frac{I_1 - 3\theta f h_m}{P_a}\right)^{k_2} \left(\frac{\tau_{oct}}{P_a}\right)^{k_3} \tag{4.4}$$

where $I_1$ = the first invariant of the stress tensor; $P_a$ = the atmospheric pressure; $\theta$ = the volumetric water content; $h_m$ = the matric suction in the aggregate matrix; $f$ = the saturation factor, $1 \le f \le \frac{1}{\theta}$; $\tau_{oct}$ = the octahedral shear stress; and $k_1$ , $k_2$ and $k_3$ are model parameters that are dependent on material properties of the base course. Repeated load tests are used to measure the resilient moduli of the selected base materials at specific stress state and optimum moisture content. Solver Function in the software Excel is employed to determine the values of $k_1$, $k_2$ and $k_3$ in Equation 4.4. Table 4.3 lists the determined k-values as well as associated matric suction values and the corresponding R-squared values for each specimen.

Multiple regression analysis is performed using the JMP software to investigate the correlation between the k values and the base course properties, including the dry density ($\gamma_d$), water content ($w$), MBV, PFC, and aggregate gradation, angularity, shape and texture in terms of the shape parameter $a$ and the scale parameter $\lambda$ in the Weibull distribution. Compared to plasticity index, liquid limit and $P_{200}$, these selected base

course properties are much more directly related to pavement performance (Pan et al. 2006). The measurements of these performance-related base course properties are quicker, more accurate, repeatable and reliable. The data of base course properties used in the development of the prediction models are presented in Table 4.3.

**Table 4.3 Test Results for Aggregate Specimens at Optimum Moisture Content**

| Source Type | $k_1$ | $k_2$ | $k_3$ | Matric Suction (kPa) | $R^2$ |
|---|---|---|---|---|---|
| A01 | 1206.3 | 0.72 | -0.03 | -50.1 | 0.89 |
| A02 | 1198.2 | 0.84 | -0.02 | -39.8 | 0.91 |
| A03 | 1000.2 | 0.90 | -0.03 | -29.8 | 0.92 |
| B01 | 689.1 | 1.31 | -0.16 | -20.0 | 0.99 |
| B02 | 772.4 | 1.25 | -0.14 | -41.0 | 0.98 |
| C01 | 299.2 | 1.05 | -0.07 | -100.0 | 0.99 |
| C02 | 349.6 | 1.10 | -0.07 | -100.0 | 0.99 |
| C03 | 415.8 | 1.06 | -0.06 | -76.2 | 0.99 |
| D01 | 386.2 | 1.44 | -0.10 | -125.9 | 0.93 |
| D02 | 544.0 | 1.21 | -0.12 | -79.4 | 0.94 |
| E01 | 1206.0 | 0.87 | -0.03 | -63.1 | 0.99 |
| F01 | 456.7 | 1.21 | -0.12 | -63.1 | 0.93 |
| F02 | 442.3 | 1.30 | -0.10 | -63.1 | 0.88 |
| F03 | 652.4 | 1.00 | -0.09 | -41.2 | 0.94 |
| G01 | 1464.5 | 0.78 | -0.05 | -39.8 | 0.93 |
| G02 | 1072.5 | 1.02 | -0.08 | -100 | 0.96 |
| H01 | 2440.2 | 0.36 | 0.00 | -63.1 | 0.92 |
| H02 | 1928.2 | 0.71 | -0.03 | -63.1 | 0.96 |
| I01 | 773.9 | 0.74 | -0.10 | -316.2 | 0.97 |
| I02 | 563.5 | 0.63 | -0.15 | -363.2 | 0.96 |

A stepwise multiple regression analysis is performed to detect the significant material properties of the base course for modeling $k_1$, $k_2$ and $k_3$. The p-value obtained from the t-test is used to identify the significant variables in the model. A p-value less than 0.05 indicates that the variable is significant at a 95 percent confidence level. Table 4.4 presents the results produced by the JMP software. The t-ratio is a ratio of the departure of an estimated parameter from its notional value and its standard error. A higher absolute value of the t-ratio corresponds to a smaller obtained p-value. It is shown that the dry density, shape, angularity and texture of the aggregates, and the percent fines content are significant variables in the prediction models. Equations 4.5 to 4.7 are the prediction models for $k_1$, $k_2$, and $k_3$, respectively, from the regression analysis.

$$\ln k_1 = -137.19 + 13.60\ln(\gamma_d) + 4.35\ln(\lambda_A) - 0.62\lambda_S + 1.68\ln(\lambda_T) \tag{4.5}$$

$$k_2 = 36.14 + 0.04\,pfc - 3.81\ln\left(\lambda_A\right) - 0.22a_S - 0.77\ln\left(\lambda_T\right) \tag{4.6}$$

$$k_3 = -4.39 + 0.45\ln\left(\gamma_d\right) - 0.01\,pfc + 0.05a_S + 0.15\ln\left(\lambda_T\right) \tag{4.7}$$

**Table 4.4 Results of Multiple Regression Analysis**

| | Variables | DF | Parameter Estimate | Standard Error | t Ratio | p-value |
|---|---|---|---|---|---|---|
| **Prediction Model of** $\ln(k_1)$ | Intercept | 1 | -137.19 | 17.72 | -7.74 | <0.0001 |
| | $\ln(\gamma_d)$ | 1 | 13.60 | 1.77 | 7.70 | <0.0001 |
| | $\ln(\lambda_A)$ | 1 | 4.35 | 1.42 | 3.07 | 0.0078 |
| | $\lambda_S$ | 1 | -0.62 | 0.17 | -3.72 | 0.0021 |
| | $\ln(\lambda_T)$ | 1 | 1.68 | 0.32 | 5.31 | <0.0001 |
| **Prediction Model of** $k_2$ | Intercept | 1 | 36.14 | 5.60 | 6.46 | <0.0001 |
| | $pfc$ | 1 | 0.04 | 0.01 | 4.87 | 0.0002 |
| | $\ln(\lambda_A)$ | 1 | -3.81 | 0.74 | -5.17 | <0.0001 |
| | $a_S$ | 1 | -0.22 | 0.06 | -3.67 | 0.0023 |
| | $\ln(\lambda_T)$ | 1 | -0.77 | 0.11 | 6.78 | <0.0001 |
| **Prediction Model of** $k_3$ | Intercept | 1 | -4.39 | 0.71 | -6.16 | <0.0001 |
| | $\ln(\gamma_d)$ | 1 | 0.45 | 0.09 | 5.01 | 0.0002 |
| | $pfc$ | 1 | -0.01 | 0.001 | -8.09 | <0.0001 |
| | $a_S$ | 1 | 0.05 | 0.01 | 5.85 | <0.0001 |
| | $\ln(\lambda_T)$ | 1 | 0.14 | 0.02 | 9.22 | <0.0001 |

Figure 4.7 compares the k values predicted by Equations 4.5 to 4.7 with those predicted using simple empirical parameters, including dry unit weight, optimum water content, plasticity index, liquid limit and $P_{200}$. As can be seen from Figure 4.7, the R-squared values of the performance-related prediction models are much higher than those produced by simple empirical parameters. This is because the selected material properties in this study are directly related to the performance of unbound aggregates. This fact also suggests that the proposed performance-related base course properties can accurately predict the k coefficients of the resilient modulus model.

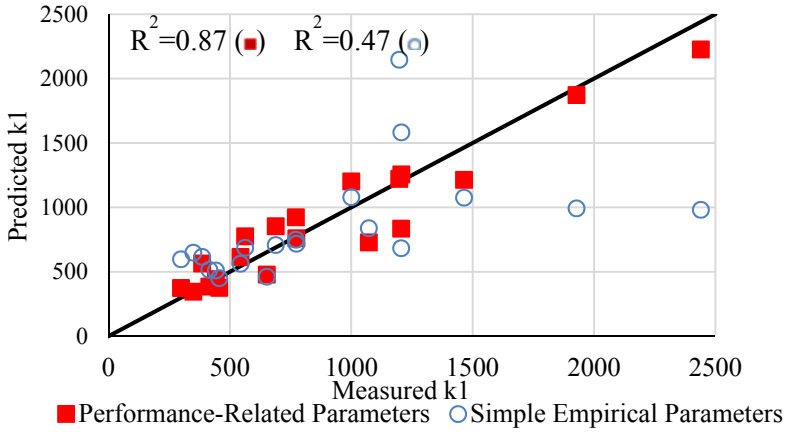


**(a)**

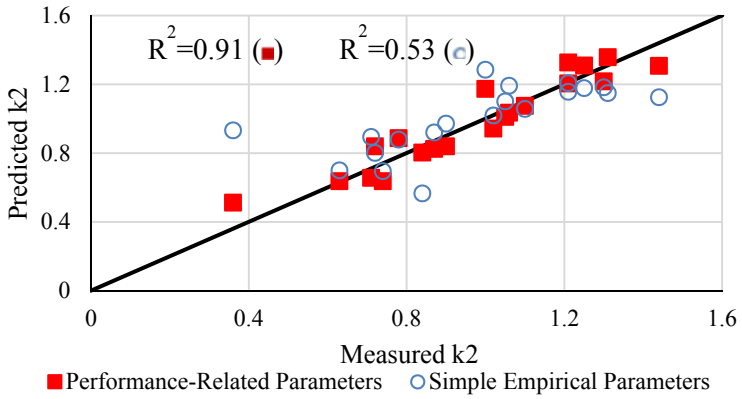


**(b)**

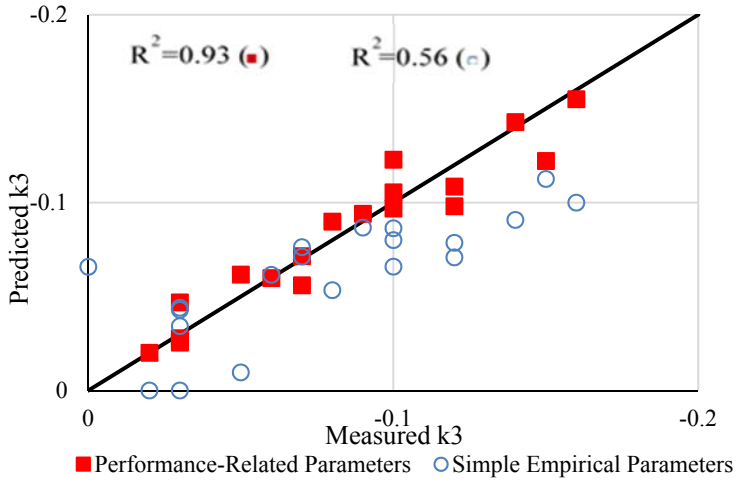


**(c)**

**Figure 4.7 Comparison between Predicted k Values by Performance-Related Parameters and Simple Empirical Parameters**

### *4.5.2 Prediction of Permanent Deformation for Base Materials*

In order to characterize the permanent deformation properties of unbound base materials, various models have been developed to determine the relation between the accumulated permanent strain and the number of load cycles. Two commonly used models are the VESYS model and the Tseng-Lytton model, which are shown in Equations 4.8 and 4.9, respectively (Kenis 1977; Tseng and Lytton 1989).

$$\frac{1}{\varepsilon_r}\left[\frac{\partial \varepsilon^P(N)}{\partial N}\right] = \mu N^{-\alpha} \tag{4.8}$$

where $\varepsilon_r$ is the resilient strain of the granular aggregate; $\varepsilon^p$ is the permanent strain of the granular aggregate; $N$ is the number of load cycles; $\mu$ and $\alpha$ are the permanent deformation properties in VESYS model.

$$\varepsilon^p = \varepsilon_0^p e^{-(\frac{\rho}{N})^\beta} \tag{4.9}$$

where $\varepsilon^p$ is the permanent strain of the granular material; $\varepsilon_0^p$ is the maximum permanent strain; $N$ is the number of load cycles; $\rho$ is the scale factor; and $\beta$ is the shape factor. $\varepsilon_0^p$, $\rho$ and $\beta$ are permanent deformation properties in the Tseng-Lytton model, which is implemented in the current pavement ME design program. In both the models, the permanent deformation properties are determined through the regression analysis of test data from repeated load triaxial tests. The load sequence of the repeated load triaxial test is shown in Table 4.5. The test begins with sequence zero as a preconditioning step. The following sequence is used to determine the unrecoverable behavior of the granular material. The static confining pressure and haversine-shaped

deviator stress with 0.1 second load period and 0.9 second rest period are applied to the specimen for 10,000 cycles. Table 4.6 lists the determined permanent deformation properties for base materials compacted at optimum moisture content.

**Table 4.5 Load Sequences for Permanent Deformation Test**

| Sequence | Confining Pressure (psi) | Contact Stress (psi) | Cyclic Stress (psi) | Maximum Stress (psi) | Number of Cycles |
|---|---|---|---|---|---|
| 0 | 15 | 1.5 | 13.5 | 15.0 | 500 |
| 1 | 7 | 2.0 | 18 | 20.0 | 10000 |

**Table 4.6 Summary of Permanent Deformation Test Results for Aggregate Specimens Compacted at Optimum Moisture Content**

| Source Type | $\varepsilon_r$ at 500th load repetition | VESYS Model Parameters | | Tseng-Lytton Model Parameters | | |
|---|---|---|---|---|---|---|
| | | $\alpha$ | $\mu$ | $\varepsilon_0^p$ | $\rho$ | $\beta$ |
| A01 | 0.000389 | 0.811 | 0.437 | 8.38E-03 | 890 | 0.301 |
| A02 | 0.000307 | 0.769 | 0.294 | 5.04E-03 | 860 | 0.305 |
| B01 | 0.000359 | 0.776 | 0.461 | 9.32E-03 | 940 | 0.287 |
| B02 | 0.000406 | 0.727 | 0.404 | 1.28E-02 | 1500 | 0.246 |
| C01 | 0.000881 | 0.79 | 0.227 | 1.04E-02 | 860 | 0.305 |
| D01 | 0.000385 | 0.675 | 0.363 | 1.23E-02 | 970 | 0.293 |
| D02 | 0.000325 | 0.794 | 0.284 | 4.86E-03 | 940 | 0.292 |
| E01 | 0.000312 | 0.823 | 0.137 | 1.98E-03 | 820 | 0.310 |
| F01 | 0.000423 | 0.767 | 0.909 | 2.19E-02 | 900 | 0.300 |
| F02 | 0.000482 | 0.684 | 0.526 | 2.24E-02 | 1230 | 0.304 |
| G01 | 0.000361 | 0.711 | 0.349 | 9.19E-03 | 950 | 0.302 |
| G02 | 0.000228 | 0.647 | 0.196 | 4.50E-03 | 980 | 0.310 |
| H01 | 0.000192 | 0.944 | 0.108 | 1.42E-03 | 980 | 0.100 |
| I01 | 0.000395 | 0.458 | 0.006 | 8.57E-04 | 1530 | 0.305 |

The similar stepwise regression analysis is performed to identify the significant performance-related properties of the base course for predicting $\alpha$, $\mu$, $\varepsilon_0$, $\rho$, and $\beta$ in the permanent deformation models (Nazzal and Mohammad 2010). The analysis mixes the forward and backward stepwise regression methods. Initially, all of the variables are inputted into the model. When running the analysis, the variables are removed or entered on the basis of the p-value threshold stopping rule. That is, if the p-value of the variable is larger than 0.25, the variable will be removed from the model, and vice versa. Finally, the one with largest F-test value is chosen as the best regression model.

Table 4.7 presents the results produced by the JMP software. It is shown that maximum dry density, MBV, shape parameter of gradation, scale parameter of angularity index, shape parameter of texture, and scale parameter of texture are significantly influential variables to predict the parameters in the VESYS model. It is also suggested that MBV, PFC, shape parameter of angularity index, shape parameter of texture, and scale parameter of texture are significantly influential variables to predict the parameters in the Tseng-Lytton Model. According to the regression analysis, Equations 4.10 to 4.14 list the prediction models for $\alpha$, $\mu$, $\varepsilon_0$, $\rho$, and $\beta$, respectively. The indicators of these permanent deformation properties are a mixture of those that can only be measured in the laboratory and others that can also be measured in the field. In the laboratory, the permanent deformation indicators that can be measured are the dry density, the gradation and the Weibull measures of shape, angularity and texture. In the field, the permanent deformation indicators that can be measured are the MBV, the

percent fines content and the water content. Figure 4.8 compares the predicted permanent deformation parameter values as predicted by Equations 4.10 through 4.14 to the measured values listed in Table 4.6. A good agreement is observed between the model-predicted permanent deformation properties and the laboratory measured ones. This indicates that the proposed regression models can accurately predict the permanent deformation behavior.

$$\ln \alpha = 4.91 + 1.23 \ln \gamma_d - 0.02 MBV + 0.59 a_G - 1.91 \ln \lambda_A + 0.17 a_T \tag{4.10}$$

$$\ln \mu = -54.68 + 16.89 \ln \gamma_d + 0.06\, pfc + 3.34 a_G - 7.60 \ln \lambda_A - 3.72 \ln \lambda_T \tag{4.11}$$

$$\ln \varepsilon_0 = 10.24 - 0.03 MBV + 0.10\, pfc + 0.88 a_A - 3.95 \ln \lambda_T \tag{4.12}$$

$$\ln \rho = 6.74 + 0.02 MBV + 0.04\, pfc - 0.85 a_G + 0.03 \lambda_G - 0.13 a_T \tag{4.13}$$

$$\ln \beta = 10.17 - 2.75 \ln \gamma_d - 0.05\, pfc - 2.00 a_G - 1.61 \ln \lambda_A - 0.34 a_T \tag{4.14}$$

**Table 4.7 Results of Multiple Regression Analysis**

| | Variables | DF | Parameter Estimate | Standard Error | t Ratio | p-value |
|---|---|---|---|---|---|---|
| **Prediction Model of** $\ln\alpha$ | Intercept | 1 | 4.9077 | 8.565 | 0.57 | 0.58 |
| | $\ln\gamma_d$ | 1 | 1.2260 | 0.732 | 1.68 | 0.13 |
| | *MBV* | 1 | -0.0180 | 0.006 | -3.23 | 0.01 |
| | $a_G$ | 1 | 0.5875 | 0.258 | 2.28 | 0.05 |
| | $\ln\lambda_A$ | 1 | -1.9066 | 0.629 | -3.03 | 0.02 |
| | $a_T$ | 1 | 0.1701 | 0.05 | 3.23 | 0.01 |
| **Prediction Model of** $\ln\mu$ | Intercept | 1 | -54.678 | 51.48 | -1.06 | 0.32 |
| | $\ln\gamma_d$ | 1 | 16.894 | 4.262 | 3.96 | 0.004 |
| | *pfc* | 1 | 0.0558 | 0.053 | 1.05 | 0.33 |
| | $a_G$ | 1 | 3.3356 | 1.724 | 1.93 | 0.09 |
| | $\ln\lambda_A$ | 1 | -7.598 | 5.808 | -1.31 | 0.23 |
| | $\ln\lambda_T$ | 1 | -3.2748 | 0.989 | -3.77 | 0.006 |
| **Prediction Model of** $\ln\varepsilon_0$ | Intercept | 1 | 10.238 | 3.728 | 2.75 | 0.02 |
| | *MBV* | 1 | -0.0263 | 0.025 | -1.07 | 0.31 |
| | *pfc* | 1 | 0.0995 | 0.052 | 1.92 | 0.09 |
| | $a_A$ | 1 | 0.8882 | 0.316 | 2.81 | 0.02 |
| | $\ln\lambda_T$ | 1 | -3.9520 | 0.615 | -6.42 | 0.0001 |
| **Prediction Model of** $\ln\rho$ | Intercept | 1 | 6.7414 | 0.43 | 15.67 | <0.0001 |
| | *MBV* | 1 | 0.0167 | 0.007 | 2.42 | 0.04 |
| | *pfc* | 1 | 0.0432 | 0.009 | 5.02 | 0.001 |
| | $a_G$ | 1 | -0.8545 | 0.346 | -2.47 | 0.04 |
| | $\lambda_G$ | 1 | 0.0328 | 0.026 | 1.24 | 0.25 |
| | $a_T$ | 1 | -0.126 | 0.064 | -1.96 | 0.09 |
| **Prediction Model of** $\ln\beta$ | Intercept | 1 | 10.174 | 16.21 | 0.63 | 0.55 |
| | $\ln\gamma_d$ | 1 | -2.7506 | 1.488 | -1.85 | 0.10 |
| | *pfc* | 1 | -0.0492 | 0.018 | -2.7 | 0.03 |
| | $a_G$ | 1 | -2.000 | 0.503 | -3.98 | 0.004 |
| | $\ln\lambda_A$ | 1 | 1.6072 | 1.522 | 1.06 | 0.32 |
| | $a_T$ | 1 | -0.3403 | 0.095 | -3.58 | 0.007 |

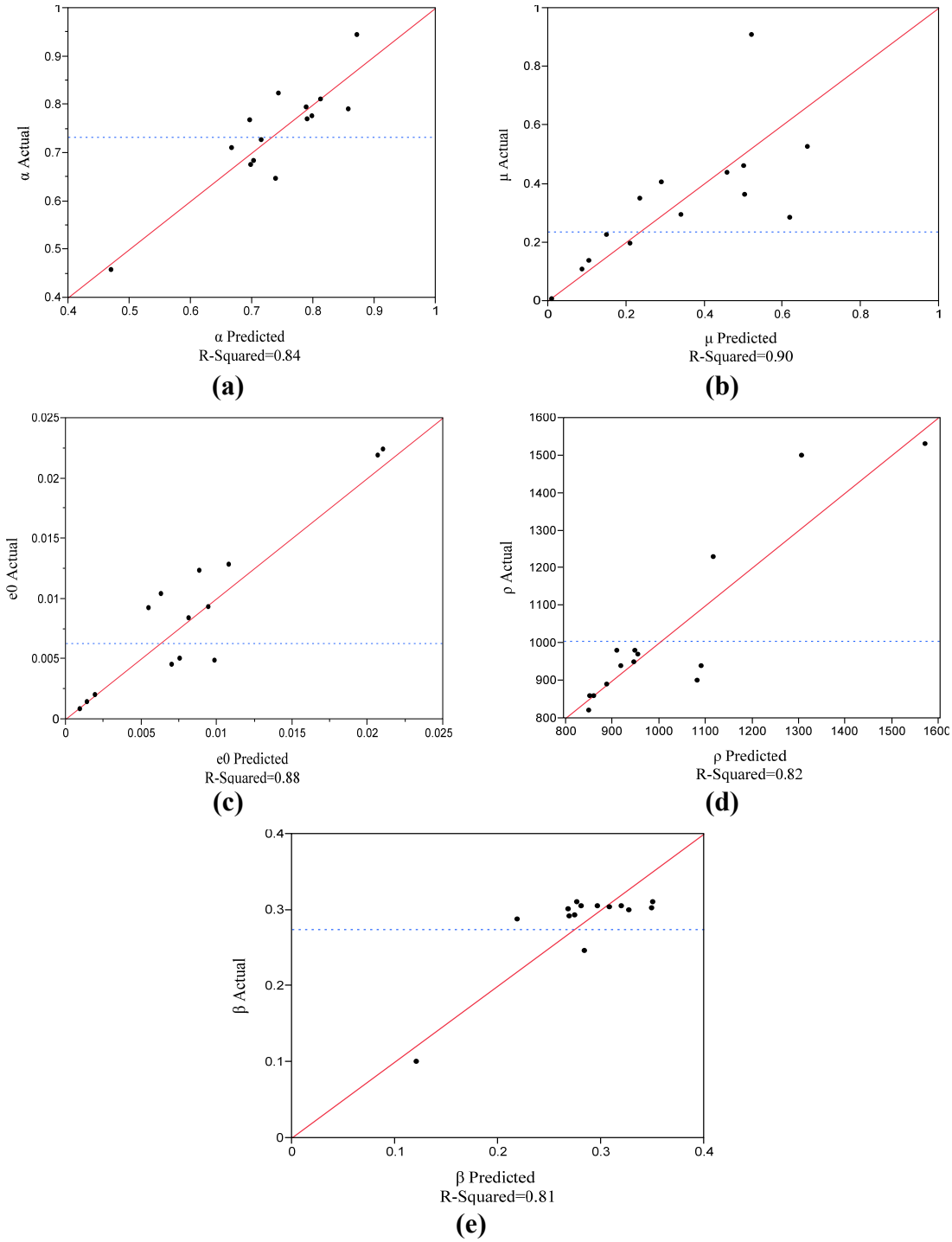


**Figure 4.8 Comparison of Predicted Permanent Deformation Properties and Measured Permanent Deformation Properties**

# 5. LABORATORY EVALUATION OF THE INFLUENCE OF GEOGRID ON PAVEMENT PERFORMANCE

## 5.1 Introduction

Geogrids are widely used by highway agencies in unbound base layers (i.e., within the base layer or as a base/subgrade interface layer) as a means for enhancing the performance of flexible pavements. Many studies which have performed tests on large-scale or in-service geogrid-reinforced pavement sections indicated that geogrids are effective in improving the stiffness and stability of the reinforced pavement structures and reducing the accumulated permanent deformation (Haas et al. 1988; Al-Qadi et al. 1994; Perkins 2002). To extend the use of geogrid in the flexible pavement structures, there is a need to incorporate the geogrid material into the pavement design. Currently, limited research has dealt with the methodologies of quantifying the influence of geogrid on pavement performance in a manner that would allow incorporation into the mechanistic-empirical (ME) pavement design and analysis procedures. The accurate and efficient laboratory characterization of geogrid-reinforced unbound granular material (UGM) is the first step for including the geogrid material in the pavement design (Abu-Farsakh et al. 2007). To develop a laboratory methodology compatible with the current Pavement ME Design, it is desired to quantify the characteristics of geogrid reinforcement in terms of the resilient properties and permanent deformation properties of the geogrid-reinforced UGMs (AASHTO 2008). These properties can be determined using repeated load triaxial (RLT) tests.

Many studies have been conducted to characterize the effect of geogrid reinforcement on the vertical resilient modulus of UGMs. It was found that the geogrid did not have a significant effect on enhancing the vertical resilient modulus of the reinforced UGMs when the specimen was fabricated as a 15-cm diameter and 30-cm height cylinder (Nazzal et al. 2007) or a 20-cm diameter and 40-cm height cylinder (Moghaddas-Nejad and Small 2003). On the contrary, Rahman et al. (2014) reported that the geogrid was effective in improving the resilient modulus of the reinforced UGMs when the specimen size was reduced to a dimension of 15-cm diameter and 20-cm height. Therefore, it is inferred that the effect of the geogrid reinforcement on the resilient modulus of the UGMs depends on the dimensions of the UGM specimen. Yang and Han (2013) developed an analytical model to predict the resilient modulus of the geogrid-reinforced UGMs at any given dimensions. According to this analytical model, the geogrid is more effective in increasing the resilient modulus of the UGMs with a larger diameter and a smaller height. McDowell et al. (2006) and Schuettpelz et al. (2009) showed that the geogrid provided the reinforcing effect in an area that is typically approximately 3 cm to 7.5 cm in thickness on both sides of the geogrid. Since the geogrid reinforcement influence zone only has such a small range, quantifying the influence of geogrid on the vertical resilient modulus of the UGMs with a 30-cm height or more may be inappropriate. Recent studies have revealed that the UGMs exhibit cross-anisotropic resilient behavior (Adu-Osei et al. 2001; Ashtiani 2009), i.e. the resilient moduli in the vertical plane are different from the horizontal resilient moduli, while the resilient moduli in the horizontal plane are the same in all directions. The

cross-anisotropic nature of the UGMs has been demonstrated to be a major factor that influences pavement performance (Tutumluer and Thompson 1997; Oh et al. 2006). Therefore, quantifying the influence of geogrids on the resilient properties of UGMs should focus on evaluating the effect of geogrids on the cross-anisotropic properties of the base course, which however has not been identified in any of the literature that was reviewed in this study.

Compared to the increase of the resilient modulus, the reduction of the permanent deformation of UGM is a more important benefit of the geogrid reinforcement. Perkins et al. (2004) and Nazzal et al. (2007) found that the geogrid considerably reduced the permanent deformation of the UGMs using the RLT tests. Moghaddas-Nejad and Small (2003) and Abu-Farsakh et al. (2012) showed that for a particular confining stress, the reduction of the permanent deformation by geogrid increased rapidly with the increase of the deviatoric stress, until a peak was reached, then decreased gradually. This finding indicated that the stress level significantly influenced the effects of the geogrid on the reduction of the permanent deformation of the UGMs. It is known that the stress induced by the traffic load is non-uniformly distributed in the base course of flexible pavements. Therefore, quantifying the effect of stress level on the permanent deformation characteristics of the geogrid-reinforced UGMs is critical to accurately predict the rutting of the geogrid-reinforced unbound base layer. In addition, previous laboratory studies mainly evaluated the influential factors, such as the aperture type of geogrid, the mechanical properties of geogrid, and the geogrid location, on the permanent deformation characteristics of the reinforced UGM with dimensions of 15-cm diameter

and 30-cm height (Abu-Farsakh et al. 2012; Wayne et al. 2011). The influence of these factors on the permanent deformation characteristics of the smaller height specimen (i.e., 15-cm diameter and 15-cm height) is still not clear.

To address the aforementioned problems, this chapter describes a laboratory methodology to quantify the impact of the geogrid on the resilient and permanent deformation properties of UGMs. Specifically, the effect of the geogrid on the cross-anisotropic resilient modulus is evaluated using the rapid triaxial test. The stress dependent permanent deformation properties of the geogrid-reinforced UGMs are characterized by the previously proposed mechanistic-empirical rutting model. The UGM specimen size is reduced to the dimension of 15-cm diameter and 15-cm height for both the cross-anisotropy test and permanent deformation test.

## 5.2 Materials and Experimental

### *5.2.1 Materials*

*Aggregate*

One crushed granite material was used in this study. The gradation of the selected aggregate material is shown in Table 1a. It has a maximum dry density of $2.16\times10^3$ kg/m$^3$, and an optimum water content of 6.7%. The compacted aggregate specimen has a cohesion of 20.2 kPa, and an internal friction angle of 51.3°.

*Geogrid*

Three types of geogrid, TX-1, TX-2 and BX-3, were selected to reinforce the UGMs. “TX” denotes the aperture shape of the geogrid is triangular. “BX” represents

the aperture shape of the geogrid is rectangular. The physical and mechanical properties of the selected geogrids are shown in Table 1b. It is seen that the geogrid TX-2 has a higher sheet stiffness than the geogrid TX-1.

**Table 5.1 Information of Selected Materials**

**a. Gradation of Crushed Granite Aggregate**

| **Sieve Size (mm)** | 25.4 | 19.0 | 12.7 | 9.5 | 4.75 | 2.36 | 1.18 | 0.6 | 0.075 |
|---|---|---|---|---|---|---|---|---|---|
| **Passing Percentage (%)** | 100 | 97 | 86 | 68 | 46 | 30 | 20 | 15 | 4.1 |

**b. Physical and Mechanical Properties of the Selected Geogrids**

| **Geogrid Type** | **Aperture Shape** | **Aperture Dimension (mm)** | **Tensile Sheet Stiffness[a] (kN/m)** | |
|---|---|---|---|---|
| | | | **MD[b]** | **XMD[c]** |
| TX-1 | Triangle | 40×40×40 | 225 | 225 |
| TX-2 | Triangle | 40×40×40 | 300 | 300 |
| BX-3 | Rectangle | 25×33 | 300 | 450 |

a. Sheet stiffness corresponding to 2% tensile strain
b. MD=Machine direction
c. XMD=Cross-Machine direction

*Geogrid-Reinforced and Unreinforced Aggregate Specimen*

The geogrid-reinforced and unreinforced aggregate specimens were fabricated as 15-cm diameter and 15-cm height cylinders at the optimum water content using a modified compactive effort (*21*). The effect of the geogrid depends upon its location within the base course. To evaluate this effect, the geogrid was placed in three locations,

namely, the middle of the specimen, one-quarter below the middle of the specimen, and the bottom of the specimen, respectively, as shown in Figure 5.1.

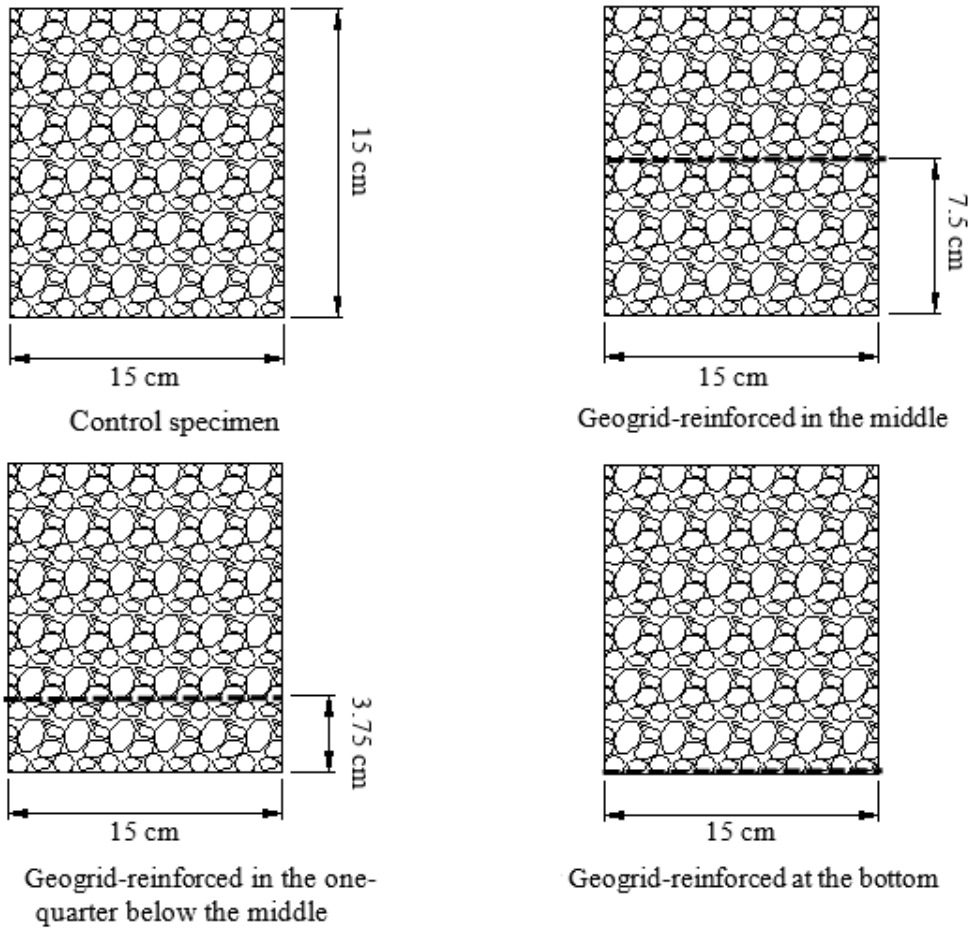


**Figure 5.1 Geogrid Locations in UGM Specimen**

### *5.2.2 Test Methods*

*Cross-Anisotropy Test*

The cross-anisotropy tests were conducted on both the geogrid-reinforced and unreinforced aggregate specimens using the Universal Testing Machine (UTM) with a Rapid Triaxial Test (RaTT) cell. Figure 3.2 shows the configuration of the cross-anisotropy test. Prior to testing, the RaTT cell was moved downward to encompass the specimen. The confining pressure was applied directly to the specimen by the RaTT cell via a pneumatic bladder. The dynamic axial load was applied to the specimen through the loading frame of the UTM. In pre-conditioning, the confining pressure was controlled at 103.4 kPa, and a 103.4 kPa deviatoric axial load was applied for 500 repetitions. Table 5.2 shows the cross-anisotropy test protocol developed by Texas A&M University (Adu-Osei et al. 2001). There were a total of 10 stress states associated with corresponding dynamic stresses in the three stress modes (compression, shear and extension mode). At each stress state, every loading cycle of the dynamic stress consisted of 1.5 seconds of loading and 1.5 seconds of unloading. Linear Variable Differential Transformers (LVDTs) measured the vertical and horizontal deformations of the specimen. The test data were used to calculate the anisotropic properties of geogrid-reinforced and unreinforced aggregate specimen using the system identification method.

*Permanent Deformation Test*

Compared to the cross-anisotropy test, the permanent deformation test used the same UTM configuration, but a different test module. The detailed permanent deformation test procedure was described in Chapter 3.

**Table 5.2 RLT Test Protocols for Determining Cross-Anisotropic Properties**

| Stress state | Static Stress (kPa) | | Dynamic Stress (kPa) | | | | | |
|---|---|---|---|---|---|---|---|---|
| | | | Compression | | Shear | | Extension | |
| | $\sigma_y$ | $\sigma_x$ | $\sigma_y^c$ | $\sigma_x^c$ | $\sigma_y^s$ | $\sigma_x^s$ | $\sigma_y^e$ | $\sigma_x^e$ |
| 1 | 40 | 25 | 5 | 0 | 10 | -5 | -5 | 5 |
| 2 | 50 | 25 | 10 | 0 | 10 | -5 | -10 | 5 |
| 3 | 70 | 40 | 10 | 0 | 10 | -5 | -10 | 10 |
| 4 | 130 | 60 | 20 | 0 | 20 | -10 | -10 | 10 |
| 5 | 150 | 70 | 20 | 0 | 20 | -10 | -10 | 10 |
| 6 | 170 | 100 | 20 | 0 | 20 | -10 | -20 | 20 |
| 7 | 220 | 120 | 30 | 0 | 30 | -15 | -20 | 20 |
| 8 | 250 | 140 | 30 | 0 | 30 | -15 | -20 | 20 |
| 9 | 250 | 120 | 30 | 0 | 30 | -15 | -20 | 20 |
| 10 | 250 | 105 | 30 | 0 | 30 | -15 | -20 | 20 |

## 5.3 Impact of Geogrid on Cross-Anisotropy of UGM

The measured vertical and horizontal resilient deformations in the cross-anisotropy test are analyzed using the system identification method to back-calculate the vertical and horizontal resilient moduli, $E_y$ and $E_x$, respectively, based on the constitutive model presented in Equation 1. The determined vertical and horizontal moduli of the geogrid-reinforced specimens are compared to those of the unreinforced specimens (the control) by calculating the normalized modulus ratio of the geogrid-reinforced specimen to the unreinforced specimen, as shown in Equations 5.1 and 5.2.

$$Normalized\,Horizontal\,Modulus\,Ratio = \frac{E_{x-geogrid}}{E_{x-control}} \tag{5.1}$$

$$Normalized\ Vertical\ Modulus\ Ratio = \frac{E_{y-geogrid}}{E_{y-control}} \quad (5.2)$$

where $E_{x-geogrid}$ is the horizontal resilient modulus of the geogrid-reinforced specimen; $E_{x-control}$ is the horizontal resilient modulus of the unreinforced specimen; $E_{y-geogrid}$ is the vertical resilient modulus of the geogrid-reinforced specimen; and $E_{y-control}$ is the vertical resilient modulus of the unreinforced specimen.

Figure 5.2a shows the horizontal and vertical moduli of the unreinforced UGM at each stress state. The test stress states shown in Table 5.2 are classified as the low stress level (i.e., stress states 1-3), the medium stress level (i.e., stress states 4-6), and the high stress level (i.e., stress states 7-10). Figures 5.2b and 5.2c show the effect of the three types of geogrid (TX-1, TX-2 and BX-3) on the horizontal and vertical resilient moduli of UGM when they are placed in the middle of the specimen. It is seen that the normalized horizontal and vertical modulus ratios of all three types of geogrid-reinforced specimens are larger than 100% at every stress state, which indicates that the geogrid increases both the vertical and horizontal moduli of the UGM specimen since the total elastic deformation of the specimen is restricted due to adding of the geogrid in the UGMs. Compared to the geogrid TX-1, the geogrid TX-2 provides slightly higher horizontal and vertical modulus ratios at most of stress states, which demonstrates that the geogrid with a higher sheet stiffness is more beneficial for the reinforcement. Compared to the geogrid TX-1 and TX-2, the geogrid BX-3 provides comparable reinforcement on the horizontal and vertical resilient moduli of UGM. This indicates that the aperture shape of the geogrid does not significantly affect the resilient modulus of

UGM specimen. As can be seen from Figures 5.2b and 5.2c, the geogrid is more effective in reinforcing the horizontal and vertical moduli of UGM when it is subjected to the low or medium stress levels. This makes sense as the resilient modulus of UGMs is stress dependent and, at high stress level, the modulus is dominated by stress values rather than the geogrid. Thus the effect of geogrid on resilient modulus is more significant at relatively low stress levels. Figure 5.2d presents the effect of the geogrid type on the anisotropic ratio of UGM, which is defined as the ratio of the horizontal modulus to the vertical modulus. It is observed that normalized anisotropic ratios of the geogrid-reinforced specimens fluctuate around 100%. This indicates that the inclusion of geogrid does not influence the anisotropic ratio of UGM. In sum, geogrid increases both vertical and horizontal resilient moduli but not the modulus ratio (i.e., anisotropy) of UGM, which is more significant at low and medium stress levels and enhanced slightly by greater geogrid sheet stiffness but not affected by the geogrid aperture shape.

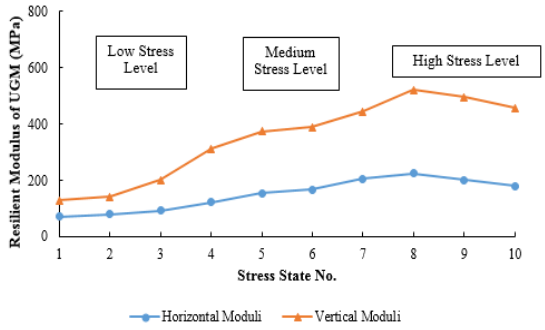


**a. Horizontal and Vertical Moduli of Unreinforced UGM**

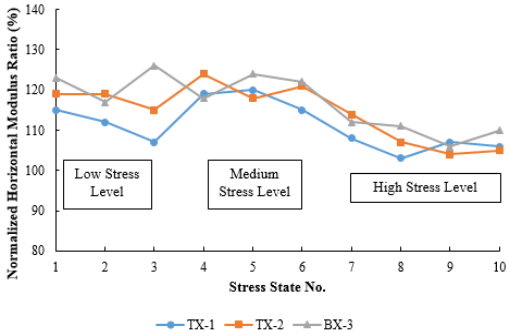


**b. Effect of Geogrid Type on Horizontal Modulus of Granular Material**

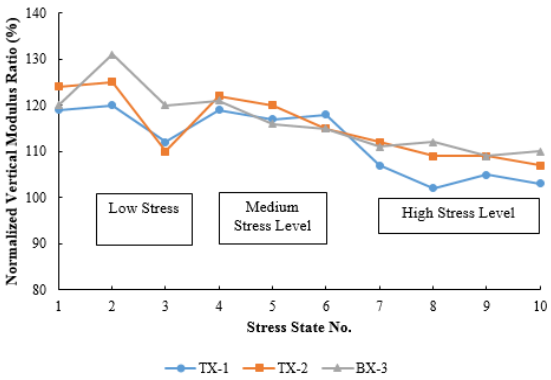


**c. Effect of Geogrid Type on Vertical Modulus of Granular Material**

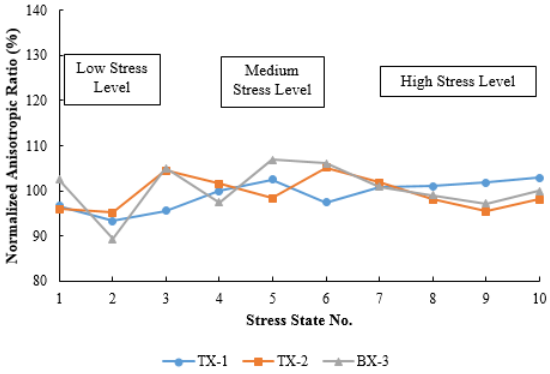


**d. Effect of Geogrid Type on Anisotropic Ratio of Granular Material**

**Figure 5.2 Effect of Geogrid Type on Cross-Anisotropic Properties of Granular Material**

Figures 5.3a and 5.3b present the effect of geogrid location on the horizontal and vertical resilient moduli of UGM. It is seen that the normalized modulus ratios when geogrid placed in the middle or at one-quarter below the middle of specimen are larger than 100% at every stress state, while those of the specimen with geogrid placed at the

bottom of a specimen fluctuate around 100%. This indicates that placing the geogrid in the middle or at one-quarter below the middle of a specimen increases the vertical and horizontal moduli, but placing the geogrid at the bottom cannot reinforce the UGM neither vertically nor horizontally. Compared to the geogrid placed in the middle of specimen, the geogrid placed at one-quarter below the middle of specimen provides slightly smaller normalized vertical and horizontal modulus ratios at most of the stress states, which indicates that the geogrid placed in the middle of specimen has a slightly better reinforcement effect. It must be noted that the bottom of the UGM specimen interfaces with an aluminum platen, which differs from the interface between a pavement base layer with the subgrade. Thus placing a geogrid at the bottom of the UGM specimen and at the bottom of the base layer may introduce different effects on the UGM performance, which needs to be studied based on pavement structural analysis in the future.

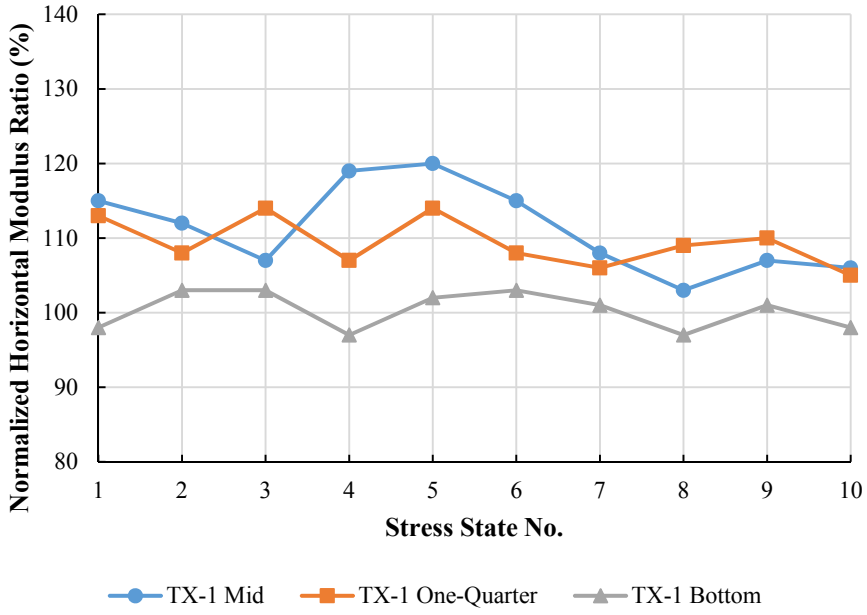


**a. Effect of Geogrid Location on Horizontal Modulus of Granular Material**

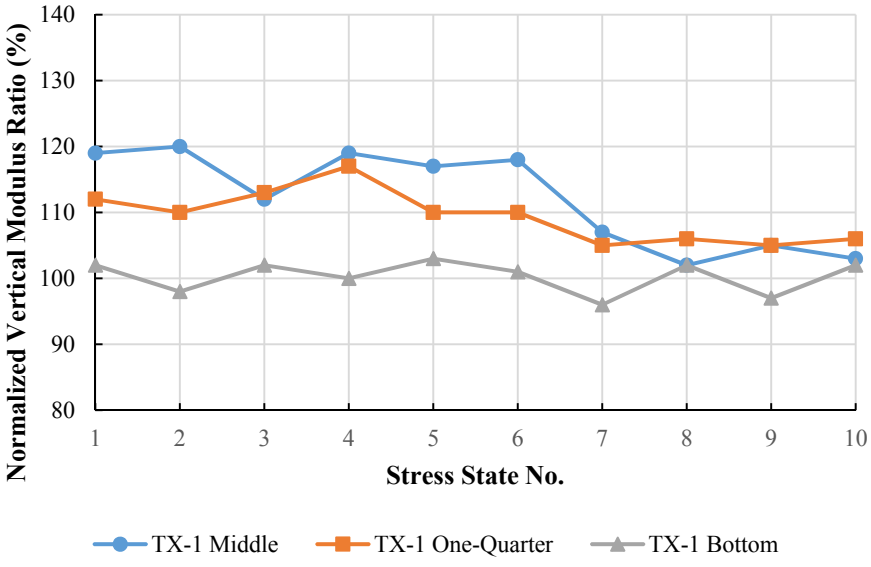


**b. Effect of Geogrid Location on Vertical Modulus of Granular Material**

**Figure 5.3 Effect of Geogrid Location on Cross-Anisotropic Properties of Granular Material**

## 5.4 Impact of Geogrid on Permanent Deformation of UGM

According to Table 3.1, the stress states of the permanent deformation test are classified as two groups: one group has the same $I_1$ with various $J_2$ (i.e., stress state 1, 2, 3, 4 and 8); the other one has the same $J_2$ with different $I_1$ (i.e., stress state 1, 5, 6, 7 and 9). Figures 5.4a and 5.5a present the correlations of $J_2$ and $I_1$ with the accumulated permanent strain at 10,000 load cycles for geogrid-reinforced and unreinforced UGMs. At the same $I_1$, increasing $J_2$ results in an increasing accumulated plastic strain. While at a constant $J_2$, increasing $I_1$ yields a reduction of the accumulated permanent strain. This is consistent with the concept of the proposed permanent deformation model that $J_2$ is a softening indicator and $I_1$ is a strengthening factor for the permanent deformation of UGM. As can be seen in Figures 5.4a and 5.5a, these correlations are fitted by the power functions with 0.98-0.99 R-Squared values. The high goodness of fit explains why the power models of $I_1$ and $J_2$ are used in Equation 2.

It is observed from Figures 5.4a and 5.5a that the geogrid-reinforced UGMs have smaller plastic strains than those of unreinforced UGMs at every stress state. The reduction of plastic strain (RPS) due to the geogrid reinforcement is quantified using Equation 5.3 (Abu-Farsakh et al. 2012).

$$RPS\,(\%) = \frac{permanent\ strain\ without\ geogrid - permanent\ strain\ with\ geogrid}{permanent\ strain\ without\ georid} \times 100 \qquad (5.3)$$

Figures 5.4b and 5.5b show the effect of geogrid type on the permanent deformation of UGM in terms of the RPS. Compared to the geogrid BX-3, the inclusions of geogrid TX-1 and TX-2 have higher RPS values at all of the stress states. This

demonstrates that the geogrid with the triangular apertures is more effective than that with the rectangular apertures in reducing the permanent deformation of UGM. This could be due to the fact that the triangle is a more stable shape than the rectangle in terms of deformation. However, it is recalled that the aperture shape of geogrid does not significantly affect the resilient modulus of UGM specimen. Thus the stable effect of the triangle apertures become obvious only when the deformation of the geogrid reaches a significant level (e.g., the plastic deformation). In addition, it is seen that the geogrid TX-2 has a higher RPS value than the geogrid TX-1, which indicates that the geogrid with a higher sheet stiffness has more benefits for reinforcing the UGM. Figures 5.4b and 5.5b also illustrate the effect of stress levels on the geogrid reinforcement. It is seen from Figure 5.4b that the RPS of geogrid-reinforced UGM is only 10-20% when the square root of $J_2$ equals 39.8 kPa, while it increases to 20-40% when the square root of $J_2$ reaches 99.4 kPa or more. This indicates that the effect of geogrid reinforcement is not significant in reducing the permanent deformation until the deviatoric shear stress reaches a threshold level (e.g., 99.4 kPa in this study). Figure 5.5b shows that the RPS of different types of geogrid-reinforced UGMs do not vary with the bulk stress when the square root of $J_2$ equals to 111.4 kPa. This indicates that the bulk stress level does not significantly affect the geogrid reinforcement when the deviatoric shear stress is high.

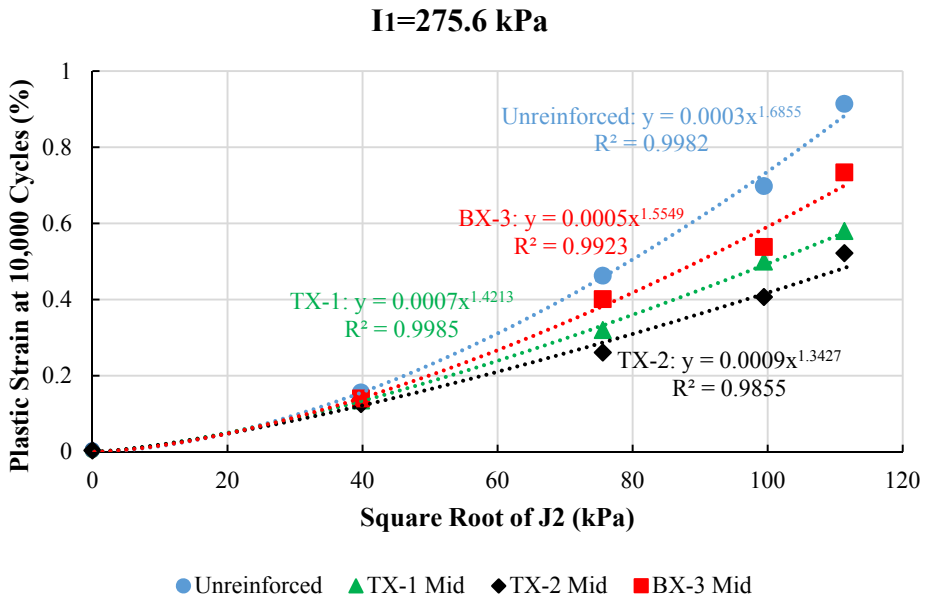


**a. Correlations of $J_2$ with Accumulated Plastic Strain for Geogrid-Reinforced and Unreinforced UGM**

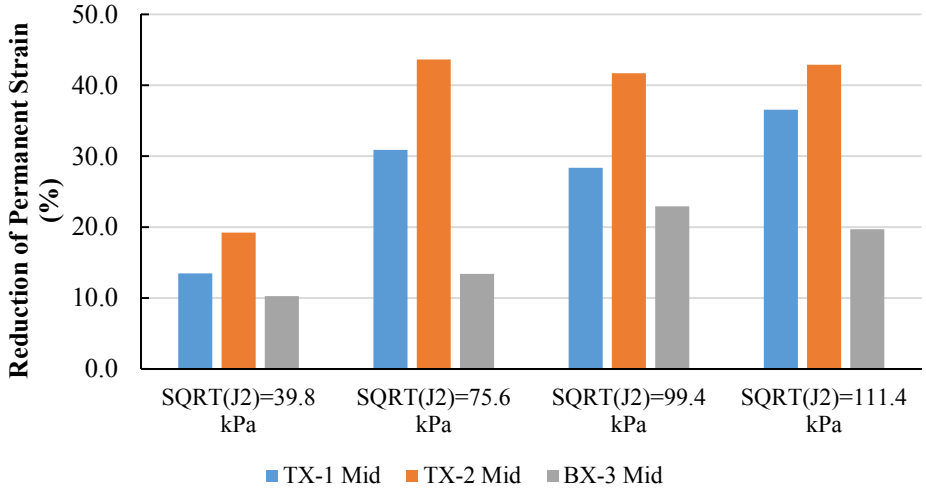


**b. Effect of Geogrid Type on Permanent Deformation of UGM at Different Deviatoric Stress Levels**

**Figure 5.4 Effect of Deviatoric Stress Level on Geogrid Reinforcement**

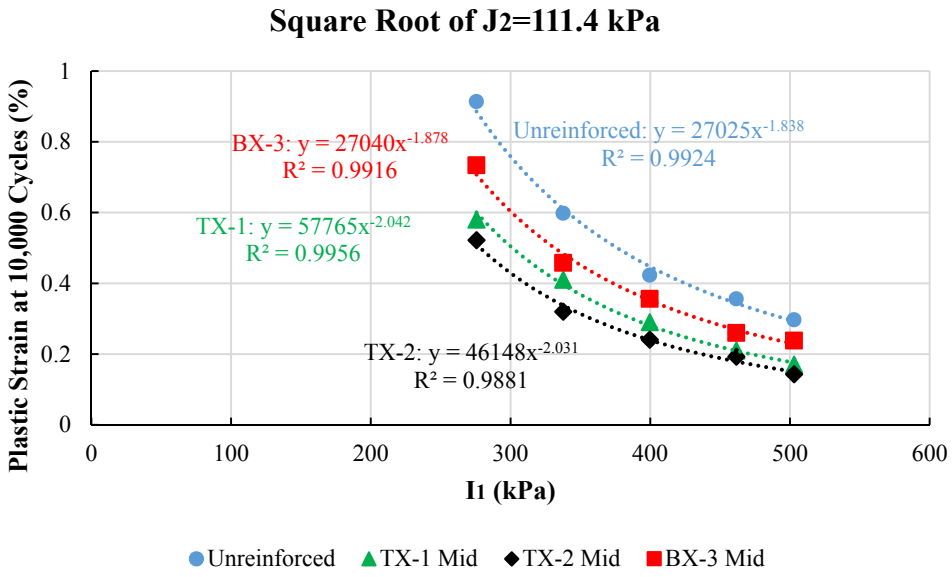


**a. Correlations of $I_1$ with Accumulated Plastic Strain for Geogrid-Reinforced and Unreinforced UGM**

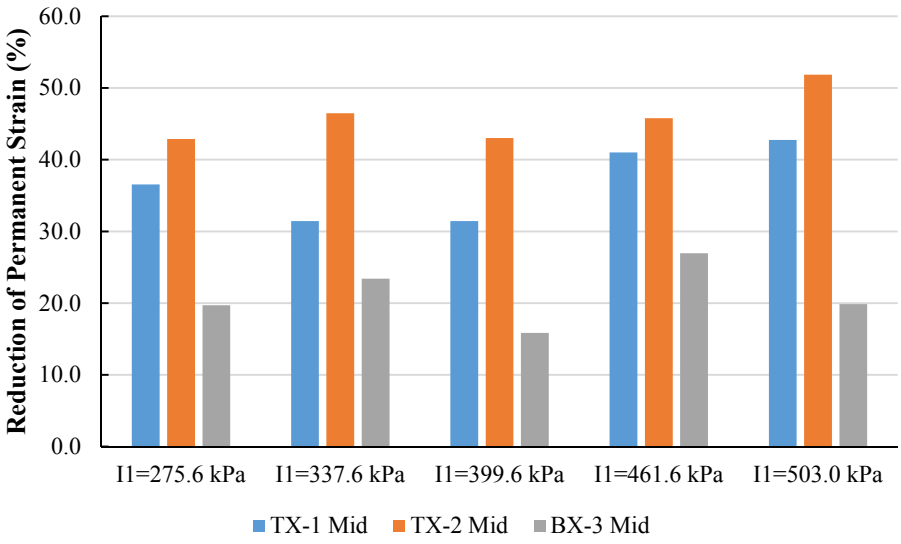


**b. Effect of Geogrid Type on Permanent Deformation of UGM at Different Bulk Stress Levels**

**Figure 5.5 Effect of Bulk Stress Level on Geogrid Reinforcement**

Figures 5.6a and 5.6b show the effect of geogrid location on the permanent deformation of UGM. It is seen that the geogrid placed in the middle or at one-quarter below the middle of UGM significantly reduces the accumulated plastic strain when the square root of $J_2$ is 75.6 kPa or more, whereas the geogrid placed at the bottom of the UGM does not exhibit any beneficial effect. Again, the differences between a laboratory UGM bottom interface and a field pavement based bottom interface should be considered. Compared to the geogrid placed at one-quarter below middle of the specimen, the geogrid placed in the middle of the specimen has larger RPS values, which demonstrates that placing the geogrid in the middle is more effective than placing it at one-quarter below the middle of UGM in reducing the permanent deformation. The reason lies in that the geogrid located in the middle has a greater influencing area within the sample compared to that located at one-quarter below the middle of the specimen. Thus the beneficial effects on permanent deformation reduction is greater when placing the geogrid in the middle. The same explanation can be applied to the increase of the resilient modulus as observed in Figure 5.3.

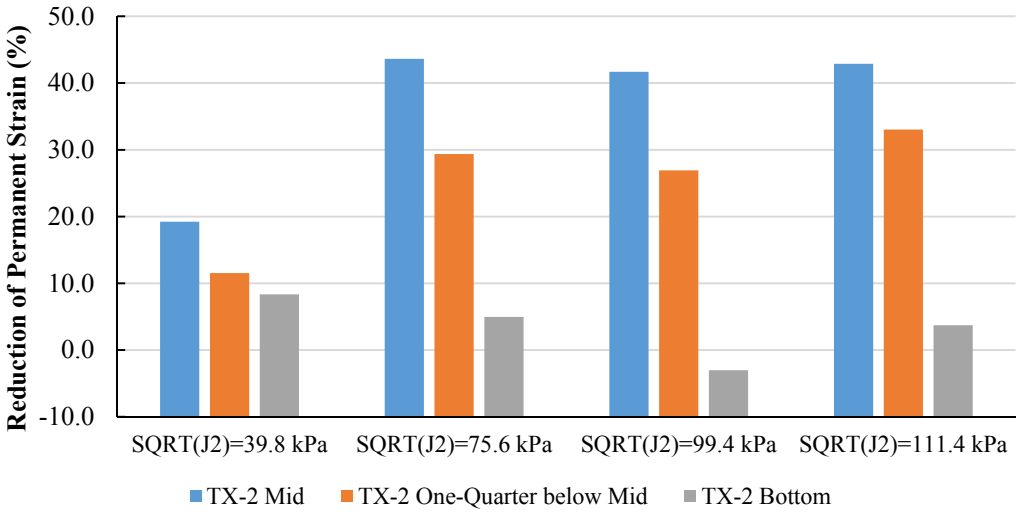


**a. Effect of Geogrid Location on Permanent Deformation of UGM at Different Deviatoric Stress Levels**

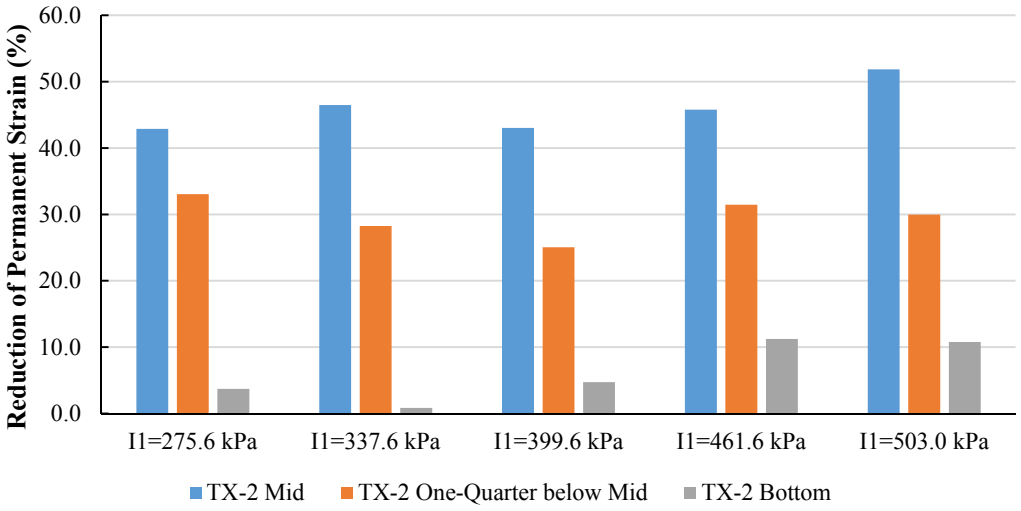


**b. Effect of Geogrid Location on Permanent Deformation of UGM at Different Bulk Stress Levels**

**Figure 5.6 Effect of Geogrid Location on Permanent Deformation Characteristics of UGM**

The proposed mechanistic-empirical rutting model is employed to quantify the permanent deformation characteristics of geogrid-reinforced and unreinforced UGMs at various stress states. The model coefficients are determined by using the solver function in Microsoft Excel to fit the measured permanent strain curves from stress states 1-7. Figures 5.7 compares the model-predicted permanent strain curves with the laboratory-measured ones at different stress states for geogrid-reinforced UGMs. It is seen that all of the determined RMSE values are relatively small, which indicates that the proposed model accurately captures the influence of stress level on the permanent deformation of the geogrid-reinforced UGMs.

Figures 5.7 also presents the determined coefficients of the proposed rutting model, which are used to predict the plastic strain curves of the UGMs at stress states 8 and 9. To examine the accuracy of the proposed rutting model, the model predicted permanent strain curves are compared to the laboratory-measured permanent strain curves from stress states 8 and 9, which are shown in Figure 5.8. It is seen that the model predictions have small RMSE values for both geogrid-reinforced and unreinforced UGMs at the two stress states, which indicates that the proposed rutting model is accurate to predict the stress dependent permanent deformation characteristics of geogrid-reinforced and unreinforced UGMs. Table 5.3 lists the determined model coefficients for the geogrid-reinforced and unreinforced UGMs tested in this study. The determined model coefficients can be used to predict the permanent deformation of UGMs at any stress levels and numbers of load repetitions.

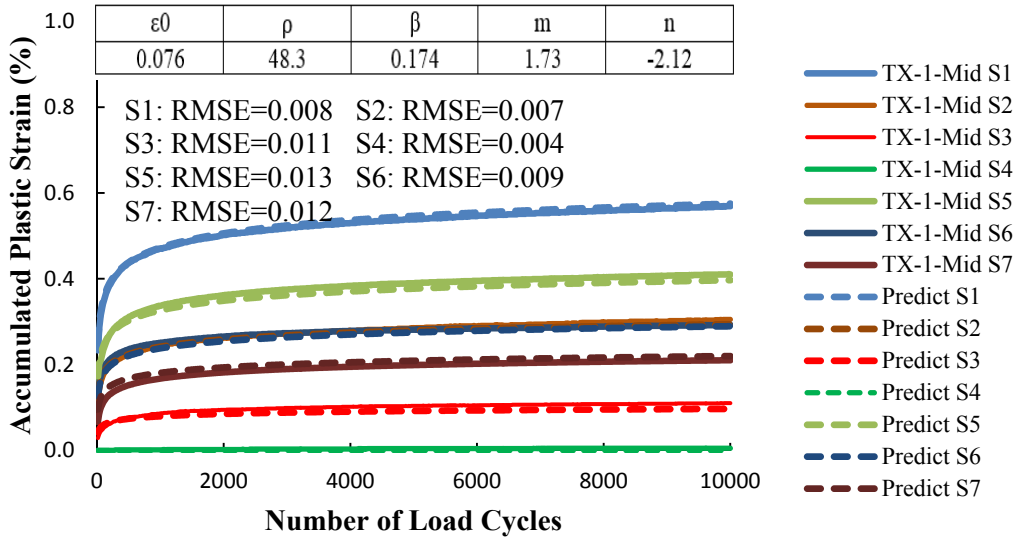


**Figure 5.7 Comparison of Lab-Measured and Proposed Model-Predicted Permanent Deformation Curves for Geogrid-Reinforced UGM**

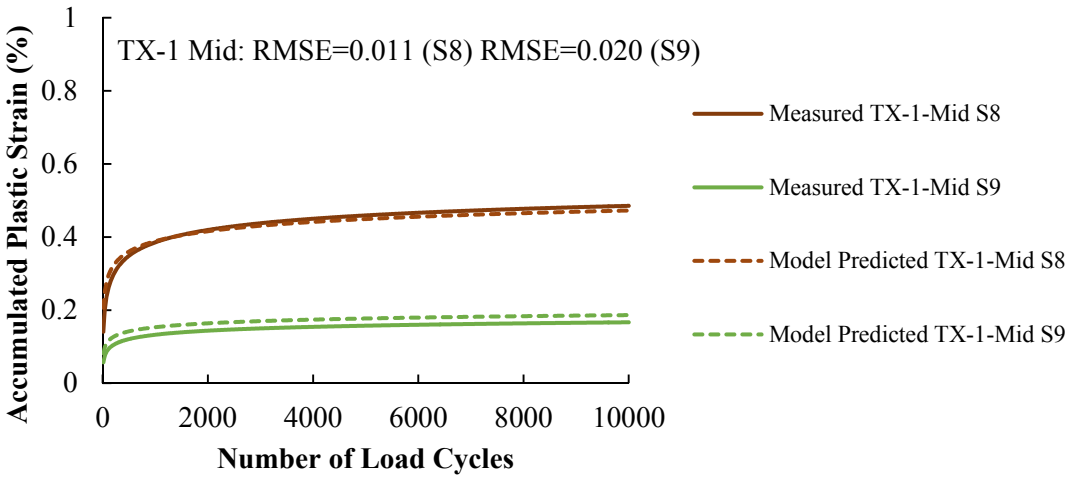


**Figure 5.8 Validation of Prediction Accuracy of Proposed Model for Geogrid-Reinforced and Unreinforced UGMs**

**Table 5.3 Determination of Model Coefficients for Geogrid-Reinforced and Unreinforced UGMs**

| Material Type | Permanent Deformation Model Coefficients | | | | |
|---|---|---|---|---|---|
| | $\varepsilon_0$ | $\rho$ | $\beta$ | m | n |
| Unreinforced | 0.149 | 72.4 | 0.247 | 1.70 | -2.16 |
| TX-1 Middle | 0.076 | 48.3 | 0.174 | 1.73 | -2.12 |
| TX-2 Middle | 0.068 | 82.1 | 0.165 | 1.84 | -2.21 |
| BX-3 Middle | 0.082 | 31.2 | 0.182 | 1.64 | -2.01 |
| TX-2 One-Quarter below Middle | 0.093 | 62.5 | 0.159 | 1.62 | -2.03 |
| TX-2 Bottom | 0.142 | 35.1 | 0.294 | 1.79 | -2.26 |

## 5.5 Analytical Model for Quantifying Impact of Geogrids

The repeated load triaxial test studies indicate that the placement of geogrid influences the cross-anisotropic properties (i.e. the vertical and horizontal modulus) and the permanent deformation properties of the UGM. An analytical model is proposed to predict the vertical and horizontal modulus and the permanent deformation of the geogrid-reinforced UGM when it is subjected to a triaxial load. Figure 5.9a shows a schematic plot of a geogrid-reinforced UGM specimen in the triaxial load test. The geogrid-reinforced specimen is compressed in the axial direction, and normally expands in the lateral direction due to the plastic and resilient deformation. It is seen that the lateral movement of UGM is restraint by the geogrid. The shear stress is generated due

to the relative lateral displacement between geogrid and aggregate, which results in the stretch of the embedded geogrid. Note that the lateral movement of aggregate and geogrid cannot be identical. Figure 5.9b shows the difference of lateral movement between geogrid and aggregate during the test. A coefficient $\alpha$ is employed to account for the difference of radial displacement between geogrid and aggregate, as shown in Equation 5.4.

$$\alpha = \frac{\varepsilon_{rr}^{a}}{\varepsilon_{rr}^{g}} \tag{5.4}$$

where $\varepsilon_{rr}^{a}$ is the aggregate radial tensile strain at the interface between geogrid and aggregate, $\varepsilon_{rr}^{g}$ is the geogrid radial tensile strain. Note that the value of $\alpha$ is normally larger than 1, which represents that the aggregate has a larger lateral movement than the geogrid. The analytical solution to determine the coefficient $\alpha$ is shown in Equations 5.5 and 5.6 (1).

$$\beta \cdot J_0\left(\beta\frac{D}{2}\right) - \frac{2}{D}\cdot J_1\left(\beta\frac{D}{2}\right) = \sigma_3 \tag{5.5}$$

$$\beta = \left[\frac{2G_a(\alpha-1)\left(1-\nu_g^2\right)}{\delta M}\right]^{1/2} \tag{5.6}$$

where $J_i(x)$ is the Bessel function of order i, $D$ is the diameter of the aggregate specimen (i.e. $D$=15 cm), $G_a$ is the shear modulus of the aggregate. Equation 5.5 is an implicit equation for the coefficient $\alpha$. The stretch of the geogrid generates a reinforcement force $T$ to confine the UGM specimen through the aggregate particle interlock and interface friction (Yang and Han 2013). Figure 5.9c shows that the

reinforcement force $T$ is equivalent to a triangularly distributed additional confining stress $\Delta\sigma_3$, which only acts on a 15 cm geogrid-reinforced influence zone (Schuettpelz et al. 2009). This distribution takes into account the phenomenon that the geogrid reinforcement influence decreases with the distance between aggregate and geogrid, and the geogrid reinforcement is negligible when the material is far away from the geogrid.

Under an axisymmetric plane-stress condition, the reaction force $T$ is determined by Equation 5.7.

$$T = \frac{M}{\left(1-\nu_g^2\right)} \cdot \left(\varepsilon_{rr}^g + \nu_g \varepsilon_{\theta\theta}^g\right) \tag{5.7}$$

where $M$ is the geogrid sheet stiffness, $\nu_g$ is the Poisson's ratio of the geogrid, $\varepsilon_{rr}^g$ is the geogrid tensile strain in the radial direction, and $\varepsilon_{\theta\theta}^g$ is the geogrid tensile strain in the circumferential direction. By assuming the geogrid expands uniformly in both the radial and the circumferential directions, Equation 5.7 is simplified as,

$$T = \frac{M}{\left(1-\nu_g\right)} \cdot \varepsilon_{rr}^g \tag{5.8}$$

If the equivalent additional confining stress $\Delta\sigma_3$ is triangularly distributed in the influential zone, the maximum additional confining stress $\Delta\sigma_{3\max}$ can be calculated by Equation 5.9.

$$\Delta\sigma_{3\max} = \frac{2T}{\delta} = \frac{2M}{\left(1-\nu_g\right)\delta} \cdot \varepsilon_{rr}^g \tag{5.9}$$

where $\delta$ is the thickness of the influential zone (i.e. $\delta$ =15 cm). Substituting Equation 5.4 into Equation 5.9 yields,

$$\Delta\sigma_{3\max} = \frac{2M}{\left(1-\nu_g\right)\delta\alpha}\cdot\varepsilon_{rr}^{a} \tag{5.10}$$

In Equation 5.10, the aggregate radial tensile strain $\varepsilon_{rr}^{a}$ is the summation of the radial elastic strain $\varepsilon_{3,r}^{a}$ and the radial plastic strain $\varepsilon_{3,p}^{a}$. The radial elastic strain $\varepsilon_{3,r}^{a}$ is calculated by the Generalized Hooke's law, as shown in Equations 5.11.

$$\varepsilon_{3,r}^{a} = \frac{\left(\sigma_3+\Delta\sigma_{3\max}\right)}{E_H} - \frac{\nu_{13}\sigma_1}{E_V} - \frac{\nu_{33}\left(\sigma_3+\Delta\sigma_{3\max}\right)}{E_H} \tag{5.11}$$

where $\sigma_3$ is the axial stress applied to the specimen, $\sigma_1$ is the initial confining pressure, $\nu_{13}$ is the Poisson's ratio to characterize the effect of axial strain on lateral strain, $\nu_{33}$ is the Poisson's ratio to characterize the effect of lateral strain on lateral strain, $E_H$ is the horizontal modulus of the specimen, and $E_V$ is the vertical modulus of the specimen. Equation 5.12 is used to calculate the axial plastic strain $\varepsilon_{1,p}^{a}$.

$$\varepsilon_{1,p}^{a} = \varepsilon_0 e^{-\left(\frac{\rho}{N}\right)^{\beta}}\left(\sqrt{J_2}\right)^{m}\left(\alpha I_1+K\right)^{n} \tag{5.12}$$

where $J_2 = \frac{1}{3}\left[\sigma_1-\left(\sigma_3+\Delta\sigma_{3\max}\right)\right]^2$, $I_1 = \sigma_1+2\left(\sigma_3+\Delta\sigma_{3\max}\right)$, and $\varepsilon_0$, $\rho$, $\beta$, $m$ and $n$ are permanent deformation properties for the unreinforced specimen. The relationship between the radial plastic strain $\varepsilon_{3,p}^{a}$ and the axial plastic strain $\varepsilon_{1,p}^{a}$ is shown in Equation 5.13.

$$\varepsilon_{3,p}^{a} = \frac{1}{2}\varepsilon_{1,p}^{a}\left(\frac{1+\sin\psi}{1-\sin\psi}\right) \tag{5.13}$$

where $\psi$ is the dilation angle of the specimen. Assuming that the dilation angle $\psi$ is 15°, Equation 5.13 is simplified as,

$$\varepsilon_{3,p}^{a} = 0.85\varepsilon_{1,p}^{a} \tag{5.14}$$

Substituting Equations 5.11, 5.12 and 5.14 into Equation 5.10 yields,

$$\Delta\sigma_{3\max} = \frac{2M}{\left(1-\nu_g\right)\delta\alpha}\cdot\left[\frac{\left(\sigma_3+\Delta\sigma_{3\max}\right)}{E_H}-\frac{\nu_{13}\sigma_1}{E_V}-\frac{\nu_{33}\left(\sigma_3+\Delta\sigma_{3\max}\right)}{E_H}+0.85\varepsilon_0 e^{-\left(\frac{\rho}{N}\right)^{\beta}}\left(\sqrt{J_2}\right)^{m}\left(\alpha I_1+K\right)^{n}\right] \tag{5.15}$$

In Equation 5.15, the only unknown parameter is the maximum additional confining stress $\Delta\sigma_{3\max}$. An iteration method is utilized to solve for this parameter.

Since the thickness of the influence zone $\delta$ is a constant, the calculated maximum additional confining stress $\Delta\sigma_{3\max}$ can be used to determine the distribution function of equivalent additional confining stress $\Delta\sigma_3(z)$ along the depth $z$ of specimen. The determined equivalent additional confining stress distribution $\Delta\sigma_3(z)$ is then input into Equation 5.16 to calculate the modified vertical modulus of the base course $E_{V-Modified}(z)$ in the influence zone.

$$E_{V-Modified}(z) = k_1 P_a\left[\frac{I_1+\Delta\sigma_3(z)}{P_a}\right]^{k_2}\left(\frac{\tau_{oct}}{P_a}+1\right)^{k_3} \tag{5.16}$$

where $I_1$ is the first invariant of the stress tensor; $\tau_{oct}$ is the octahedral shear stress; $P_a$ is the atmospheric pressure; $k_1$, $k_2$ and $k_3$ are regression coefficients. The effective vertical modulus of the entire geogrid-reinforced UGM specimen $E_{V-Effective}$ is calculated by Equation 5.17, which takes into account the variation of the location of geogrid in the UGM specimen.

$$E_{V-Effective}=\begin{cases}\dfrac{E_{V-UGM}\left(h-\delta\right)+\int_{0}^{\delta}E_{V-Modified}\left(z\right)dz}{h} & \left(\dfrac{\delta}{2}<l<h-\dfrac{\delta}{2}\right)\\ \dfrac{E_{V-UGM}\left(h-\dfrac{\delta}{2}-l\right)+\int_{0}^{\frac{\delta}{2}+l}E_{V-Modified}\left(z\right)dz}{h} & \left(l<\dfrac{\delta}{2}\right)\\ \dfrac{E_{V-UGM}\left(h-\dfrac{\delta}{2}-l\right)+\int_{0}^{\frac{\delta}{2}+h-l}E_{V-Modified}\left(z\right)dz}{h} & \left(l>h-\dfrac{\delta}{2}\right)\end{cases} \tag{5.17}$$

where $E_{V-UGM}$ is the vertical modulus of the unreinforced base course, $h$ is the thickness of the base course, and $l$ is the distance between the geogrid layer and the bottom of the base course. The effective horizontal modulus of the geogrid-reinforced UGM specimen $E_{H-Effective}$ is calculated by Equation 5.15.

$$E_{H-Effective}=n\cdot E_{V-Effective} \tag{5.18}$$

where $n$ is the ratio of the horizontal modulus to the vertical modulus, which is determined from the repeated load test. Similarly, inputting the determined equivalent additional confining stress distribution $\Delta\sigma_3\left(z\right)$ into Equation 3.6 can predict the permanent deformation of geogrid-reinforced UGM at any given stress levels.

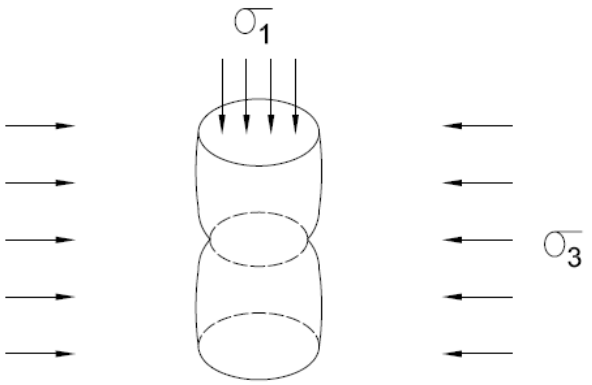


**a. Displacement Pattern of UGM Restraint by Geogrid**

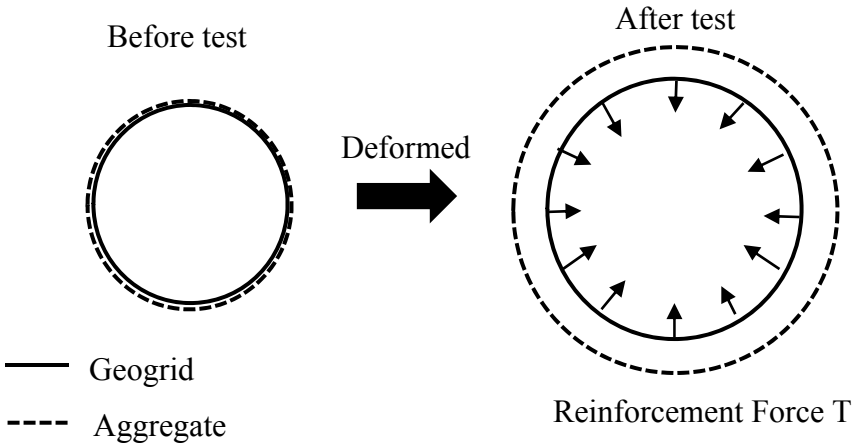


**b. Difference in Radial Movement of Geogrid and Aggregate**

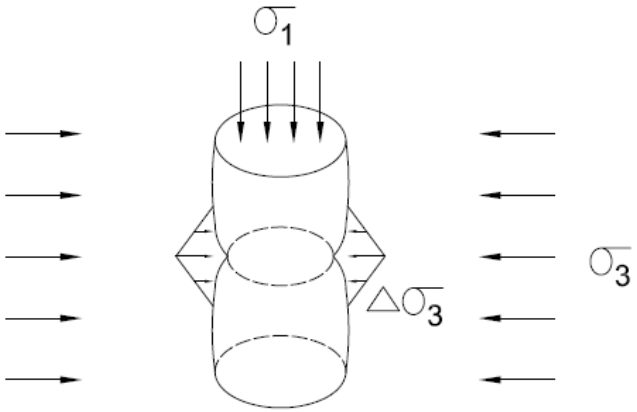


**c. Equivalence of Reinforcement Force to Additional Stress $\Delta\sigma_3$**

**Figure 5.9 Schematic Plot of Geogrid Reinforcement on UGM Specimen**

Figure 5.10 shows the comparison of the resilient moduli of geogrid-reinforced UGM predicted by the proposed analytical models and those measured from the laboratory tests. The horizontal and vertical resilient moduli predicted by the analytical models match the measured values with R-squared values of 0.96 and 0.98, respectively. This indicates that the proposed analytical models can accurately predict both the horizontal and vertical moduli of the geogrid-reinforced UGM. The analytical models will be used to characterize the lateral confinement effect of geogrid in the numerical modeling of geogrid-reinforced pavement structures.

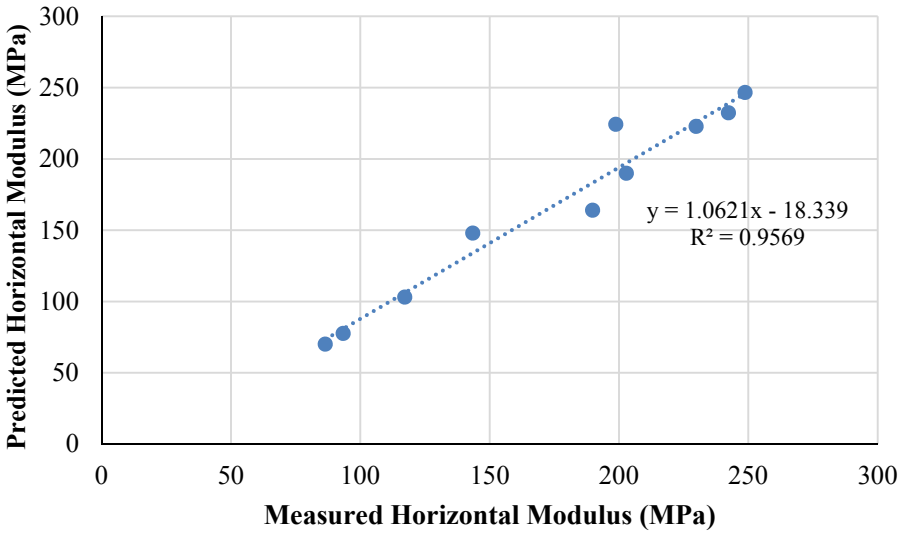


**a. Predicted Horizontal Moduli Vs. Measured Horizontal Moduli**

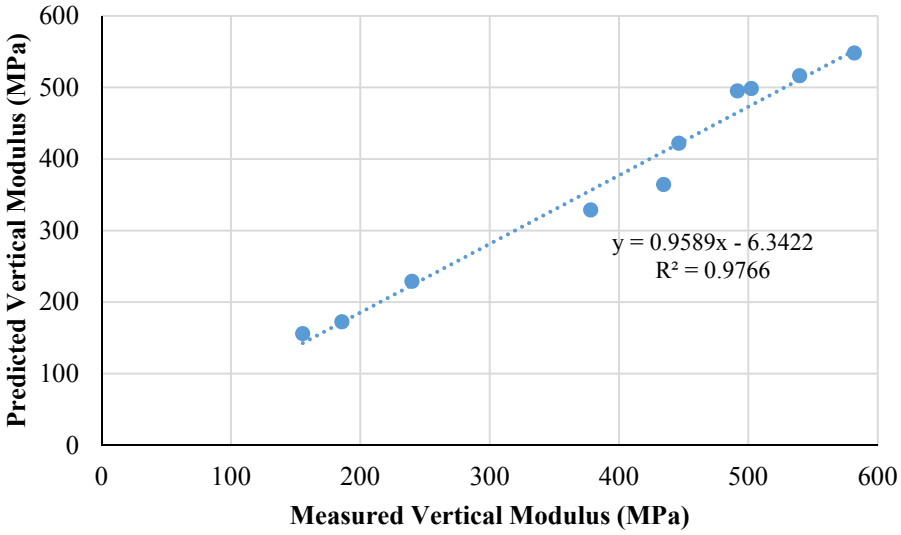


**b. Predicted Vertical Moduli Vs. Measured Vertical Moduli**

**Figure 5.10 Comparison of Resilient Moduli Predicted by Analytical Models with Measured Values**

# 6. MODELLING OF GEOGRID-REINFORCED PAVEMENT STRUCTURES USING FINITE ELEMENT APPROACH

## 6.1 Introduction

The geogrid layer has beneficial effects on the responses of pavements under traffic loading through two mechanisms: (1) generation of significant tensile stresses in the geogrid layer leading to the "lateral confinement" in materials below and above the geogrid layer, which in turn reduces the vertical stresses and increases horizontal stresses due to the improved material properties; and (2) vertical "membrane effect" resulting from the deformed geogrid layer that leads to a wider spreading and a reduction in the vertical stress around the geogrid (Giroud and Noiray 1981; Giroud et al. 1984; Perkins and Ismeik 1997b). These two mechanisms are illustrated in Figure 6.1a and are subjected to the interface condition at the geogrid-surrounding material interface. If a slip occurs at the interface, as shown in Figure 6.1b, the point A located at the base/geogrid interface will not remain as a single point but separate into two points A' and A". The occurrence of slippage at the interface may result from the reduction in the interface shear strength due to the presence of geogrids.

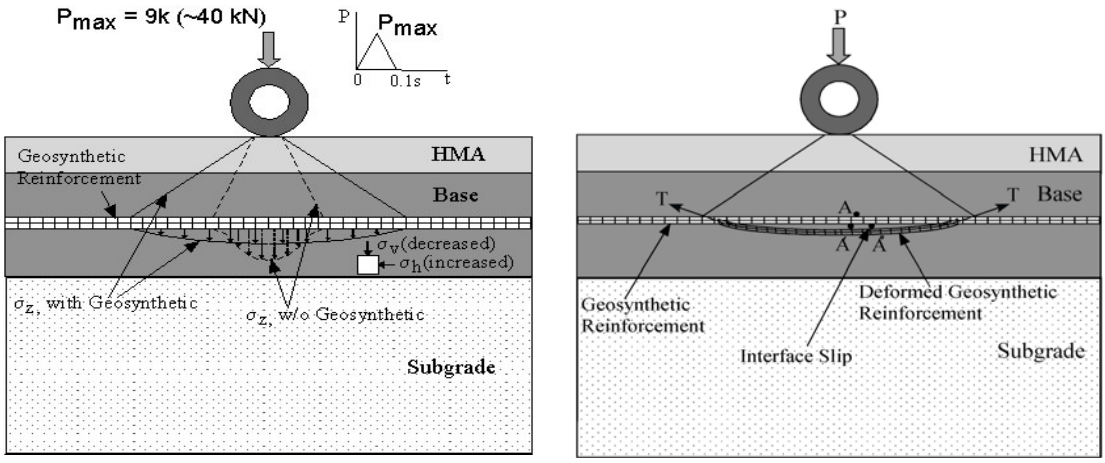


**a. Mechanisms of Geogrid in Pavement** **b. Interface Slippage**

**Figure 6.1 Pavement with a Geogrid Layer (After Perkins and Ismeik 1997b)**

Because of the positive effects of geogrids on pavement responses, using a geogrid layer in the pavement structure significantly benefits the pavement performance in terms of the reduction of pavement layer thickness, prolongation of service life and reduction of life cycle cost. These benefits have been proved in laboratory tests, in-service pavement tests and accelerated pavement tests (Al Qadi et al. 2008; Chan et al. 1989; Luo 2007).

The objective of this chapter aims to quantify the influence of geogrid on pavement performance. The finite element approach is employed to simulate the responses of geogrid-reinforced pavement structures when they are subjected to a traffic load. The finite element model of geogrid-reinforced pavement takes into account the cross-anisotropic characteristic of UGM and the lateral confinement and membrane

effect of geogrid. To validate the developed model, Soil Tank tests are conducted to measure the responses of geogrid-reinforced pavements to the specified load levels. The measurements are used to compare with the predicted responses using the finite element models. Using the validated finite element models, a large number of runs are made covering a wide range of pavement variables, including various thickness of the asphalt, base and subgrade; various levels of moduli of each layer; various anisotropic ratios of the base course; and several levels of sheet stiffness and locations of the geogrids. The neural network models are finally developed to calculate the critical strains in the geogrid-reinforced flexible pavement, which can be used to predict the pavement performance based on the distress models in Pavement ME Design.

## 6.2 Finite Element Modelling of Pavements with Geogrids

### *6.2.1 Construction of Finite Element Models*

The finite element models are developed using the software ABAQUS to simulate the Soil Tank test results (ABAQUS 2010). They are constructed for the pavement structures with and without a geogrid layer in order to determine the critical responses of the pavement to the different loading conditions. These pavement responses are used to predict the flexible pavement performance. Figure 6.2 shows a typical geogrid-reinforced pavement structure used in the Soil Tank test. It consists of a 15 cm hot mix asphalt (HMA) layer, a 25 cm unbound aggregate base course, a 0.2 cm geogrid layer and subgrade. The geogrid layer is placed between the base course and subgrade. The pavement structure is subjected to dynamic loading cycles with loading amplitudes

of 40.0 kN, 53.4 kN and 71.2 kN, respectively. The loading zone is applied with a circular loading foot with a radius of 15 cm. Figure 6.3 presents the finite element mesh of the geogrid-reinforced pavement structure in ABAQUS. The cylindrical pavement structure in the Soil Tank test is simplified as an axisymmetric model. Fine mesh is used in the vicinity of the load. The HMA layer, base course and subgrade are represented as 8-node biquadratic homogeneous solid elements with reduced integration. The geogrid layer is represented by the 3-node quadratic membrane element. The interface between the geogrid layer and the aggregate/soil layer is characterized by the Goodman element (Goodman et al. 1968).

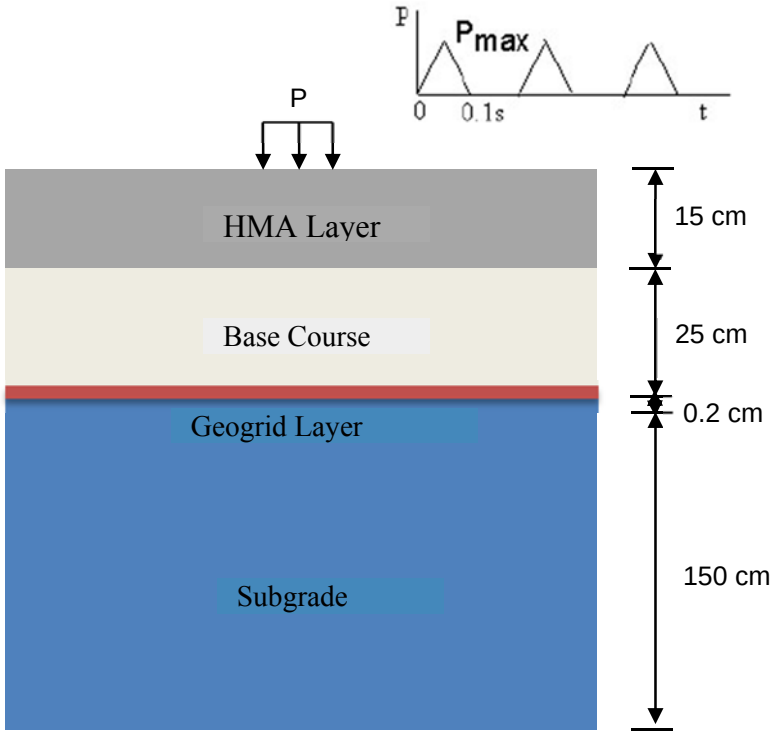


**Figure 6.2 Typical Geogrid-Reinforced Pavement Structure in Soil Tank Test**

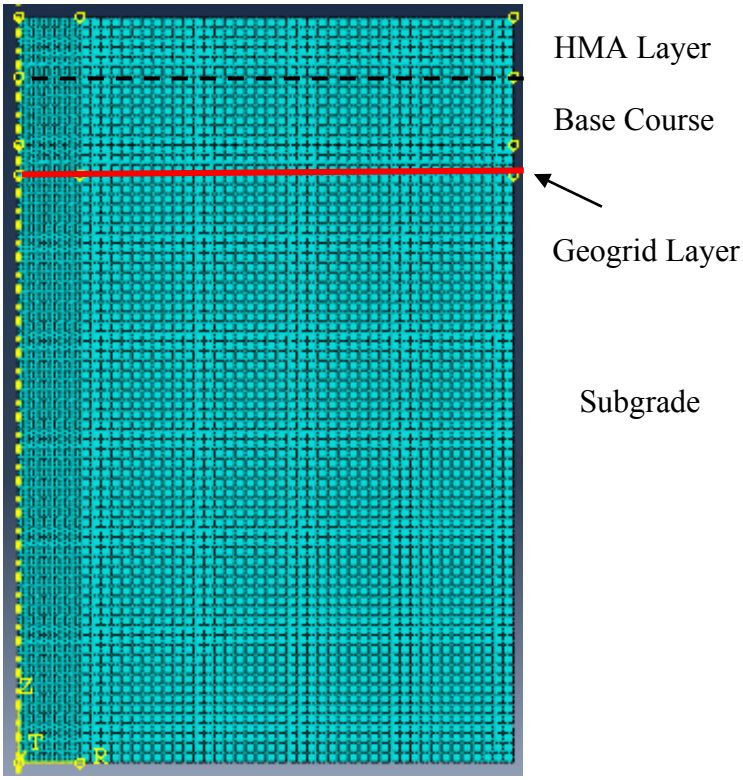


**Figure 6.3 Meshed Geogrid-Reinforced Pavement Structure in ABAQUS**

### *6.2.2 Development of Goodman Model Friction Subroutine*

When surfaces of geogrid and aggregate/soil are in contact, they usually transmit shear and normal stresses across their interface. In this study, the interface element between the geogrid surface and the aggregate/soil surface is characterized using the Goodman model (Kwon 2007), which is shown in Equation 6.1.

$$\begin{bmatrix} d\tau \\ d\sigma_n \end{bmatrix} = \begin{bmatrix} k_s & 0 \\ 0 & k_n \end{bmatrix} \begin{Bmatrix} du_r \\ dv_r \end{Bmatrix} \tag{6.1}$$

where $\tau$ is shear stress; $\sigma_n$ is normal stress; $u_r$ is relative shear displacement; $v_r$ is relative normal displacement; $k_s$ is the shear stiffness; and $k_n$ is the normal stiffness.

The interface slippage condition is quantified by the shear stiffness $k_s$. If the geogrid-aggregate/soil interface is fully bonded, the shear stiffness is assigned a large value, for example $k_s = 1 \times 10^9$ kN/m. If the slippage occurs at the geogrid-aggregate/soil interface, the shear stiffness $k_s$ is determined by Equation 6.2 using the pullout test data.

$$k_s = \frac{\Delta P}{2l \cdot \Delta u_r} \tag{6.2}$$

where $\Delta P$ is the incremental applied pullout force, $l$ is the embedded length of geogrid, and $\Delta u_r$ is the incremental relative displacement. This tangential contact behavior is defined by the user subroutine FRIC in the ABAQUS software.

### *6.2.3 Finite Element Modeling Techniques for Geogrid-Reinforced Pavement Structures*

As mentioned previously, the reinforcement mechanisms of a geogrid include the lateral confinement and the vertical membrane effect. In ABAQUS, the vertical membrane effect is simulated by assigning the geogrid as a membrane element. However the axisymmetric model cannot directly characterize the lateral confinement, which increases both the horizontal and vertical moduli of the base material. The findings of the laboratory test evaluations indicate that placing the geogrid layer in the middle or at one quarter of the sample height below the middle of the base material affects its horizontal and vertical modulus, while placing the geogrid layer at the bottom exerts a minor influence on the modulus of the base material. In this section, the lateral

confinement is simulated by assigning the geogrid-reinforced base material a higher modulus value. Figure 6.4 illustrates the schematic plot to simulate the lateral confinement in the geogrid-reinforced pavement structure. As shown in Figure 6.4a, the shaded area is an influence zone. Previous studies reported that the influence zone ranges from 10 cm to 15 cm (Schuettpelz et al 2009; McDowell et al. 2006; Perkins 2004). The range of influence zone is herein assumed to be 15 cm in height when the geogrid is placed in the middle of base course. In this range, the geogrid-reinforced base material has a higher modulus than the unreinforced material. The analytical models shown in Equations 14 and 15 are used to determine the modulus of the base material in the influence zone. The base material outside of the influence zone is considered as the unreinforced material. As shown in Figure 6.4b, when placing the geogrid at the bottom of base course, there is no influence zone in the model, which represents the modulus of the base material to be the same as that of the unreinforced material.

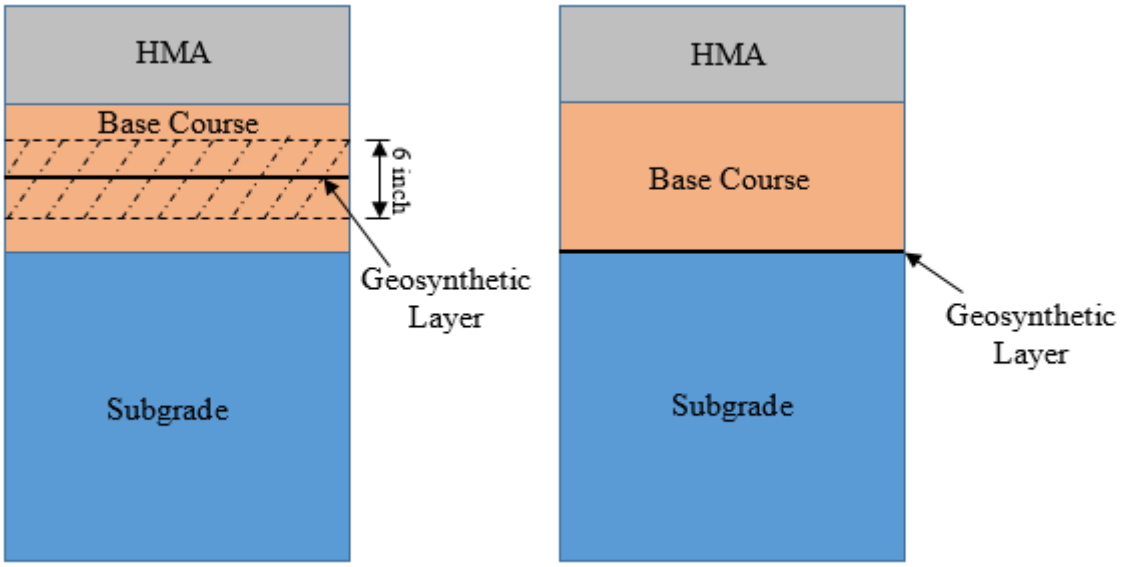


**a. Geogrid in the Middle of Base** **b. Geogrid at the Bottom of Base**

**Figure 6.4 Simulation of Lateral Confinement in Geogrid-Reinforced Pavement Structure**

## 6.3 Characterization of Materials Used in Soil Tank Test

In the developed finite element model, the HMA layer is characterized as a viscoelastic material, the base layer with and without geogrid is defined as a nonlinear cross-anisotropic elastic material, and the subgrade is assumed to be a linear elastic material. Table 6.1 presents the selected laboratory tests to characterize the materials used in the Soil Tank test and the input parameters to the finite element models.

**Table 6.1 Selected Laboratory Tests for Material Characterization**

| Material Type | Constitutive Model | Lab Test | Model Input |
|---|---|---|---|
| HMA | Viscoelastic | Dynamic modulus test | Prony series parameters ($G_i$, $K_i$, and $\tau_i$) |
| Base course | Nonlinear cross-anisotropic | Rapid triaxial test | Inputs of the developed subroutine |
| Geogrid | Elastic | Direct tension test | Tensile sheet modulus |
| Subgrade | Elastic | CBR test | Young's modulus |

In the software ABAQUS, Prony-series models are used to characterize the time-dependent viscoelastic behavior of the hot mix asphalt, which are shown in Equations 6.2 and 6.3.

$$G(t) = G_0\left(1 - \sum_{i=1}^{n} G_i\left(1 - e^{-t/\tau}\right)\right) \tag{6.2}$$

$$K(t) = K_0\left(1 - \sum_{i=1}^{n} K_i\left(1 - e^{-t/\tau}\right)\right) \tag{6.3}$$

where G(t) and K(t) are relaxation shear modulus and bulk modulus; $G_0$ and $K_0$ are instantaneous shear modulus and bulk modulus; $G_i$, $K_i$ and $\tau_i$ are the input coefficients. The method of fitting the Prony-series parameters with the dynamic modulus test result is described as follows. The relaxation modulus of a linearly viscoelastic material can be expressed as,

$$E(t) = E_{\infty}^{a} + \sum_{i=1}^{n}\left(E_i^a e^{-\frac{t}{\tau_i}}\right) \tag{6.4}$$

where E(t) is the relaxation elastic modulus; $E_{\infty}^{a}$, $E_{i}^{a}$ and $\tau_i$ are the regression coefficients in the model. Accordingly, the storage and loss moduli can be expressed by Equations 6.5 and 6.6. The magnitude of the dynamic modulus is given by Equation 6.7.

$$E'(\omega) = E_{\infty}^{a} + \sum_{i=1}^{n} \frac{\omega^2 \tau_i^2 E_{\infty}^{a}}{1+\omega^2 \tau_i^2} \tag{6.5}$$

$$E''(\omega) = \sum_{i=1}^{n} \frac{\omega \tau_i E_{\infty}^{a}}{1+\omega^2 \tau_i^2} \tag{6.6}$$

$$\left|E^*\right| = \sqrt{E'^2 + E''^2} \tag{6.7}$$

where $E'(\omega)$ and $E''(\omega)$ are the storage and loss modulus respectively; $\omega$ is the angular velocity; $\left|E^*\right|$ is the magnitude of the dynamic modulus. By fitting the dynamic modulus test result, the unknown parameters in Equation 6.4 can be determined based on the least square error criterion. As can be observed from Equations 6.2 and 6.4, the form of the Prony-series model in ABAQUS is slightly different from the model used for fitting the dynamic modulus test result. Parameter conversions between Equation 6.2 and 6.4 are required and provided by Equations 6.8-6.12. Table 6.2 lists the determined Prony-series model coefficients, which are used to characterize the asphalt concrete in ABAQUS. Figure 6.5 compares the fitted dynamic moduli and the measured ones. It is seen that the fitted dynamic moduli can accurately match the dynamic modulus test result.

$$E_0 = E_{\infty}^{a} + \sum_{i=1}^{n} E_i^{a} \tag{6.8}$$

$$E_i = \frac{E_i^{a}}{E_0} \tag{6.9}$$

$$G_0 = \frac{E_0}{2(1+\nu)} \tag{6.10}$$

$$K_0 = \frac{E_0}{3(1-2\nu)} \tag{6.11}$$

$$G_i = K_i = E_i \tag{6.12}$$

where $E_0$ is the instantaneous elastic modulus; ν is the Poisson's ratio.

**Table 6.2 Determined Prony-series Model Coefficients for the Asphalt Concrete**

| | **Prony-Series Coefficients** | | |
|---|---|---|---|
| **i** | **$G_i$** | **$K_i$** | **$\tau_i$** |
| 1 | 0.362 | 0.362 | 4.09E-06 |
| 2 | 0.363 | 0.363 | 2.56E-04 |
| 3 | 0.1765 | 0.1765 | 7.71E-03 |
| 4 | 0.074 | 0.074 | 2.10E-01 |
| 5 | 0.0165 | 0.0165 | 3.88E+00 |
| 6 | 0.0057 | 0.0057 | 6.53E+01 |
| Elastic parameters: instantaneous modulus = 18,130 MPa; Poisson's ratio = 0.35 | | | |

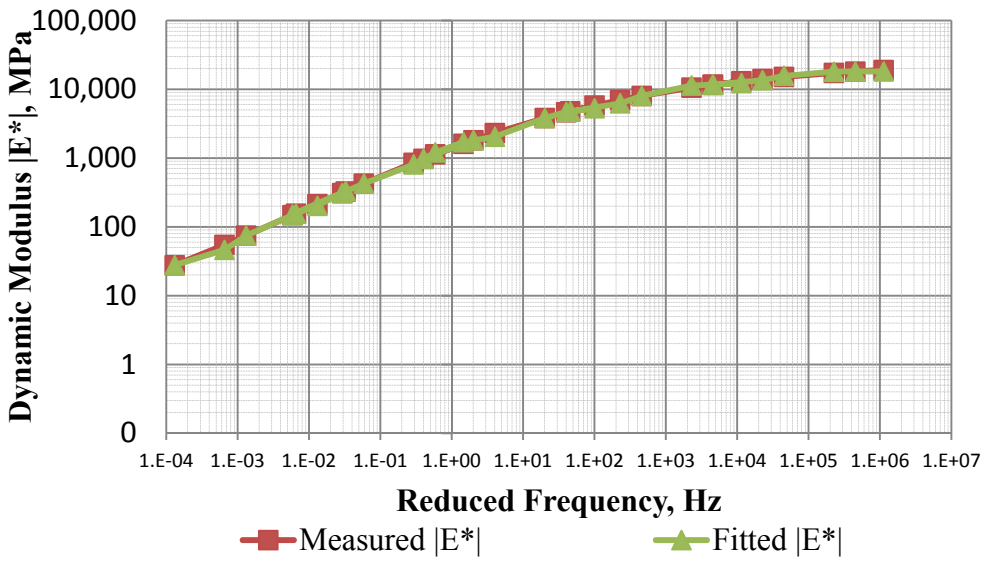


**Figure 6.5 Comparison between the Measured Dynamic Moduli and the Fitted Dynamic Moduli**

As stated in the previous section, the RaTT is employed to determine the cross-anisotropic properties of the UGM used in the Soil Tank test. The test data are given in Appendix L. The constitutive models of the UGM used in this study are shown in Equations 6.13 to 6.15.

$$E_y = k_1 P_a \left(\frac{I_1}{P_a}\right)^{k_2} \left(\frac{\tau_{oct}}{P_a} + 1\right)^{k_3} \tag{6.13}$$

$$n = \frac{E_x}{E_y} \tag{6.14}$$

$$m = \frac{G_{xy}}{E_y} \tag{6.15}$$

where $I_1$ is the first invariant of the stress tensor; $\tau_{oct}$ is the octahedral shear stress; $P_a$ is the atmospheric pressure; $k_1$, $k_2$ and $k_3$ are regression coefficients; $E_x$ is the horizontal resilient modulus; $E_y$ is the vertical resilient modulus; and $G_{xy}$ is the shear modulus in the $x-y$ plane. Table 6.3 presents the cross-anisotropic properties of the UGM determined in the Soil Tank test.

**Table 6.3 Cross-Anisotropic Properties of the UGM Used in Soil Tank Test**

| **Parameters** | **$k_1$** | **$k_2$** | **$k_3$** | **n** | **m** | **$\nu_{xy}$** | **$\nu_{xx}$** |
|---|---|---|---|---|---|---|---|
| **Values** | 1545 | 0.75 | -0.1 | 0.45 | 0.35 | 0.17 | 0.43 |

As shown in Figure 6.6, the direct tension tests are conducted to determine the sheet modulus of geogrid products used in the Soil Tank tests. Figure 6.7 shows the relationships between the tensile force and the tensile strain for the tested geogrid. "MD" is the abbreviation for machine direction. "XMD" is the abbreviation for cross machine direction. It is seen that geogrid in the machine direction has a smaller sheet modulus than that in the cross machine direction. The ductility of geogrid in the machine direction is much higher than that in the cross machine direction. The sheet moduli at 2% strain and 5% strain are compared to the data in the manufacturer's specifications, as shown in Table 6.4. It is found that all of the determined geogrid sheet moduli are higher than the data in the manufacturer's specifications.

**Figure 6.6 Direct Tension Test for Determining Sheet Modulus of Geogrid**

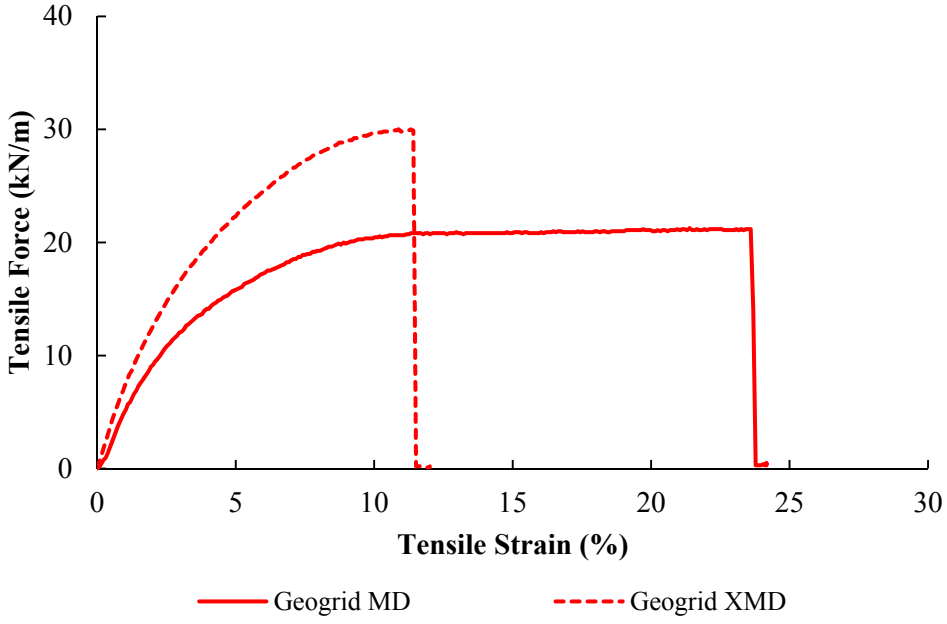


**Figure 6.7 Relationships between Tensile Force and Tensile Strain for Geogrid**

**Table 6.4 Comparison of Geogrid Sheet Modulus Values between Laboratory Test and Manufacture's Specifications**

| Geogrid Direction | Mechanical Properties-Test | | Mechanical Properties-Specification | |
|---|---|---|---|---|
| | Sheet Modulus @ 2% Strain (MPa) | Sheet Modulus @ 5% Strain (MPa) | Sheet Modulus @ 2% Strain (MPa) | Sheet Modulus @ 5% Strain (MPa) |
| Geogrid MD Value | 232 | 161 | 150 | 118 |
| Geogrid XMD Value | 316 | 225 | 225 | 196 |

## 6.4 Comparison of Finite Element Simulations with Soil Tank Measurements

The finite element simulation results of the developed geogrid-reinforced and unreinforced pavement models are validated by comparing them to the Soil Tank test measurements in terms of the surface deflection, tensile strain at the bottom of the asphalt concrete, and vertical pressures within the base and subgrade layers. Figure 6.8 illustrates the location of the instruments, such as the LVDTs, the tensile strain gauge, and the pressure sensors in the flexible pavement structures.

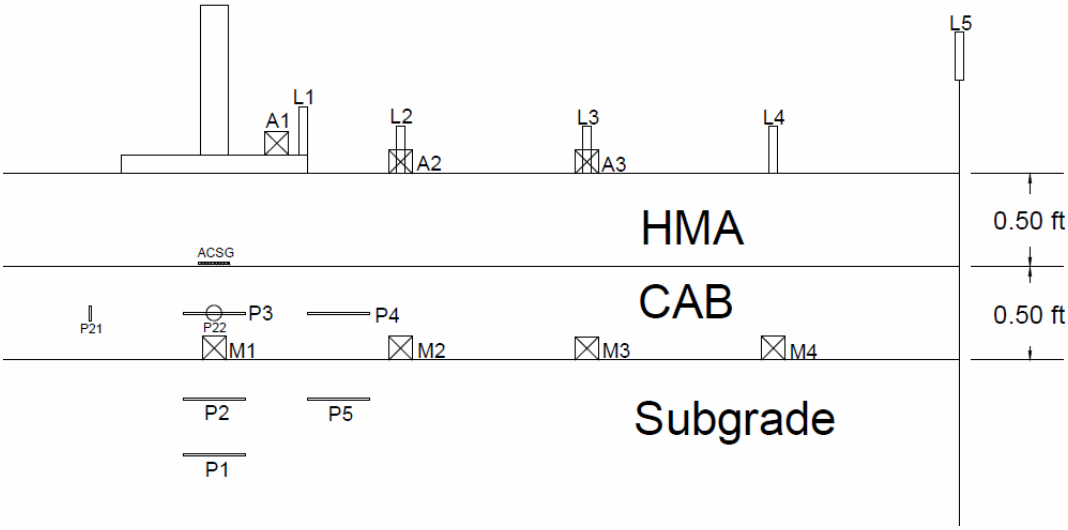


**a. Flexible Pavement with 15 cm Base Course**

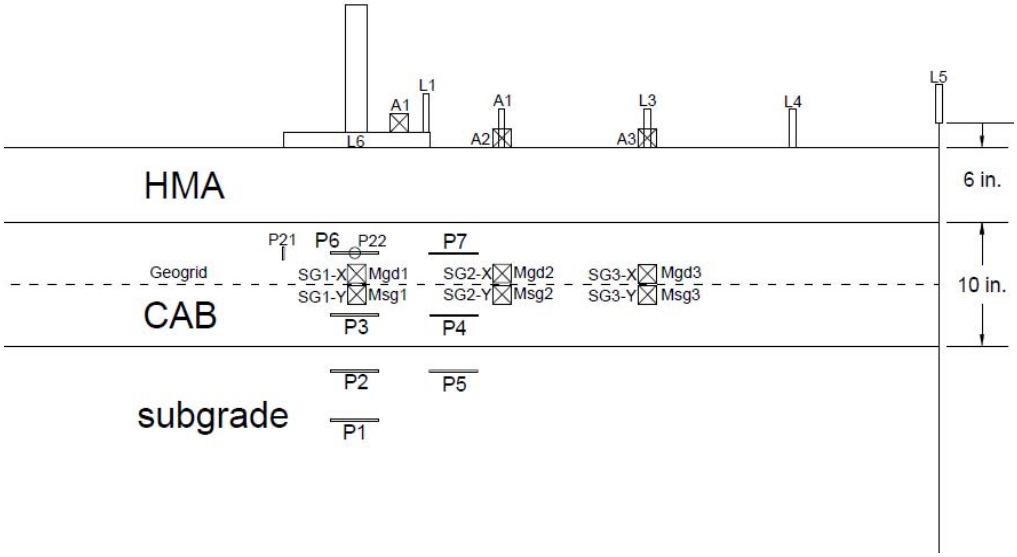


**b. Flexible Pavement with 25 cm Base Course**

**Figure 6.8 Location of Instruments in Flexible Pavement Structures**

Figure 6.9 shows the comparison of the surface deflections predicted by the finite element models and the Soil Tank test measurements when the pavement structures are

subjected to a 40.0 kN load. The model-predicted surface deflections are in agreement with the Soil Tank measurements from LVDTs 1, 2, and 3. The deviation between the measured surface deflection by LVDT 4 and that predicted by the finite element model exists because the surface deflection at this location is too small to be accurately captured by the LVDT. This indicates that the developed geogrid-reinforced and unreinforced pavement models have high accuracy to predict the pavement surface deflections. The comparison of the tensile strain at the bottom of asphalt concrete is plotted in Figure 6.10. It is seen that the developed finite element models accurately predict the tensile strain in the geogrid-reinforced and unreinforced pavement structures. Figure 6.11 presents the comparison between the predicted vertical pressures within the base and subgrade layer and the measured results. Most of the measured pressure values are captured by the developed finite element models, except the measurement of pressure cell $P_1$ and $P_7$. There are a number of possible explanations for these discrepancies, including, for sensor $P_1$ that the stress dependent behavior of the subgrade was not taken into account (See Figures 6.11a and 6.11b). For sensor $P_7$ in Figure 6.11b, the measured pressure being lower than the predicted may be due to arching over the sensor.

In summary, the finite element simulation results are in good agreement with the Soil Tank test measurements for both the reinforced and unreinforced pavement structures. The considerations of the paving material characterization, the geogrid-aggregate/soil interface characterization, and the reinforcement influence zone are

important to develop accurate numerical models of geogrid-reinforced pavement structures.

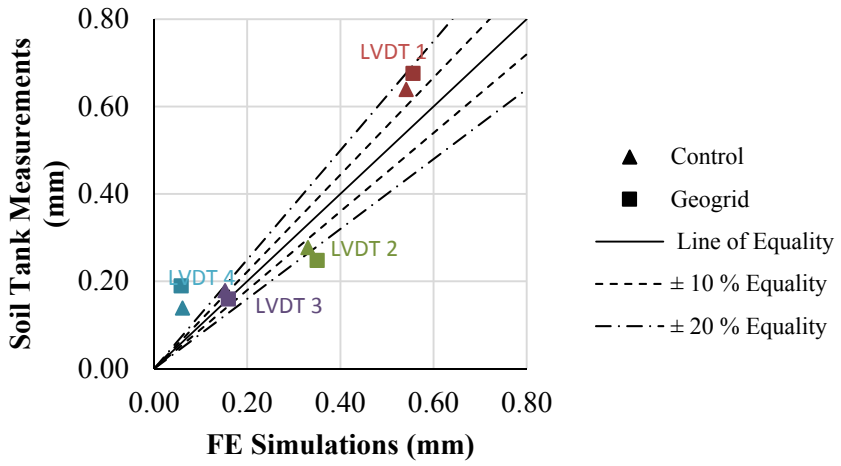


**a. Pavement Structures with 15 cm Base Course**

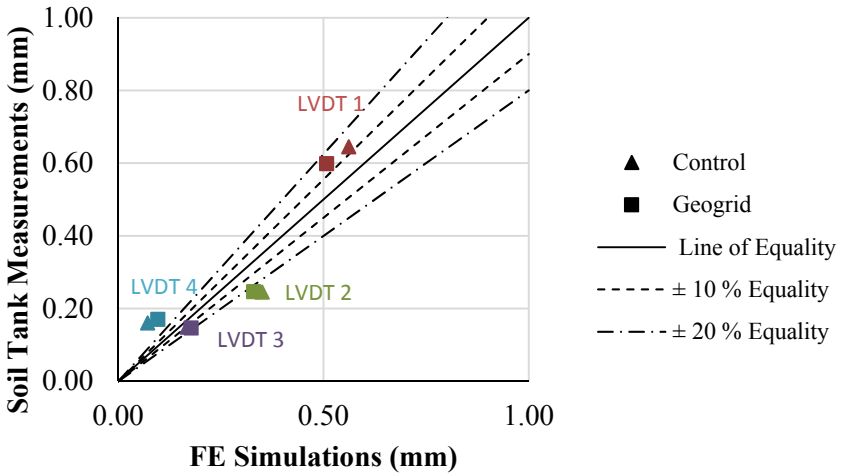


**b. Pavement Structures with 25 cm Base Course**

**Figure 6.9 Comparison of Measured and Predicted Surface Deflections for Pavements with and without Geogrid**

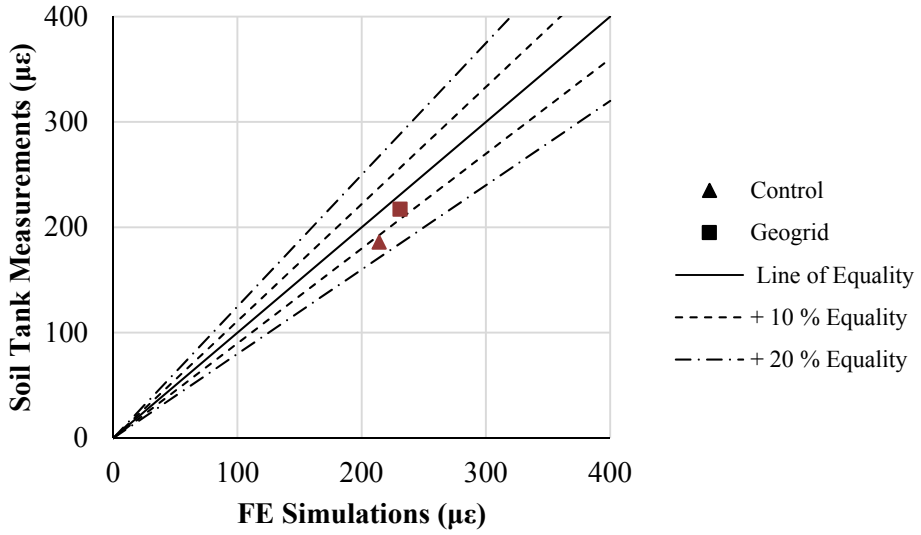


**a. Pavement Structures with 15 cm Base Course**

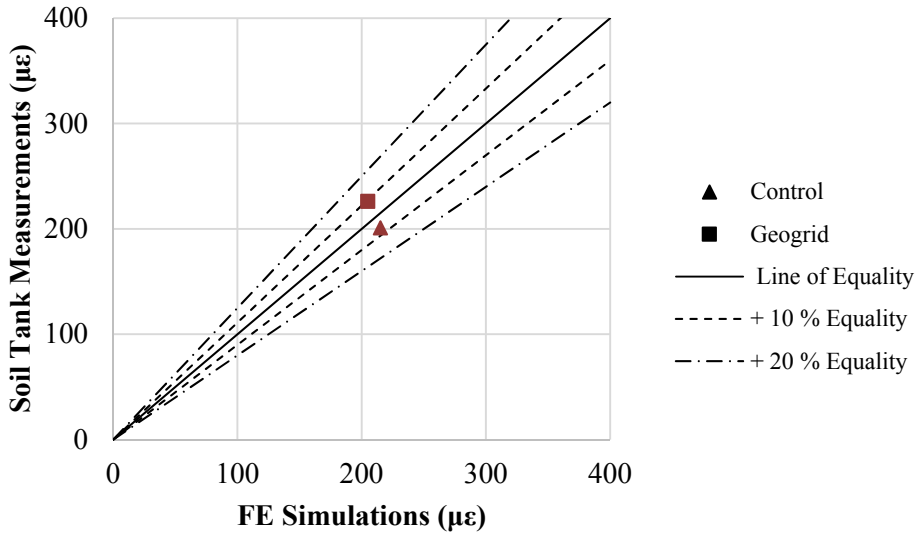


**b. Pavement Structures with 25 cm Base Course**

**Figure 6.10 Comparison of Measured and Predicted Tensile Strains at the Bottom of Asphalt Concrete for Pavements with and without Geogrid**

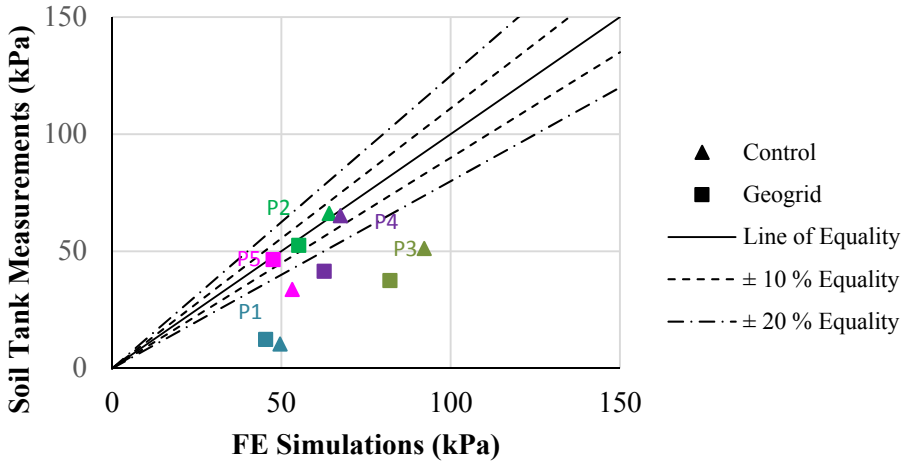


**a. Pavement Structures with 15 cm Base Course**

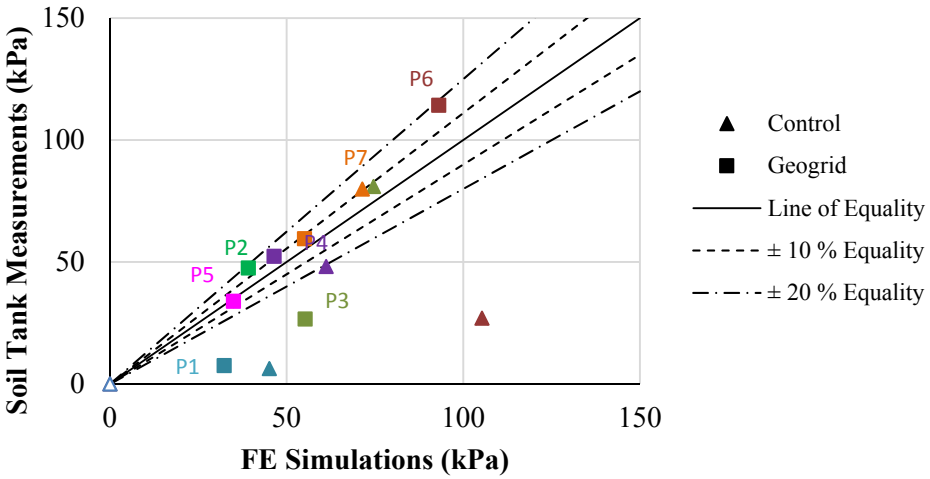


**b. Pavement Structures with 25 cm Base Course**

**Figure 6.11 Comparison of Measured and Predicted Vertical Stresses within the Base and Subgrade for Pavements with and without Geogrid**

## 6.5 Parametric Study of Material Properties on Pavement Performance

The sensitivity analysis of the pavement responses predicted by the finite element model is conducted by varying the material properties, such as the subgrade modulus and the geogrid sheet modulus, and the thickness of the base course. It is found that the primary advantage of geogrid reinforcement is the reduction of the vertical compressive strain in the base course and at the top of subgrade. Therefore, the pavement responses studied in the sensitivity analysis specifically refer to these two critical strains. The unreinforced pavement structure consisted of a 10 cm HMA layer, a 15 cm base course, and the subgrade is analyzed as the control group. The control structure is also reinforced by the geogrid placed in the middle or at the bottom of the base course.

Figures 6.12a and 6.12b show the sensitivity of the model-predicted pavement responses to the variations in the subgrade modulus. The selected subgrade moduli are 35 MPa, 105 MPa and 175 MPa, which represent the poor, fair and good quality of subgrade, respectively. The increase of subgrade modulus remarkably decreases the vertical strain at the top of subgrade, but slightly increases the vertical strain within the base layer. The placement of the geogrid is effective in reducing these two critical strains. The reduction of the critical strains due to the geogrid reinforcement are normalized using Equation 6.16.

$$Normalized\ reduction\ of\ strain = \frac{Strain\_Control - Strain\_Geogrid}{Strain\_Control} \times 100\% \quad (6.16)$$

where $Strain\_Control$ is the computed critical strain in the control model, $Strain\_Geogrid$ is the computed critical strain in the geogrid-reinforced model.

Figure 6.13a indicates that the reduction of the vertical strain at the top of subgrade is significant when the geogrid is placed at the bottom of the base course. The increase of subgrade modulus slightly decreases the reduction percentage by the presence of the geogrid. Figure 6.13b illustrates that the geogrid reinforced in the middle of the base course effectively reduces the vertical strain, while the geogrid located at the bottom of base course slightly increases the base vertical strain. With the increase of subgrade modulus, the normalized reduction of the base vertical strain due to geogrid decreases by approximately 5%. This indicates that the geogrid reinforcement is more effective when it is placed over a weak subgrade, which normally has a low resilient modulus.

Figures 6.14a and 6.14b show the sensitivity of the pavement responses predicted by the model to the variation of the geogrid sheet stiffness. Both the vertical strain at the top of subgrade and the average vertical strain within the base layer decrease with the geogrid sheet stiffness. This indicates that the geogrid with a higher sheet stiffness is more efficient in reducing the permanent deformation of the pavement structure.

Figure 6.15 indicates that the developed geogrid-reinforced and unreinforced pavement models are also sensitive to the thickness of the base course in predicting the vertical strains in the base layer and the subgrade. It is seen that increasing the thickness of the base course reduces both the vertical compressive strain at the top of subgrade and the vertical strain within the base course. The geogrid reinforcement is more effective for a thin base layer in terms of the percent reduction of vertical strains in the base and subgrade.

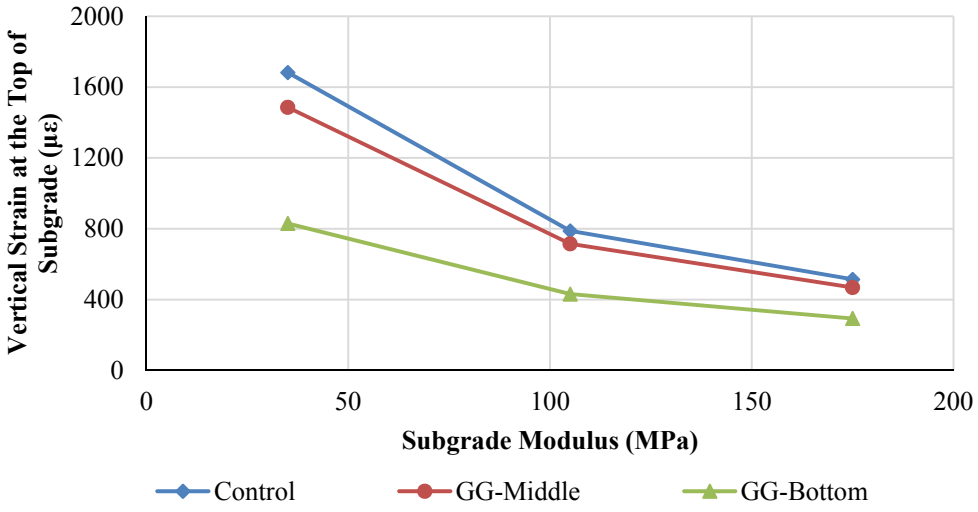


**a. Computed Vertical Strain at the Top of Subgrade**

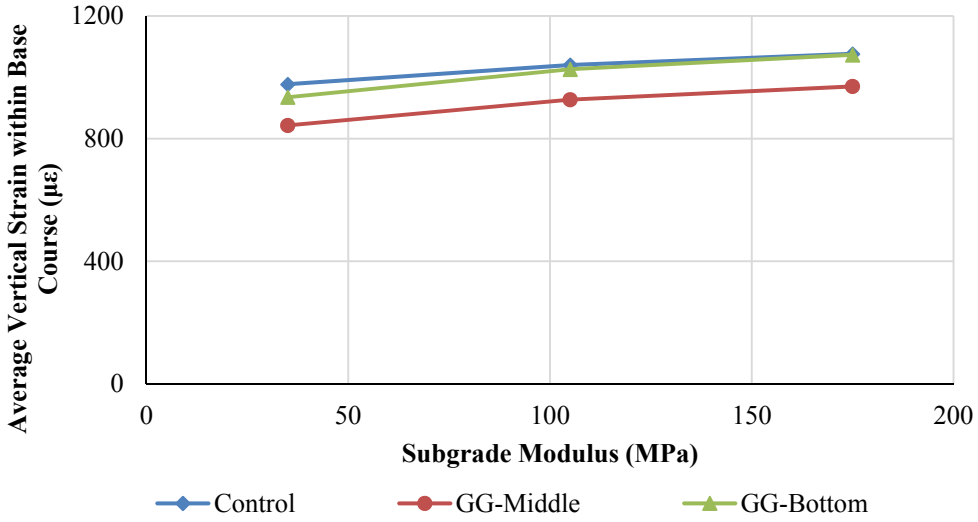


**b. Computed Average Vertical Strain within Base Course**

**Figure 6.12 Computation of Model-Predicted Pavement Responses by Varying Subgrade Modulus**

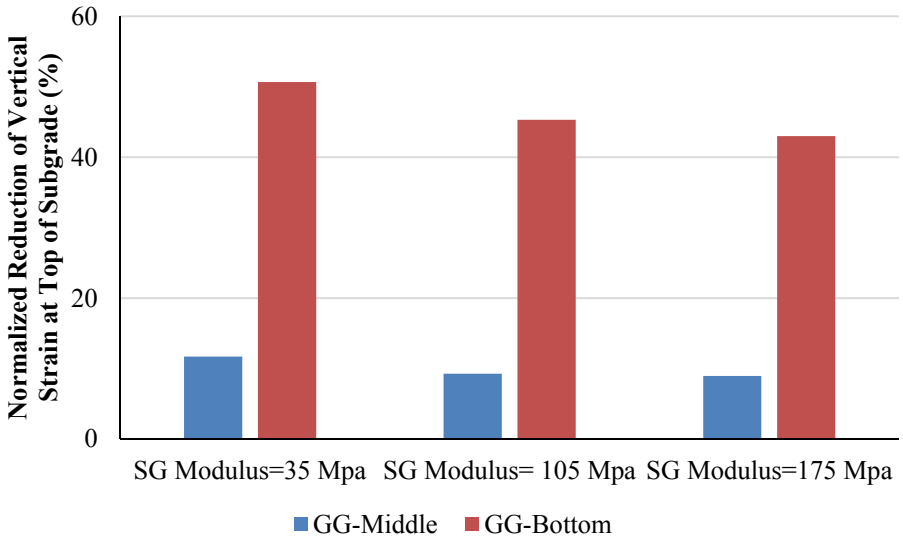


**a. Normalized Reduction of Vertical Strain at the Top of Subgrade**

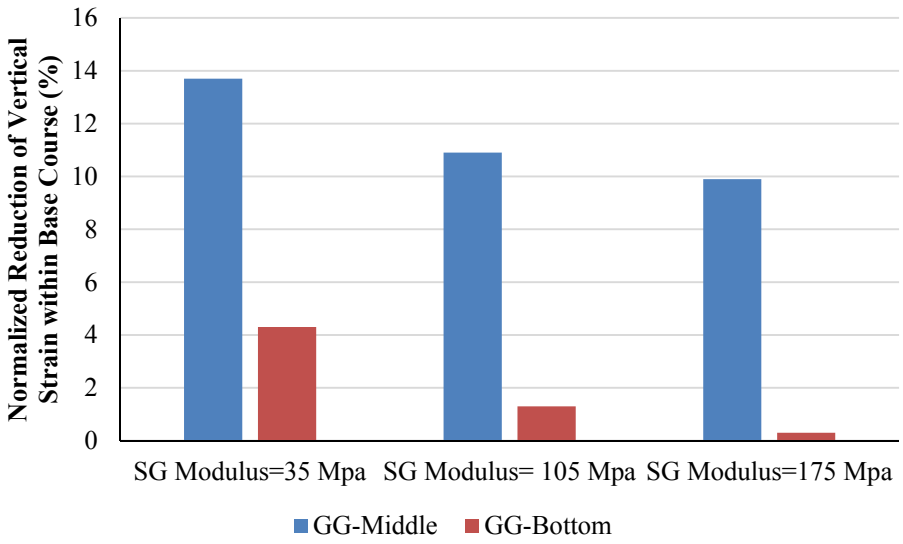


**b. Normalized Reduction of Vertical Strain within Base Course**

**Figure 6.13 Sensitivity of Model-Predicted Pavement Responses to Subgrade Modulus**

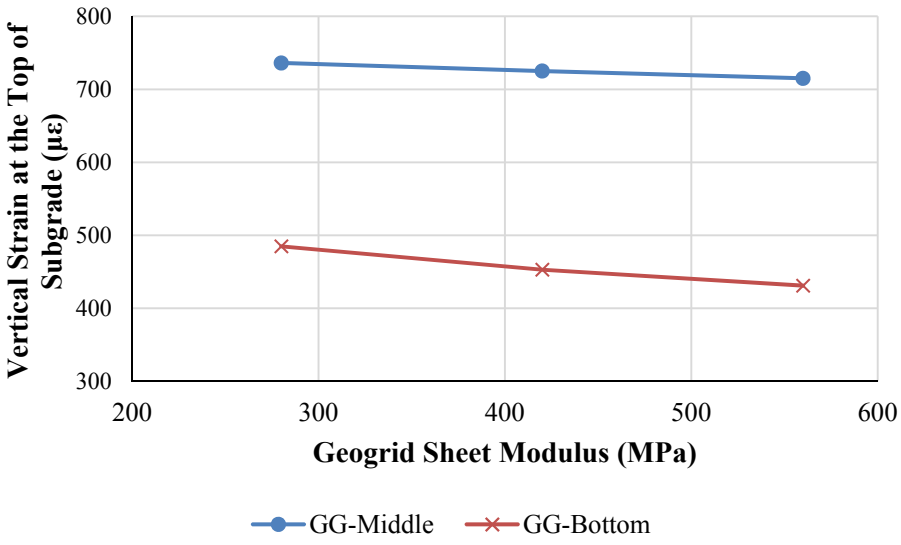


**a. Vertical Strain at the Top of Subgrade**

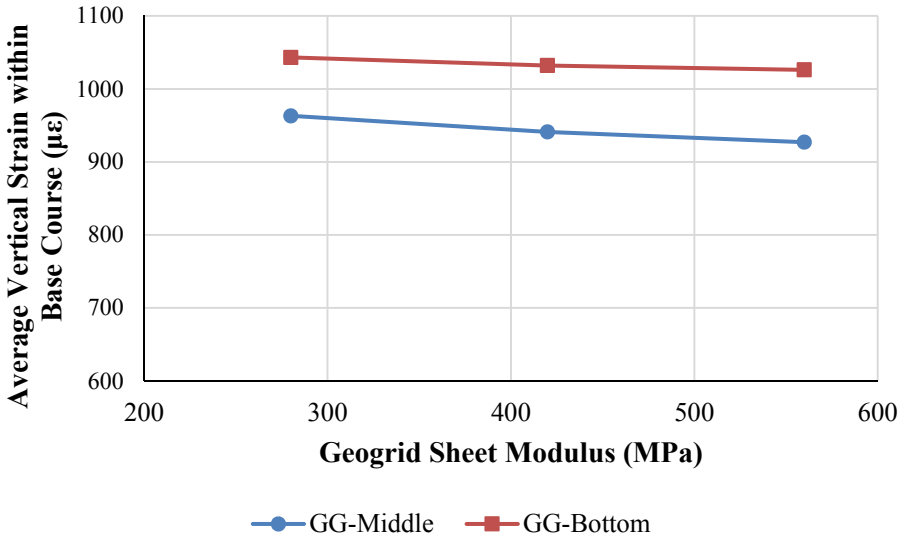


**b. Average Vertical Strain within the Base Course**

**Figure 6.14 Sensitivity of Model-Predicted Pavement Responses to Geogrid Sheet Modulus**

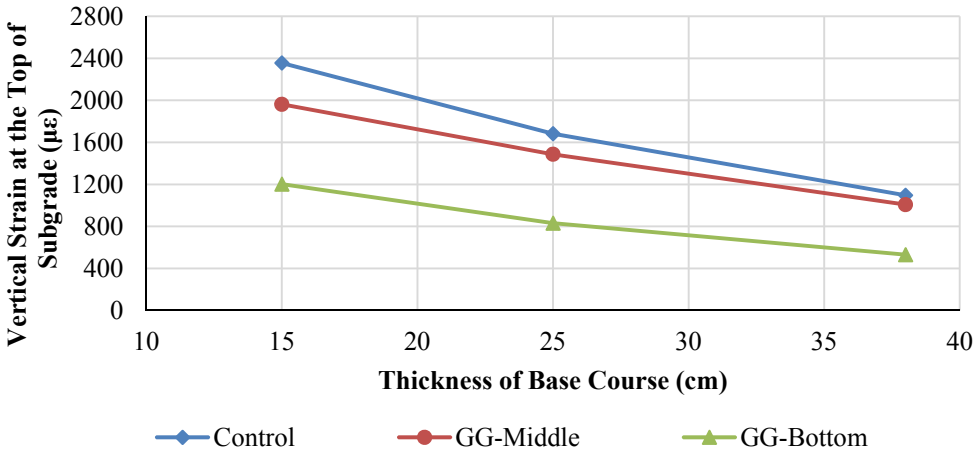


**a. Computed Vertical Strain at the Top of Subgrade**

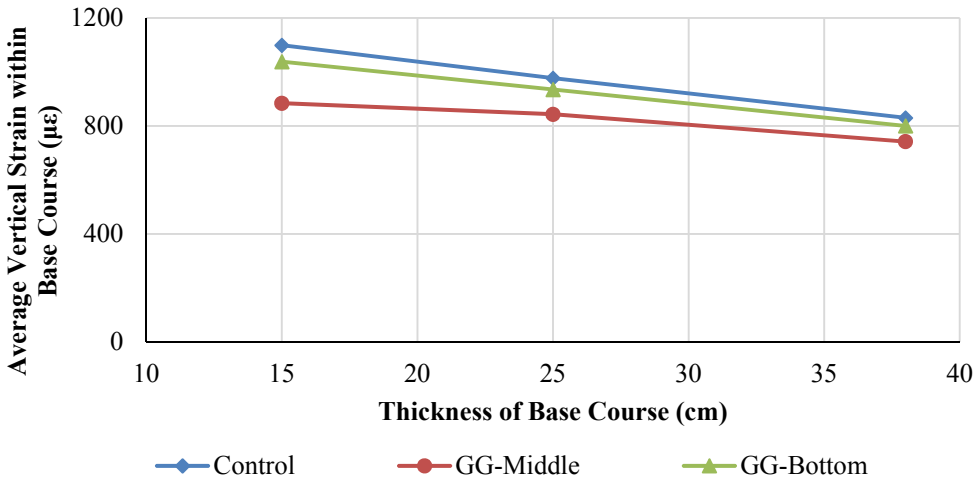


**b. Computed Average Vertical Strain within Base Course**

**Figure 6.15 Sensitivity of Model-Predicted Pavement Responses to Thickness of Base Course**

## 6.6 Artificial Neural Network Approach for Predicting Pavement Performance

### *6.6.1 Background of Artificial Neural Network Approach*

The current Pavement ME Design software predicts the pavement performance based on the computed critical pavement responses from a linear isotropic and layered elastic program. In other words, the determination of critical pavement responses are the key to forecasting the pavement performance. The finite element models developed in this project are sufficiently accurate to compute the critical responses of geogrid-reinforced pavement structures. However, these models are developed using the software ABAQUS, which is not compatible with the Pavement ME Design embedded software DARWin-ME. Furthermore, replacing the current Pavement ME Design software with the developed finite element models to compute the critical responses of the arbitrary user-inputted geogrid-reinforced pavement structures is impractical at the moment. Therefore, there is a need to predict the responses of any given geogrid-reinforced pavement structure based on computation by the developed finite element models for a wide range of geogrid-reinforced pavement structures.

To satisfy this need, the Artificial Neural Network (ANN) approach is used to predict the critical responses of geogrid-reinforced pavement structures. The ANN models allow establishing the correlations between the input variables $X_i$ and the output variables $Y_j$ through the inter-connected neurons (i.e. weight factor $w_{ji}$). Note that the input variables $X_i$ and the output variables $Y_j$ are usually normalized to $x_i$ and $y_j$ respectively, which are the values between 0 and 1. Herein, the output variables $Y_j$

represent the computed critical pavement responses, including the tensile strain at the bottom of the asphalt concrete, and the compressive strain within the asphalt concrete, base layer and subgrade. The selection of the input parameters $X_i$ is based on the sensitivity analysis of the developed finite element models. The identified input parameters to the ANN model include the layer thickness, the modulus of the paving material, the location of the geogrid, and the type of geogrid. The correlations developed by the ANN models between the normalized input parameters $x_i$ and the normalized output variables $y_j$ are shown in Equation 37.

$$y_j = f\left(\sum_{i=1}^{n} w_{ji} x_i\right) \tag{6.17}$$

where $f$ is a transfer function, which normally uses a sigmoidal, Gaussian , or threshold functional form, and $w_{ji}$ are the unknown weight factors. Developing a neural network model specifically refers to the determination of the weight factors $w_{ji}$ in Equation 37. The ANN model determines these weight factors $w_{ji}$ through the two major functions: training and validating. The training data set is used to determine the trial weight factors $w_{ji}$, and the validating data set is employed to examine the accuracy of the model prediction. A robust ANN model normally requires a large database of input and output variables (Wu et al. 2014). Thus, generating the input and output variables database is the first step in developing the ANN model.

### *6.6.2 Experimental Computational Plan for ANN Models*

To generate the database of the numerical model inputs and the corresponding computed critical pavement responses, the computation of multiple cases is performed based on the developed geogrid-reinforced and unreinforced finite element models. Tables 6.5 and 6.6 show the selected input parameters as well as their values for the geogrid-reinforced pavement structures and the corresponding unreinforced pavement structures, respectively. Based on these experimental computational plans, the number of the computed geogrid-reinforced pavement models is 2916, and the number of the computed unreinforced pavement models is 486. From Table 6.5, three geogrid sheet stiffness values and two geogrid locations (middle and bottom of base course) are taken into account in the computation of the multiple cases. The pavement responses database is divided into 3 categories, including

- The geogrid placed in the middle of base layer (GG-M),
- The geogrid placed at the bottom of base layer (GG-B), and
- The unreinforced one (NG).

Each category of pavement response database corresponds to one set of neural network models.

**Table 6.5 Selected Input Parameters for Geogrid-Reinforced Pavement Structures**

| Influential Factors | Level | Input Values |
|---|---|---|
| Load Magnitude | 1 | 40.0 kN |
| HMA Thickness | 3 | 5, 10 and 15 cm |
| HMA Modulus | 3 | 2100, 3150 and 4200 MPa |
| Base Thickness | 3 | 15, 25 and 38 cm |
| Base Vertical Modulus | 3 | 140, 280 and 420 MPa |
| Base Anisotropic Ratio | 2 | 0.35 and 0.45 |
| Geogrid Location | 2 | Middle and Bottom of Base Course |
| Geogrid Sheet Modulus | 3 | 200, 400 and 600 MPa |
| Subgrade Modulus | 3 | 35, 105 and 175 MPa |
| The Number of Total Cases is 2916. | | |

**Table 6.6 Selected Input Parameters for Unreinforced Pavement Structures**

| Influential Factors | Level | Input Values |
|---|---|---|
| Load Magnitude | 1 | 40.0 kN |
| HMA Thickness | 3 | 5, 10 and 15 cm |
| HMA Modulus | 3 | 2100, 3150 and 4200 MPa |
| Base Thickness | 3 | 15, 25 and 38 cm |
| Base Vertical Modulus | 3 | 140, 280 and 420 MPa |
| Base Anisotropic Ratio | 2 | 0.35 and 0.45 |
| Subgrade Modulus | 3 | 35, 105 and 175 MPa |
| The Number of Total Cases is 486. | | |

### *6.6.3 Selection of ANN Algorithms*

A three-layered neural network architecture consisting of one input layer, one hidden layer and one output layer is constructed as shown Figure 6.16. The input parameters are listed in Tables 6.5 and 6.6, except the geogrid location. The output variables are the critical pavement responses, including the tensile strain at the bottom of asphalt concrete, and the compressive strains within asphalt concrete, base course and

subgrade. The hidden layer assigns 20 neurons to establish the connection between the output layer and the input layer. In this study, the transfer function uses a sigmoidal functional form, which is shown in Equation 38 (Ceylan et al. 2014).

$$f\left(I_i\right)=\frac{1}{1+\exp\left(-\varphi I_i\right)} \tag{6.18}$$

where $I_i$ is the input quantity, $\varphi$ is a positive scaling constant, which controls the steepness between the two asymptotic values 0 and 1. The constructed neural network structure is programmed by the software MATLAB 2013a (Demuth and Beale 1998). The training algorithm uses the Levenberg-Marquardt back propagation method to minimize the mean squared error (MSE) (More 1978). The gradient descent weight function is employed as a learning algorithm to adjust the weight factors $w_{ji}$ (Amari 1998).

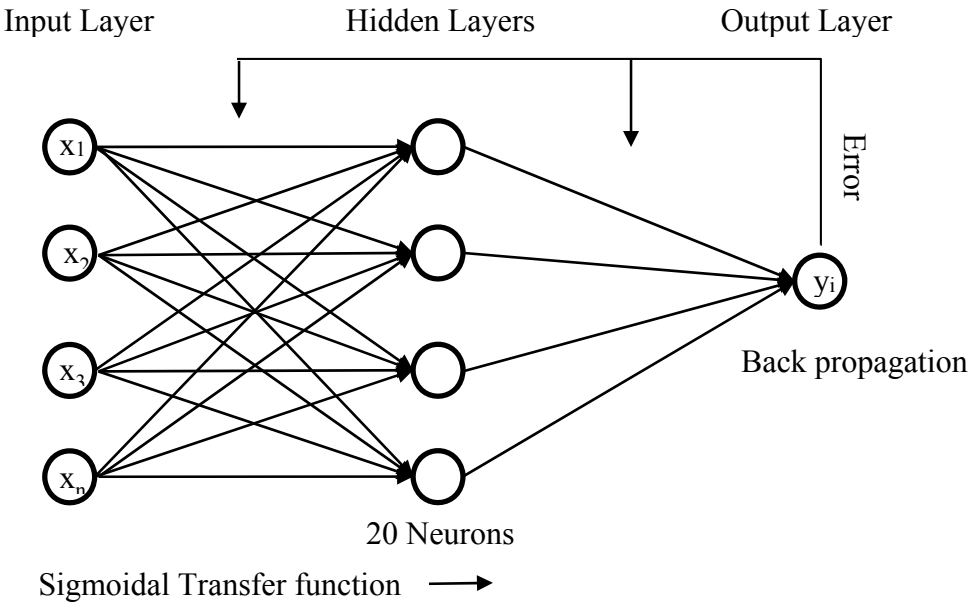


**Figure 6.16 Illustration of Three-Layered Neural Network Architecture**

### *6.6.4 Prediction of Pavement Responses*

The pavement response database is first randomly divided into a training data set and a validating data set as the ratio of 80% and 20% respectively. The training data set is used to determine the weight factors $w_{ji}$, and the validating data set is employed to examine the prediction accuracy of the developed neural network. Figures 6.17-6.21 show the comparisons between the finite element model-computed pavement responses and the ANN model-predicted pavement responses for the GG-M structure. The ANN models accurately predict all of the pavement responses from the validating data set after the training process. The developed ANN models are used to interpolate the critical responses of any given geogrid-reinforced pavement structure. The predicted pavement

responses can be input into the Pavement ME Design Models to calculate the fatigue cracking, rutting and international roughness index.

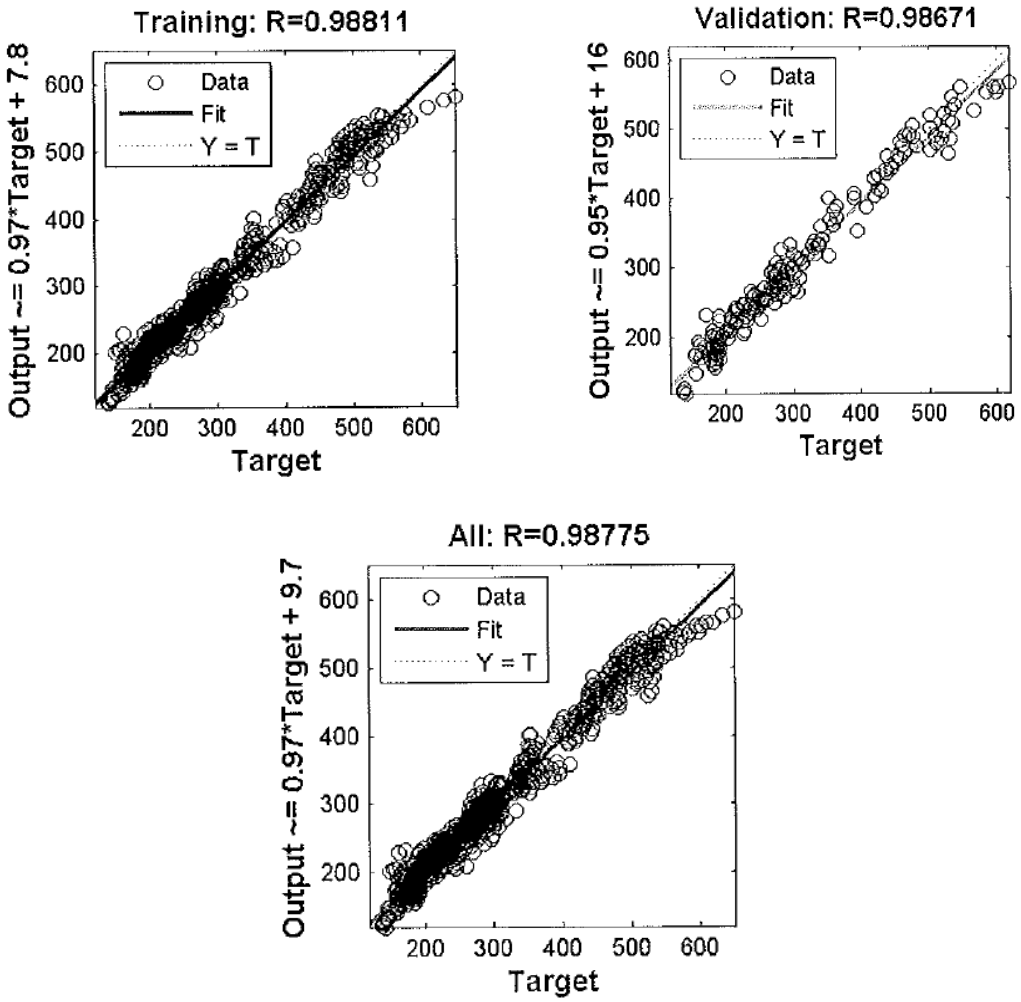


**Figure 6.17 Comparison of Tensile Strain at the Bottom of the Asphalt Concrete**

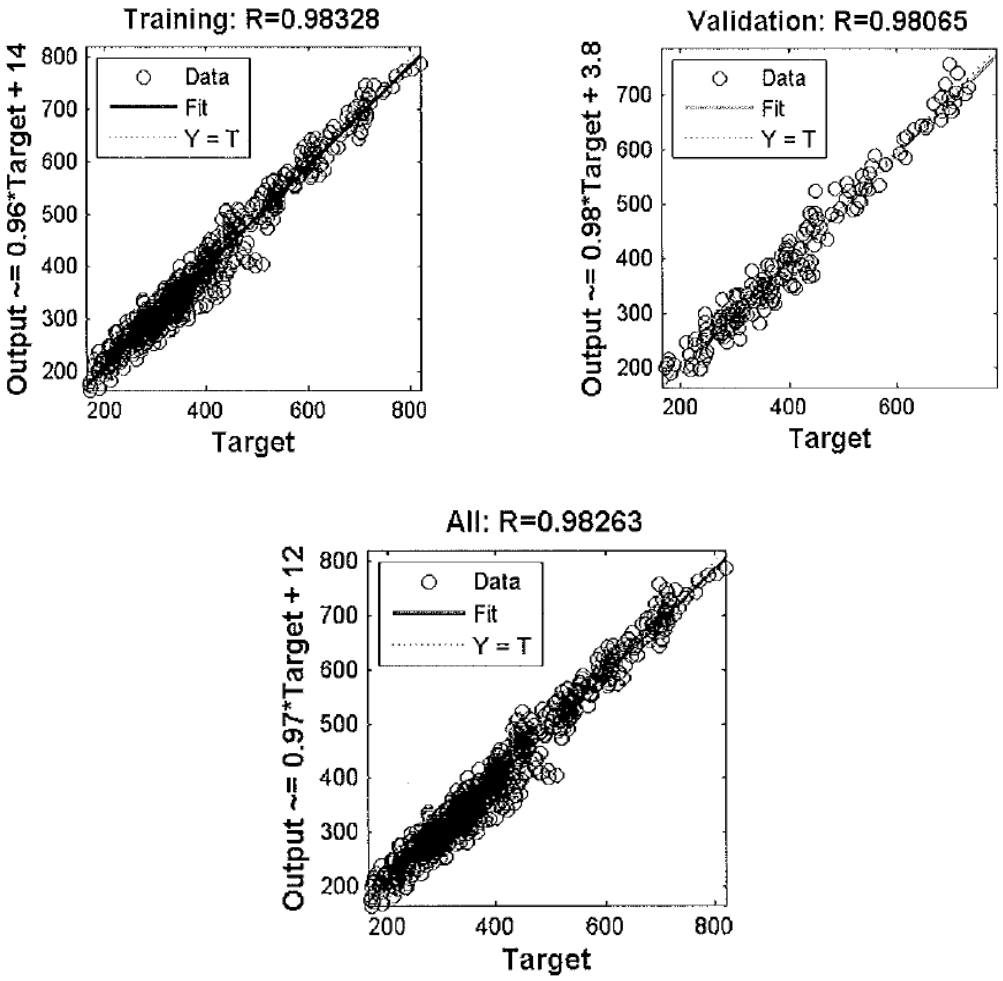


**Figure 6.18 Comparison of Average Vertical Strain in the Asphalt Concrete**

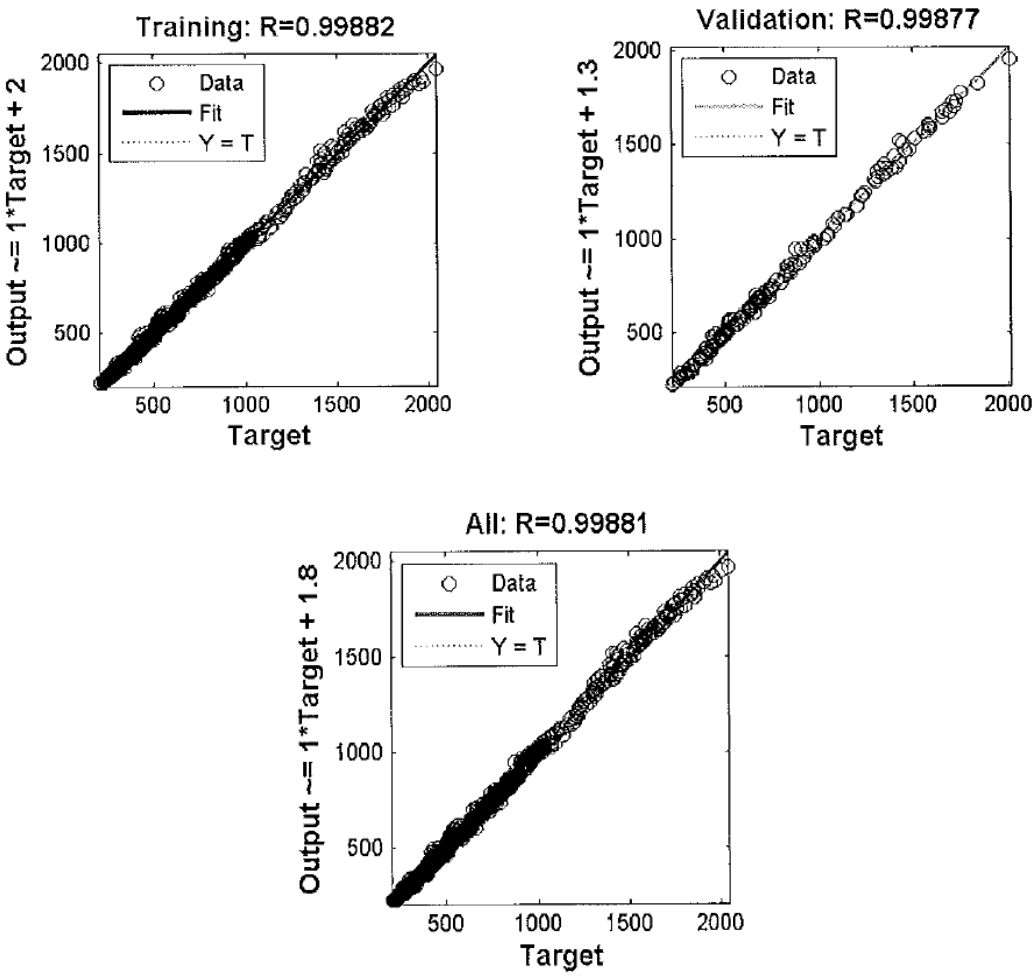


**Figure 6.19 Comparison of Average Vertical Strain in the Base Layer**

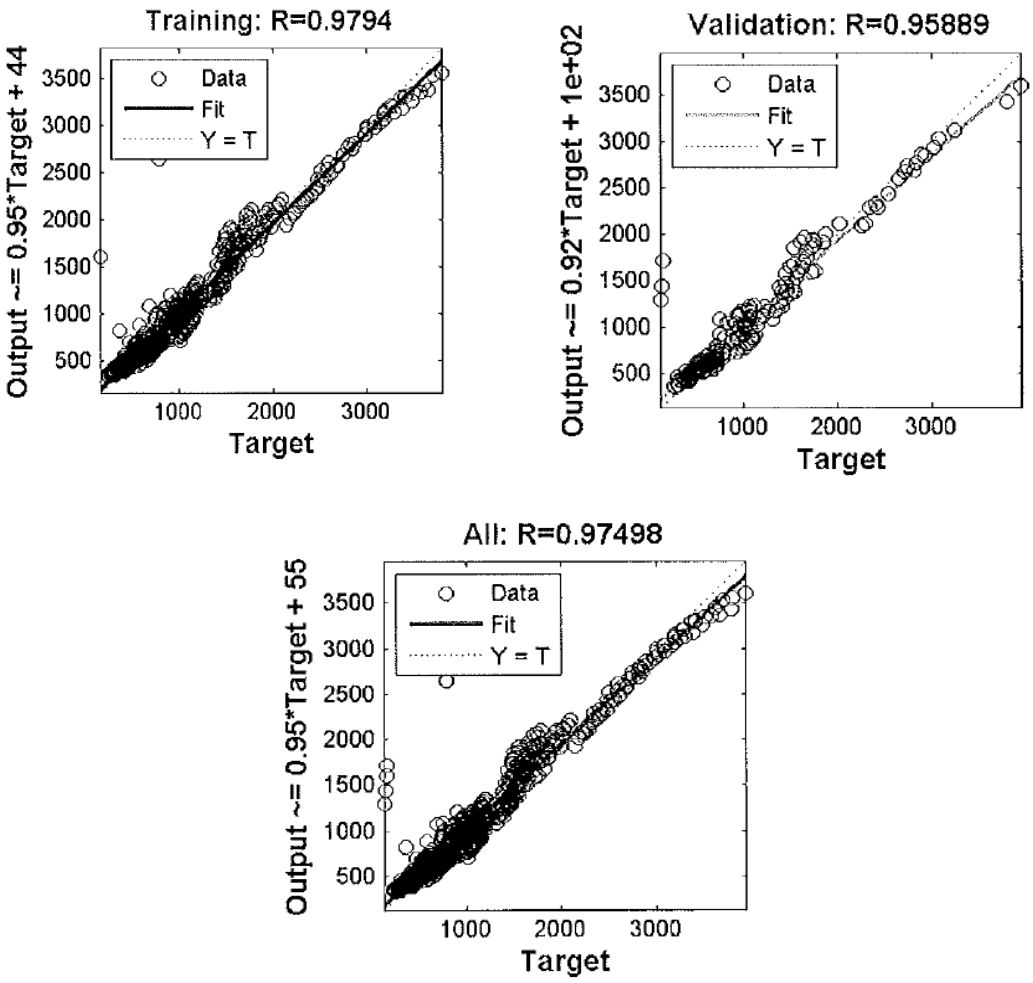


**Figure 6.20 Comparison of Vertical Strain at the Top of the Subgrade**

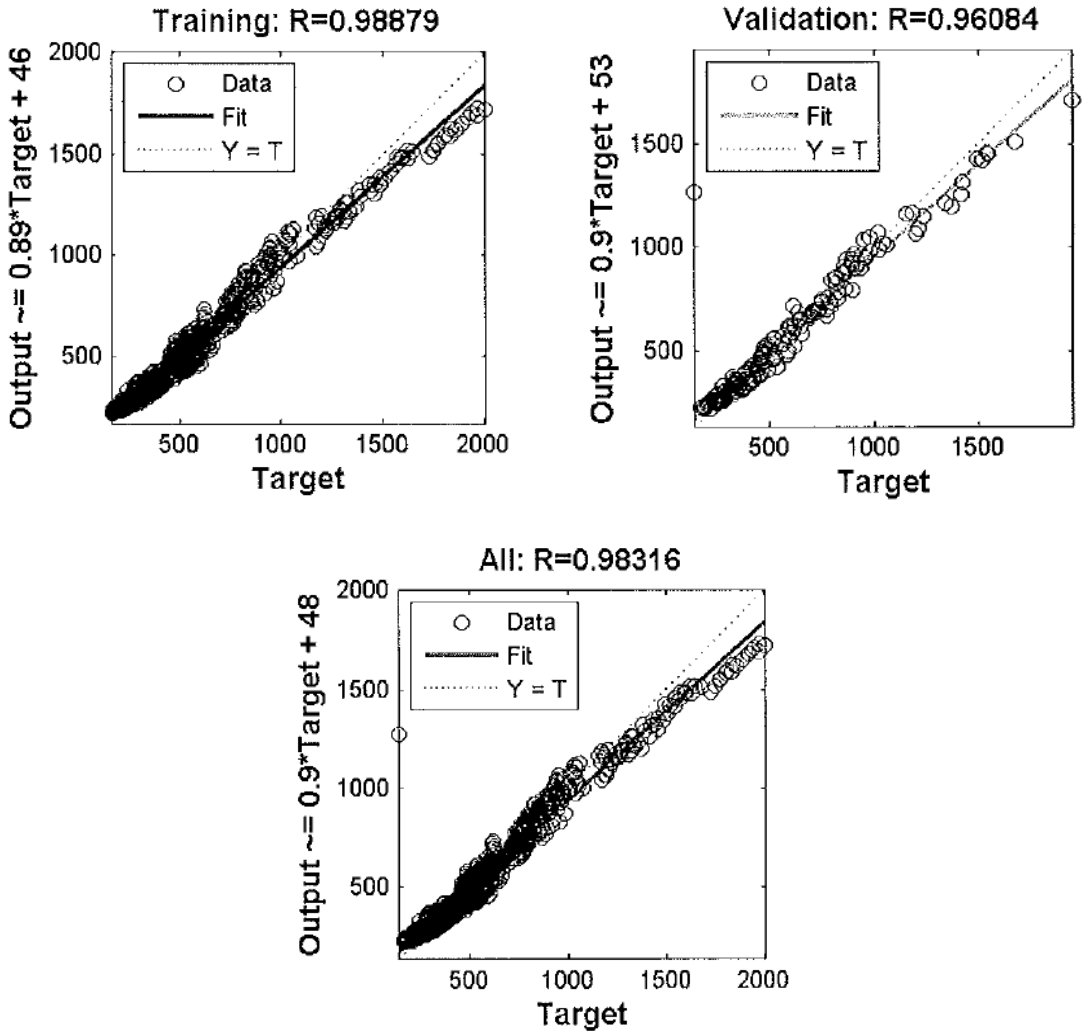


**Figure 6.21 Comparison of Vertical Strain at 15 cm below the Top of the Subgrade**

# 7. CONCLUSIONS AND RECOMMENDATIONS

## 7.1 Conclusions

This study proposes a comprehensive methodology to characterize the moisture-sensitive and stress-dependent nonlinear cross-anisotropic behavior of unbound granular material (UGM). The newly developed constitutive model considers both the stress dependence and moisture dependence of the resilient modulus of UGM. The degree of saturation and the matric suction are incorporated in this model to discriminate the effect of the moisture variations. The repeated load triaxial test is used to measure the resilient moduli of the selected base materials at different moisture contents. The moisture dependence of the developed model is validated by comparing the model-predicted resilient moduli to those measured from the tests. Compared with the Pavement ME Design model, the proposed model is more accurate to characterize the moisture dependence of UGM. It is shown that the matric suction of the UGM is a key element to reflect the moisture dependence of the resilient modulus.

One finite element model has been developed to predict the responses of the pavement structures when they are subjected to the specified traffic loads. In this finite element model, a user-defined material (UMAT) subroutine is programmed to take into account the moisture-sensitive and stress-dependent nonlinear cross-anisotropic behavior of base material. The UMAT subroutine adopts the secant stiffness approach with the multiple damping factors. The line search technique is employed to make the numerical computation converge. The developed UMAT subroutine is verified using the simulated triaxial test. At a specified stress state, the modulus and strain of the UGM predicted by

the finite element model with the developed UMAT subroutine is close to the analytical solutions. To investigate the influence of the moisture content of base material on pavement response, three moisture conditions are simulated in the finite element model, which includes the dry condition, the optimum moisture condition, and the moist condition. It is shown that the modulus of base material is sensitive to the moisture condition. The moduli of base material at the dry condition are nearly twice as large as those of base material at the moist condition. This variation further results in the change of pavement responses, such as the surface deflection, the tensile strain at the bottom of asphalt concrete, and the compressive strain in base course and subgrade. The computational results indicate that the model-predicted surface deflections, tensile strain at the bottom of asphalt concrete and compressive strains in base course are significantly sensitive to the moisture condition in base course, while the model-predicted compressive strain at the top of subgrade is slightly affected by the moisture variation in base course. The numerical simulations also demonstrate that increasing the moisture content of base course increases the surface deflections, the tensile strains at the bottom of asphalt concrete, and the compressive strains in base and subgrade.

Rutting or accumulated permanent deformation (PD) is the primary distress for unbound granular bases in flexible pavements. This study proposes a new mechanistic-empirical rutting (MER) model to evaluate the PD behavior of UGM. The new MER model considers the stress dependence of PD behavior of UGM by incorporating the two terms, $\sqrt{J_2}$ and $\alpha I_1 + K$ into the Tseng-Lytton model. This modification is based on the

concept of Drucker-Prager plastic yield criterion, which considers $\sqrt{J_2}$ as a softening term and $\alpha I_1 + K$ as a hardening term for UGMs.

A new PD test protocol is developed to determine the MER model coefficients and validate the MER model accuracy. The proposed test protocol includes 7 stress states used to determine the model coefficients and 2 stress states to validate the model prediction accuracy. Based on the PD test results, the correlations of $I_1$ and $J_2$ with the accumulated permanent strain at 10,000 load cycles are fitted by the power models with 0.97~0.99 R-Squared values. Laboratory-measured and model-predicted accumulated permanent strain curves are compared in this study. It is shown that the proposed MER model accurately fits the permanent strain curves of the UGMs in all load periods. The prediction accuracy of the model is validated by comparing the predicted permanent strain curves with the laboratory measurements at different stress states other than those used for determining the model coefficients. The comparison results indicate that the proposed MER model is capable of accurately characterizing the stress dependence of the rutting behavior for UGM.

The sensitivity analysis is also performed to evaluate the effect of cohesion and friction angle on the PD behavior. It is shown that a higher cohesion yields less accumulated PD, and the increasing of friction angle also reduces the accumulated permanent strain. Through the cohesion and stress terms embedded in the model, the proposed MER model has a potential to evaluate the moisture-sensitivity of the PD behavior of the UGMs. The new model is successfully implemented to predict the rut depth of a flexible pavement. The computed rut depth by the new model is always higher

than that predicted by MEPDG model. This is consistent with the laboratory observations that the MEPDG model underestimates the permanent deformation of tested materials. Both the MER model and MEPDG model exhibit the same trend that, when increasing load magnitude or decreasing base modulus, more rut depth is accumulated in the base layer. It is seen that the MER model is more sensitive than the MEPDG model in terms of predicting the rutting performance of the base layer when the load magnitude and base modulus change.

This study also presents the results of a wide variety of tests to determine the properties of a variety of Texas base courses as they relate to performance. Repeated loading is applied to all base materials at different levels of confining pressure and deviatoric pressures. The resilient moduli and permanent deformation properties are measured directly. Other indicator tests are made on the same materials to determine how well they are correlated to these performance-related properties. These tests include the methylene blue test developed by the W.R. Grace Corporation, the percent fines content test using the Horiba particle size analyzer, the filter paper test to measure the soil suction, the gradation sieve analysis, and the aggregate imaging system test to measure the shape, angularity and texture of the coarse aggregate particles.

The multiple regression analysis is performed to develop the prediction models for the resilient moduli and PD properties using these performance-related base course properties. The dry density, shape, angularity and texture of the coarse aggregates, and the percent fines content and the methylene blue value are proven to be significant variables in the prediction models. The proposed performance-related base course

properties are accurate, repeatable and reliable. The tests needed to determine these performance-related base course properties are simple and efficient than the repeated load triaxial test. The developed prediction models for the resilient moduli and PD properties have high R-squared values, which indicates the developed models are accurate to predict the resilient moduli and PD of granular materials.

After characterizing the elastic and plastic behaviors of UGM, this study evaluates the influence of geogrid on the performance of flexible pavements. Geogrids are widely used by highway agencies in unbound base layers for enhancing the performance of flexible pavements. The repeated load triaxial test is used to evaluate the impact of geogrid on the cross-anisotropic and stress dependent permanent deformation characteristics of UGMs. It is found that the effect of geogrid reinforcement on cross-anisotropic and permanent deformation characteristics of UGM is influenced by the aperture type, the sheet stiffness and the location of the geogrid. The cross-anisotropy test results indicate that placing the geogrid in the middle or at one-quarter below the middle of specimen reinforces both the vertical and horizontal resilient moduli, and significantly reduces the permanent deformation of UGM. The inclusion of geogrid does not influence the anisotropic ratio of UGM. It is also demonstrated that the geogrid is more effective in reinforcing the horizontal and vertical modulus of UGM when the reinforced specimen is subjected to the low or medium stress levels. The effect of geogrid reinforcement is not significant in reducing the permanent deformation of UGM until the deviatoric shear stress reaches a threshold level. The MER model is successfully applied to evaluate the permanent deformation properties of geogrid-

reinforced granular material. The determined model coefficients can be used to predict the permanent deformation of the geogrid-reinforced UGMs at any stress levels and numbers of load repetitions.

Geogrids reinforce the granular materials through two major mechanisms: lateral confinement to reinforce the UGM in the vicinity of the geogrid, and the membrane effect to reduce the vertical stresses in base and subgrade. The finite element models are developed to simulate the geogrid-reinforced pavement structures by taking into account these two mechanisms, and to evaluate the effect of material and geometric factors on the performance of geogrid-reinforced pavements.

In the finite element model, the lateral confinement is equivalent to an increase of horizontal and vertical moduli of UGM in the geogrid influence zone. The membrane effect is simulated by defining the geogrid as a membrane element, and characterizing the geogrid-aggregates/soils interface interaction using the Goodman model. To validate the developed finite element model, the large-scale Soil Tank test is conducted to measure the responses of geogrid-reinforced and unreinforced pavement structures. The Soil Tank test measurements include the surface deflections, the tensile strain at the bottom of asphalt concrete, and the vertical and horizontal pressures at a variety of locations in base and subgrade. The predicted pavement responses from the finite element models are comprehensively compared to these measurements. The comparison results indicate that the finite element simulation results are in good agreement with the Soil Tank test measurements for both the reinforced and unreinforced pavement structures. The considerations of the paving material characterization, the geogrid-

aggregate/soil interface characterization, and the reinforcement influence zone are important to develop accurate numerical models of geogrid-reinforced pavement structures.

The developed geogrid-reinforced pavement models are also able to quantify the effect of layer thickness, layer modulus, sheet stiffness of geogrid, and geogrid location on pavement responses. The finite element modeling technique provides a sound basis for predicting the performance of geogrid-reinforced pavements. Using this approach, a large database of critical pavement responses is established for a wide range of geogrid-reinforced pavement structures. The established database of geogrid-reinforced pavement responses is used to train and validate the artificial neural network (ANN) models. The developed ANN models are used to predict the responses of geogrid-reinforced pavement structures for any given layer thickness and material properties. The predicted pavement responses can be input into the Pavement ME Design distress models to calculate the pavement performance, such as the fatigue cracking, rutting and international roughness index. This methodology is compatible with the current Pavement ME Design framework, which facilitates the incorporation into the Pavement ME Design software.

## 7.2 Recommendations for Future Research

This study focuses on the characterization and performance prediction of unbound granular bases with and without geogrid reinforcement. Constitutive models have been developed to characterize the elastic and plastic behavior of granular material

with and without geogrid. These models are implemented to predict the pavement performance based on the finite element approach. The developed finite element models for unreinforced and geogrid-reinforced pavements have been validated by comparing the model-predicted responses with the measurements from the large-scale Soil Tank test. To make this research work more practical, the following studies are recommended as continuations of this study.

The current Pavement ME Design and the AASHTO Mechanistic-Empirical Pavement Design Guide Manual of Practice (MEPDG) considers the granular base as a nonlinear stress dependent material. The moisture sensitivity of the resilient modulus of granular base is empirically attributed to the variation of degree of saturation. This study found that the moisture sensitivity of resilient modulus is affected by the change of the matric suction. Additionally, the Pavement ME Design ignores the cross-anisotropy of base course, which results in the underestimate of the pavement performance. The proposed moisture-sensitive and stress-dependent nonlinear cross-anisotropic constitutive model should be incorporated into the Pavement ME Design software. Similarly, the new mechanistic-empirical rutting model is proved to be more accurate than Pavement ME Design model to predict the stress-dependent permanent deformation behavior of granular base. It is also suggested to incorporate this mechanistic-empirical rutting model to the current Pavement ME Design software.

Regarding the studies of geogrid-reinforced granular base, the proposed methodology to quantify the influence of geogrid on pavement performance is

compatible with the current Pavement ME Design, which should be ready for incorporating into the software.

The framework of this study is validated by using the large-scale Soil Tank test data. Before implementing it to the Pavement ME Design, more validation and calibration work should be conducted using the data available from in-service pavements or full-scale accelerated pavement tests.

This study develops the regression models to predict the resilient modulus and permanent deformation properties of granular base. One limitation of these prediction models is the tested base materials are only from Texas. To extend the applicability of the prediction models, more base materials should be collected from all over the world. If the database of these material properties are large enough, the neural network model approach is recommended to predict the resilient modulus and permanent deformation properties of granular base.

## REFERENCES


AASHTO (2007). Standard Method of Test for the Qualitative Detection of Harmful Clays of the Smectite Group in Aggregates Using Methylene Blue. *AASHTO T330-07,* American Association of State Highway and Transportation Officials, Washington, DC.

AASHTO (2008). "Mechanistic-Empirical Pavement Design Guide: A Manual of Practice." *AASHTO Designation: MEPDG-1*. Washington, DC.

ABAQUS. (2010). ABAQUS Standard User's Manual. Providence, Rhode Island.

Abu-Farsakh, M. Y., Nazzal, M. D., and Mohammad, L. N. (2007). "Effect of Reinforcement on Resilient and Permanent Deformations of Base Course Material." *Transportation Research Record: Journal of Transportation Research Board*, No. 2004, 2007, pp. 120-131.

Abu-Farsakh, M., Souci, G., Voyiadjis, G., and Chen, Q. (2012). "Evaluation of Factors Affecting the Performance of Geogrid-Reinforced Granular Base Material Using Repeated Load Triaxial Tests." *Journal of Materials in Civil Engineering*, Vol. 24, No. 1, pp. 72-83.

Adu-Osei, A., Little, D. N., Lytton, R. L. (2001). "Cross-Anisotropic Characterization of Unbound Granular Materials." *Transportation Research Record: Journal of the Transportation Research Board,* No. 1757, pp. 82-91.

Al-Qadi, I. L., Wang, H., and Tutumluer, E. (2010). "Dynamic Analysis of Thin Asphalt Pavements by Using Cross-Anisotropic Stress-Dependent Properties for Granular Layer." *Transportation Research Record: Journal of the Transportation Research Board*, No. 2154, pp. 156-163.

Al-Qadi, I. L., Brandon, T. L., Valentine, R. J., Lacina, B. A., and Smith, T. E. (1994). "Laboratory Evaluation of Geosynthetic-Reinforced Pavement Sections." *Transportation Research Record: Journal of Transportation Research Board*, No. 1439, pp. 25-31.

Al-Qadi, I. L., Dessouky, S. H., Kwon, J., and Tutumluer, E. (2008). "Geogrids in Flexible Pavements: Validated Mechanisms." *Transportation Research Record: Journal of the Transportation Research Board*, No. 2045, pp. 102-109.

Amari, S. (1998). "Natural Gradient Works Efficiently in Learning." *Neural Computation*, Vol. 10, No. 2, pp. 251-276.

Andrei, D., Witczak, M. W., Schwartz, C. W., and Uzan, J. (2004). "Harmonized Resilient Modulus Test Method for Unbound Pavement Materials." *Transportation Research Record: Journal of the Transportation Research Board*, No. 1874, pp. 29-37.

Ashtiani R, Little D. N, and Masad E. A. (2008). "Material Factors that Influence Anisotropic Behavior of Aggregate Bases." *Transportation Research Record: Journal of the Transportation Research Board,* No. 2059, pp. 20-30.

Ashtiani, R. (2009). Anisotropic Characterization and Performance Prediction of Chemically and Hydraulically Bounded Pavement Foundations. Ph.D. Dissertation, Texas A&M University, College Station, Texas.

ASTM. (2008). Standard Guide for Identification, Storage, and Handling of Geosynthetic Rolls and Samples. *ASTM D 4873-02,* American Society for Testing and Materials (ASTM), West Conshohocken, Pennsylvania.

ASTM (2010). Standard Test Method for Measurement of Soil Potential (Suction) Using Filter Paper. *ASTM D5298-10*, American Society for Testing and Materials (ASTM), West Conshohocken, Pennsylvania.

ASTM (2012). Standard Test Methods for Laboratory Compaction Characteristics of Soil Using Modified Effort. *ASTM D1557-12*, American Society for Testing and Materials (ASTM), West Conshohocken, Pennsylvania.

Barksdale, R. D., and Brown, S. F. (1988). "Potential Benefits of Geosynthetics in Flexible Pavements." *Final report, No. E-20-672*. National Cooperative Highway Research Program, National Research Council, Washington D.C., 626p.

Barksdale R, and Itani S. (1994). "Influence of Aggregate Shape on Base Behavior." *Transportation Research Record: Journal of the Transportation Research Board,* No. 1227, pp. 171-182.

Berg, R.R., Christopher, B.R. and Perkins, S.W. (2000). "Geosynthetic Reinforcement of the Aggregate Base/Subbase Courses of Flexible Pavement Structures-*GMA White Paper II*, Geosynthetic Materials Association, Roseville, MN, USA, 176p.

Cary, C., and Zapata, C. (2011). "Resilient Modulus for Unsaturated Unbound Materials." *Road Materials and Pavement Design*, Vol. 12, No.3, pp. 615-638.

Ceylan, H., Bayrak, M. B., and Gopalakrishnan, K. (2014). "Neural Networks Applications in Pavement Engineering: A Recent Survey." *International Journal of Pavement Research and Technology*, Vol. 7, No. 6, pp. 434-444.

Chan, F., Barksdale R., and Brown, S. (1989). "Aggregate Base Reinforcement of Surfaced Pavements," *Geotextile and Geomembranes,* Vol. 8, No. 3, pp. 165–189.

Chazallon, C., Hornych, P., and Mouhoubi, S. (2006). "Elastoplastic Model for the Long-Term Behavior Modeling of Unbound Granular Materials in Flexible Pavements." *International Journal of Geomechanics,* Vol. 6, No. 4, pp. 279-289.

Chen, C., Ge, L., and Zhang, J. (2010). "Modeling Permanent Deformation of Unbound Granular Materials under Repeated Loads." *International Journal of Geomechanics,* Vol. 10, No. 6, pp. 236-241.

Chow, L. (2014). Permanent Deformation Behavior of Unbound Granular Materials and Rutting Model Development. Master Thesis, University of Illinois at Urbana-Champaign, Urbana, Illinois.

Chow, L., Mishra, D., and Tutumluer, E. (2014). "Framework for Development of an Improved Unbound Aggregate Base Rutting Model for Mechanistic-Empirical Pavement Design." *Transportation Research Record: Journal of the Transportation Research Board,* No. 2401, pp. 11-21.

Demuth, H., and Beale, M. (1998). Neural Network Toolbox for Use with MATLAB. The MathWorks, Natick, Massachusetts.

Desai, C.S. (1980). "A General Basis for Yield, Failure and Potential Function in Plasticity." *International Journal of Numerical and Analytical Methods in Geomechanics,* Vol. 4, pp. 361-375.

Desai, C.S., and Faruque, M.O. (1984). "Constitutive Model for Geologic Materials." *Journal of the Engineering Mechanics Division*, ASCE, Vol. 110, No. 9, pp. 1391-1408.

Drucker, D.C., and Prager, W. (1952). "Soil Mechanics and Plastic Analysis for Limit Design." *Quarterly of Applied Mathematics,* Vol. 10, No. 2, pp. 157-165.

Erlingsson, S., and Rahman, M. (2013). "Evaluation of Permanent Deformation Characteristics of Unbound Granular Materials by Means of Multistage Repeated-Load Triaxial Tests." *Transportation Research Record: Journal of the Transportation Research Board*, No. 2369, pp. 11-19.

Epps, J., Sebesta, S., Hewes, B., Sahin, H., Luo, R., Button, J., Lytton, R., Herrera, C., Hatcher, R., and Gu, F. (2014). "Development of a specification for flexible base construction." Final Report, *No. FHWA/TX-13/0-6621*, 414p.

Fredlund, D. G., and Xing, A. (1994). "Equations for the Soil-Water Characteristic Curve." *Canadian Geotechnical Journal*, Vol. 31, pp. 521-532.

Gabr, A., and Cameron, D. (2013). "Permanent Strain Modeling of Recycled Concrete Aggregate for Unbound Pavement Construction." *Journal of Materials in Civil Engineering,* Vol. 25, No. 10, pp. 1394-1402.

Gauch, H. G., Hwang, J. T., Fick, G. W. (2003). "Model Evaluation by Comparison of Model-Based Predictions and Measured Values." *Agronomy Journal*, No. 95, pp. 1442-1446.

Giroud, J.P. and Noiray, L. (1981). "Geotextile-Reinforced Unpaved Roads." *Journal of Geotechnical Engineering Division*, ASCE, Vol. 107, No.9, pp. 1233 – 1254.

Giroud, J.P. and Han, J. (2004). "Design Method for Geogrid-Reinforced Unpaved Roads-I." *Journal of Geotechnical Engineering*, ASCE, Vol. 130, No.8, pp. 775 - 786.

Goodman, R. E., Taylor, R. L., Brekke, T. L. (1968). "A Model for the Mechanics of Jointed Rock." *Journal of Soil Mechanics and Foundation Division, ASCE*, Vol. 94, No. SM3, pp. 637-659.

Gu, F., Sahin, H., Luo, X., Luo, R., and Lytton, R. L. (2015). "Estimation of Resilient Modulus of Unbound Aggregates Using Performance-Related Base Course Properties." *Journal of Materials in Civil Engineering*, Vol. 27, No. 6, 04014188.

Haas R., Walls, J. and Carroll, R.G. (1988). "Geogrid Reinforcement of Granular Bases in Flexible Pavements." *Transportation Research Record: Journal of the Transportation Research Board*, No. 1188, pp. 19-27.

Heath A. C., Pestana, J. M., Harvey, J. T., and Bejerano, M. O. (2004). "Normalizing Behavior of Unsaturated Granular Pavement Materials." *Journal of Geotechnical and Geoenvironmental Engineering*, Vol. 130, pp. 896-904.

Hjelmstad, K., and Taciroglu, E. (2000). "Analysis and Implementation of Resilient Modulus Models for Granular Solids." *Journal of Engineering Mechanics*, Vol. 126, No.8, pp. 821-830.

Huang, Y. H. (1993). *Pavement analysis and design.* Prentice-Hall, Englewood Cliffs, NJ.

Kenis, W.J. (1977). "Predictive Design Procedures, VESYS User's Manual." Final Report, *No. FHWA-RD-77-154*, Federal Highway Administration, Mclean, VA.

Kim, M., Tutumluer. E., and Kwon, J. (2009). "Nonlinear Pavement Foundation Modeling for Three-Dimensional Finite-Element Analysis of Flexible Pavements." *International Journal of Geomechanics*, Vol. 9, No.5, pp. 195-208.

Korkiala-Tanttu, L. (2009). "Verification of Rutting Calculation for Unbound Road Materials." *Proceedings of the Institution of Civil Engineers, Transport* 162, 162(TR2), pp. 107-114.

Kwon, J. (2007). Development of a Mechanistic Model for Geogrid Reinforced Flexible Pavements. Ph.D. Dissertation. University of Illinois at Urbana-Champaign, Urbana, Illinois.

Kwon, J., and Tutumluer, E. (2009). "Geogrid Base Reinforcement with Aggregate Interlock and Modeling of Associated Stiffness Enhancement in Mechanistic Pavement Analysis." *Transportation Research Record: Journal of the Transportation Research Board,* No. 2116, pp. 85 – 95.

Lekarp, F., Isacsson, U., and Dawson, A. (2000a). "State of the Art: Resilient response of unbound aggregates." *Journal of Transportation Engineering*, Vol. 126, No.1, pp. 66-75.

Lekarp, F., Isacsson, U., and Dawson, A. (2000b). "State of the Art. II: Permanent Strain Response of Unbound Aggregates." *Journal of Transportation Engineering,* Vol. 126, No. 1, pp. 76-83.

Luo, R. (2007). Minimizing longitudinal pavement cracking due to subgrade shrinkage. Ph.D. dissertation, The University of Texas at Austin, Austin, Texas.

Liang, R. Y., Rabab'ah, S., and Khasawneh, M. (2008). "Predicting Moisture-Dependent Resilient Modulus of Cohesive Soils Using Soil Suction Concept." *Journal of Transportation Engineering*, Vol. 134, No.1, pp. 34-40.

Lytton, R. L. (1995). "Foundations and pavements on unsaturated soils." Keynote Address, *Proceedings, First International Conference on Unsaturated Soils*, International Society of Soil Mechanics and Foundation Engineering, Paris, pp. 1201-1220.

Lytton, R. L., Uzan, J., Fernando, E. G., Roque, R., Hiltunen, D., and Stoffels, S. M. (1993). "Development and Validation of Performance Prediction Models and Specifications for Asphalt Binders and Paving Mixtures." *Report No. SHRP-A-357,* Strategic Highway Research Program, National Research Council, Washington, D. C.

Masad, E. A. (2005). "Aggregate Imaging System (AIMS): Basics and Applications." *Final Report, No. FHWA/TX-05/5-1707-01-1*, 58pp.

Matsuoka, H., and Nakai, T. (1985). "Relationship among Tresca, Mises, Mohr-Coulomb and Matsuoka-Nakai Failure Criterion." *Soils and Foundations,* Vol. 25, No. 4, pp. 123-128.

McDowell, G. R., Harireche, O., Konietzky, H., Brown, S. F., and Thom, N. H. (2006). "Discrete Element Modelling of Geogrid-Reinforced Aggregates." *Proceedings of the Institution of Civil Engineers-Geotechnical Engineering*, Vol. 159, No. 1, pp 35-48.

Mishara D, and Tutumluer E. (2012). "Aggregate Physical Properties Affecting Modulus and Deformation Characteristics of Unsurfaced Pavements." *Journal of Materials in Civil Engineering,* Vol. 24, pp. 1144-1152.

Moghaddas-Nejad, F., and Small, J. (2003). "Resilient and Permanent Characteristics of Reinforced Granular Material by Repeated Load Triaxial Tests." *Geotechnical Testing Journal,* Vol. 26, No. 2, pp. 152-166.

Montgomery DC, and Runger GC. (2007). *Applied Statistics and Probability for Engineers.* John Wiley & Sons, New York.

More, J. (1978). "The Levenberg-Marquardt Algorithm: Implementation and Theory." *Numerical Analysis*, Vol. 630, pp. 105-116

Nazzal, M., Abu-Farsakh, M., and Mohammad, L. (2007). "Laboratory Characterization of Reinforced Crushed Limestone under Monotonic and Cyclic Loading." *Journal of Materials in Civil Engineering,* Vol. 19, No. 9, pp. 772-783.

Nazzal, M. D., and Mohammad, L. N. (2010). "Estimation of Resilient Modulus of Subgrade Soils for Design of Pavement Structures." *Journal of Materials in Civil Engineering*, Vol. 22, pp. 726-734.

NCHRP (2003). "Harmonized test methods for laboratory determination of resilient modulus for flexible pavement design." *Final Report. No. 1-28A,* National Cooperative Highway Research Program (NCHRP), Washington, D. C.

Oh. J., Lytton, R., and Fernando, E. (2006). "Modeling of Pavement Response Using Nonlinear Cross-Anisotropy Approach." *Journal of Transportation Engineering*, Vol. 132, No. 6, pp. 458-468.

Pan, T., Tutumluer, E., and Anochie-Boateng, J. (2006). "Aggregate Morphology Affecting Resilient Behavior of Unbound Granular Materials." *Transportation*

*Research Record: Journal of the Transportation Research Board,* No. 1952, pp. 12-20.

Perkins, S.W., and Ismeik, M. (1997a). "A Synthesis and Evaluation of Geosynthetic-Reinforced Base Course Layers in Flexible Pavements: Part I Experimental work." *Geosynthetics International*, Vol. 4, No. 6, pp. 549-604.

Perkins, S.W., and Ismeik, M. (1997b). "A Synthesis and Evaluation of Geosynthetic-Reinforced Base Course Layers in Flexible Pavements: Part II - Analytical Work." *Geosynthetics International*, Vol. 4, No. 6, pp. 605 – 621.

Perkins, S. W. (2001). "Numerical Modeling of Geosynthetic Reinforced Flexible Pavements." *Final Report, No. FHWA/MT-01-003/99160-2*, Federal Highway Administration, Washington, D.C., 112p.

Perkins, S. W., and Edens, M. Q. (2003). "A Design Model for Geosynthetic-Reinforced Pavements." *International Journal of Pavement Engineering*, Vol. 4, No. 1, pp. 37-50.

Perkins, S. W. (2004). "Development of Design Methods for Geosynthetic-Reinforced Flexible Pavements." *Report No. DTFH61-01-X-00068*, U.S. Department of Transportation, Federal Highway Administration, Washington, D. C., 263p.

Prozzi, J. A., and Luo, R. (2007). "Using Geogrids to Minimize Reflective Longitudinal Cracking on Pavements over Shrinking Subgrades." *Transportation Research Record: Journal of the Transportation Research Board*, No. 2004, pp. 99-110.

Rahman, M., Arulrajah, A., Piratheepan, J., Bo, M., and Imteaz, M. "Resilient Modulus and Permanent Deformation Responses of Geogrid-Reinforced Construction and Demolition Materials." *Journal of Materials in Civil Engineering*, Vol. 26, No. 3, 2014, pp. 512-519.

Saad, B., Mitri, H., and Poorooshasb, H. (2006). "3D FE Analysis of Flexible Pavement with Geosynthetic Reinforcement." *Journal of Transportation Engineering*, Vol. 132, No. 5, pp. 402-415.

Saevarsdottir, T., and Erlingsson, S. (2013). "Water Impact on The Behavior of Flexible Pavement Structures in An Accelerated Test." *Road Materials and Pavement Design*, Vol. 14, No.2, pp. 256-277.

Sahin H. (2011). "Characterization of Expansive Soil for Retaining Wall Design." M.S. Thesis, Texas A&M University, College Station, Texas.

Sahin, H., Gu, F., and Lytton, R. L. (2015). "Development of Soil-Water Characteristic Curve for Flexible Base Materials Using the Methylene Blue Test." *Journal of Materials in Civil Engineering*, Vol. 27, No.5, 04014175.

Salour, F., and Erlingsson, S. (2013). "Investigation of A Pavement Structural Behavior during Spring Thaw Using Falling Weight Deflectometer." *Road Materials and Pavement Design,* Vol. 14, No. 1, pp. 141-158.

Schuettpelz, C., Fratta, D., and Edil, T.B. (2009). "Evaluation of the Zone of Influence and Stiffness Improvement from Geogrid Reinforcement in Granular Materials." *Transportation Research Record: Journal of the Transportation Research Board*, No. 2116, 76-84.

Theyse, H. L. (2002). "Stiffness, Strength, and Performance of Unbound Aggregate Materials: Application of South African HVS and Laboratory Results to California Flexible Pavements." *Technical Report*, University of California Pavement Research Center, 86p.

Tseng, K. H., and Lytton, R. L. (1989). "Prediction of Permanent Deformation in Flexible Pavements Materials, Implication of Aggregates in the Design, Construction, and Performance of Flexible Pavements." *ASTM STP 1016,* American Society for Testing and Materials (ASTM), pp. 154-172, West Conshohocken, Pennsylvania.

Tutumluer, E. (1995). Predicting Behavior of Flexible Pavements with Granular Bases. Ph.D. Dissertation, Georgia Institute of Technology, Atlanta, Georgia.

Tutumluer, E., and Thompson, M. R. (1997). "Anisotropic Modeling of Granular Bases in Flexible Pavements." *Transportation Research Record: Journal of the Transportation Research Board*, No. 1577, pp. 18-26.

Tutumluer, E., and Seyhan, U. (1999). "Laboratory Determination of Anisotropic Aggregate Resilient Moduli Using an Innovative Test Device." *Transportation Research Record: Journal of the Transportation Research Board*, No. 1687, pp. 13-21.

Tutumluer, E., Little, D. N., and Kim, S. H. (2003). "Validated Model for Predicting Field Performance of Aggregate Base Courses." *Transportation Research Record: Journal of the Transportation Research Board*, No. 1837, pp. 41-49.

Tutumluer E, and Pan T. (2008). "Aggregate Morphology Affecting Strength and Permanent Deformation Behavior of Unbound Aggregate Materials." *Journal of Materials in Civil Engineering,* Vol. 20l, pp. 617-627.

Tutumluer, E. (2013). “Practices for Unbound Aggregate Pavement Layers.” *NCHRP Synthesis 445*, Transportation Research Board, National Research Council, Washington, D.C. 180p.

TxDOT (2010). “Test Procedure for Triaxial Compression for Disturbed Soils and Base Materials”, *TEX-117-E*, Texas Department of Transportation, Austin, Texas.

Uzan, J. (1985). “Characterization of Granular Material.” *Transportation Research Record: Journal of the Transportation Research Board,* No. 1022, pp. 52-59.

Uzan, J. (1999). “Permanent Deformation of A Granular Base Material.” *Transportation Research Record: Journal of the Transportation Research Board,* No. 1673, pp. 89-94.

Vermeer, P.A. (1982). “A Five-Constant Model Unifying Well-Established Concepts.” *Proceedings of International Workshop on Constitutive Relations for Soils,* Grenoble, France, pp. 175-197.

Wang, H., and Al-Qadi, I. L. (2013). “Importance of Nonlinear Anisotropic Modeling of Granular Base for Predicting Maximum Viscoelastic Pavement Responses under Moving Vehicular Loading.” *Journal of Engineering Mechanics*, Vol. 139, No.1, pp. 29-38.

Wathugala, G. W., Huang, B., and Pal, S. (1996). "Numerical Simulation of Geosynthetic-Reinforced Flexible Pavements." *Transportation Research Record: Journal of the Transportation Research Board*, No. 1534, pp. 58-65.

Wayne, M., Boudreau, R. L., and Kwon, J. (2011). “Characterization of Mechanically Stabilized Layer by Resilient Modulus and Permanent Deformation Testing.” *Transportation Research Record: Journal of the Transportation Research Board*, No. 2204, pp. 76-82.

Wu, Z., Hu, S., and Zhou, F. (2014). “Prediction of Stress Intensity Factors in Pavement Cracking with Neural Networks Based on Semi-Analytical FEA.” *Expert Systems with Applications*, Vol. 41, pp. 1021-1030.

Xiao, Y., Tutumluer, E., and Mishra, D. (2015). “Performance Evaluations of Unbound Aggregate Permanent Deformation Models for Different Aggregate Physical Properties.” *Transportation Research Record: Journal of the Transportation Research Board,* in press.

Yang, X., and Han, J. (2013). “Analytical Model for Resilient Modulus and Permanent Deformation of Geosynthetic-Reinforced Unbound Granular Material.” *Journal of Geotechnical and Geoenvironmental Engineering,* Vol. 139, No. 9, pp. 1443-1453.

Zhang, Y., Bernhardt, M., Biscontin, G., Luo, R., and Lytton, R. L. (2014). "A Generalized Drucker-Prager Viscoplastic Yield Surface Model for Asphalt Concrete." *Materials and Structures,* in press.

Zornberg, J. G., Prozzi, J. A., Gupta, R., Luo, R., McCartney, J. S., Ferreira, J. Z., and Nogueira, C. (2008). "Validating Mechanisms in Geosynthetic Reinforced Pavements." *Research Report FHWA/TX-08/0-4829-1,* Center for Transportation Research, The University of Texas at Austin, Austin, Texas.